Title

Functional Connectivity Analysis in Magnetic Resonance Imaging of Chronic Pain

Author

Cummings, Jennifer Anne

Publication Date

2025

Peer reviewed|Thesis/dissertation

Functional Connectivity Analysis in Magnetic Resonance Imaging of Chronic Pain

by

Jennifer Anne Cummings

DISSERTATION

Submitted in partial satisfaction of the requirements for degree of

DOCTOR OF PHILOSOPHY

in

Bioengineering

in the

GRADUATE DIVISION

of the

UNIVERSITY OF CALIFORNIA, SAN FRANCISCO
AND
UNIVERSITY OF CALIFORNIA, BERKELEY

Approved:

DocuSigned by:
Sharmila Majumdar
ED3F278527E84B0...

Sharmila Majumdar

Chair

DocuSigned by:
Jeffrey Lotz
DocuSigned by:4DC...

Jeffrey Lotz

DocuSigned by:
Ashish Raj
DocuSigned by:4E0...

Ashish Raj

DocuSigned by:
Grace O'Connell
9F3C0FF166E14FF...

Grace O'Connell

Committee Members

Acknowledgments

I've been uniquely fortunate to have my academic career shaped by so many mentors. First and foremost, to Sharmila: Thank you for giving me the trust and freedom to develop confidence as a researcher. I am continually inspired by your honesty, drive, and passion.

To Valentina: Thank you for picking me up out of a slump and getting me back on track. Your enthusiasm and hands-on guidance reinvigorated my love of science, and I couldn't be more grateful.

To Ashish: Thank you for teaching me a new way of thinking and for your continued encouragement and support. I've learned so much from our conversations, and I am a better person for it.

To my committee members, past and present - Jeff Lotz, Grace O'Connell, Janine Lupo, Pratik Mukherjee, Reza Abbasi Asl, and Oskar Hallatschek - thank you for helping me through these important milestones. Your feedback has been invaluable.

To all of my current and former lab mates: I have enjoyed learning from you as much as I've enjoyed our happy hours and vent sessions. I can't wait to see where you all take your careers.

To my professors, advisors, cohort, and everyone else who I've met along this journey: thank you for making me proud to be a part of this community. I have encountered so many kind, smart, driven people in the Bay, and I'm grateful to have had the opportunity to absorb some of that energy.

To my friends: I hope you all know how much you mean to me. To Dana, Nikki, Briggers: it's been a privilege to grow up with you, and I'm so glad we've maintained the connection all these years. Alessandra, Khalilah, Marina: there is no one I would have rather been stuck in a dungeon with. Thanks for being a continued source of support, humor, and inspiration. Shelby, Katya, Victoria Fong: you each have been instrumental in pushing me over the finishing line, and I'm grateful beyond measure for your tough love and endless pep talks. Kate: You were the first glimmer of hope that I could feel at home here. I'm eternally

grateful that you approached me on orientation day and I couldn't have made it all these years without you. Victoria Alderman: Thank you for being my cheerleader, confidante, and creative partner. I look forward to many more perfect days. Ayah, Alejandro, Jack: The community we've formed over the past year has been a boundless gift. And Lizzie: You made this possible. I'm grateful for your wit, your savvy, your unique perspective, and a million other things.

To my family: I'm lucky to have such a big family, and each of you has helped me get here. I especially must thank my Uncle Ray and Aunt Janet for the immeasurable support, generosity, jokes, and wisdom. To Aunt Janet: I wish you were here, but I know you're proud of me. Thank you for being a role model. To Chris, Michelle, and Fia: Thank you for always being there. I am beyond excited to watch Fia grow up.

To Frenchy: Thank you for expanding my world and showing me how to embrace all it has to offer.

And finally, to my parents: Thank you for always pushing me to be the best version of myself while reminding me that I'm loved just as I am. You created a home in which I felt grounded, safe, and free to cultivate my curiosity, and that is the reason I'm here today. Thank you for teaching me to approach life with a balance of strength and lightness. I love you.

Contributions

A portion of the text in this dissertation has been reprinted from published works, and I would like to thank the co-authors who contributed to those manuscripts. Chapter 5 is adapted from the manuscript titled "Predicting Functional Connectivity from Observed and Latent Structural Connectivity via Eigenvalue Mapping" that was published in Frontiers in Neuroscience and features contributions from Benjamin Sipes, Daniel Mathalon, and Ashish Raj. This work was supported by research grants from the National Institute of Neurological Disorders and Stroke, Grant/Award Number: R01 NS092802/183412; National Institute on Aging, Grant/Award Numbers: RF1 AG062196, R56 AG064873, and R56 AG064873. Chapter 7 is a reprint of "The Knee Connectome: A Novel Tool for Studying Spatiotemporal Change in Cartilage Thickness" as it appears in the Journal of Orthopedic Research and includes work by Kenneth Gao, Vincent Chen, Alejandro Morales Martinez, Claudia Iriondo, Francesco Caliva, Sharmila Majumdar, and Valentina Pedoia. This work was supported by research grants from the National Institute of Health (NIH), Grant/Award numbers: NIH/NIAMS R33AR073552, NIH/NIAMS R00AR070902.

Table of Contents

List of Figures

List of Tables

Chapter 1

Pain

1.1 Introduction

Pain is a complex cognitive process. Although pain is unpleasant, it is also useful; it alerts us to potential tissue damage, encourages us to rest and heal, and teaches us what to avoid in the future.

However, the same processes that serve such adaptive functions can become pathological in excess. This is the prevailing view of chronic pain conditions, which afflict millions of people in the US and abroad. In fact, the great strides we have made in biomedical progress have done little to quell rising rates of chronic pain; to date, chronic pain conditions are among the top causes of global disability, and these numbers are only expected to rise with increasing life expectancy [1].

Treating pain presents a unique challenge due to its subjective nature. In absence of a biomarker or objective measurement tool, we are pushed to view tissue damage as a proxy, but this is flawed in many ways. Primarily, it is a mistake to conflate pain and nociception:

nociception refers to the transduction of electrical signals in cells that react to harmful stimuli (a.k.a nociceptors), while pain is a conscious experience that may arise as a result.

However, pain is much more than a simple mapping of sensory input. We know that someone's emotional state has great influence on his or her perception of a painful stimulus. Extreme examples of this include phenomena such as stress-induced analgesia, in which a person experiencing extreme physical trauma may see a delayed pain onset long enough to flee the situation. A less extreme but more common example is the low coherence between clinical findings and patient-reported pain. Both the high prevalence of incidental findings in pain-free individuals and the extreme pain reported by patients in the absence of any discernible cause support the case for a more nuanced understanding of pain.

Clearly, there is great need for innovation in the study of chronic pain disorders. This thesis will present several novel research studies undertaken in pursuit of that goal. This chapter provides an overview of the current state of pain research, introducing key terms and concepts that will be revisited in later chapters.

1.2 Chronic Pain

The International Association for the Study of Pain (IASP) defines pain as "An unpleasant sensory and emotional experience associated with, or resembling that associated with, actual or potential tissue damage" [2]. Recurrent or persistent pain lasting at least three months is considered chronic [3]. The temporal cutoff of three months was originally believed to mark the normal time frame for healing. While this is no longer considered relevant to all pain conditions, the time frame remains in use due to its consistency with other chronic disorder

definitions [3].

The most recent version of the International Classification of Diseases (ICD-11) recognizes seven major categories of chronic pain: primary, cancer-related, postsurgical or posttraumatic, neuropathic, secondary headache or orofacial, secondary visceral, and secondary musculoskeletal [3]. Chronic primary pain includes conditions in which pain is the leading or only complaint, such as fibromyalgia or nonspecific low back pain, while the other 6 subgroups comprise conditions in which pain results from another identifiable disease, referred to as "chronic secondary pain" [3].

1.2.1 Mechanistic Pain Categories

Since 2017, IASP has recognized three main mechanistic categories for pain persistence, defined as:

1. Nociceptive: Arising from actual or potential tissue damage
2. Neuropathic: Arising from lesion or disease of the nervous system
3. Nociplastic: Arising from altered sensory processing that causes perceived pain despite no evidence of peripheral tissue or neural damage [4]

Although there is general consensus in the field regarding the utility of these categories, their defining characteristics are disputed, and discrete categorization is challenging in practice. Some researchers and clinicians will introduce a fourth "mixed" category to define subjects with overlapping features, while others discourage this term in favor of identifying the primary mechanism [4].

The methods commonly used to discriminate between mechanistic categories can be binned under three broad themes: underlying neurobiology/pathology, exacerbating/alleviating factors, and pain characteristics [4]. Pain categorized as nociceptive is often localized and provoked by certain movements or postures, while neuropathic pain may follow a neuronatomical distribution and accompany sensory deficits or abnormalities such as tingling or burning. Nociplastic pain, the newest and most debated category, is associated with widespread hypersensitivity and pain disproportionate to any pathologic changes and unremitting to rest. Nociplastic pain is most often diagnosed in the absence of discernible features, such as imaging findings, that confirm one of the other two categories [4, 5].

1.2.2 Central Sensitization

Central sensitization is the central nervous system's amplification of pain signals. Hyperalgesia (increased sensitivity to noxious stimuli), allodynia (pain due to a stimulus that does not normally provoke pain), and the widening of nociceptive fields are often considered hallmarks of this process [6]. Once believed to arise as a result of persistent nociceptive input, it is now recognized that central sensitization can occur in the absence of demonstrable injury or inflammation [6].

A growing body of literature suggests central sensitization as the core mechanism underlying many conditions, including fibromyalgia, irritable bowel syndrome, and chronic fatigue syndrome. The frequent comorbidity of such disorders has led the National Institutes of Health (NIH) to coin the term Chronic Overlapping Pain Conditions (COPCs) [6].

Although the concept of central sensitization is commonly used to denote nociplastic pain,

signs of pain hypersensitivity are often also present in neuropathic or nociceptive pain [4, 5]. The boundary between neuropathic and nociplastic pain is itself contested, with some arguing that any altered nociceptive processing is inherently indicative of central nervous system disorder [4]. These disputes have led some experts to suggest that the term "nociplastic pain syndrome" may be more fitting, acknowledging nociplastic pain as part of a chronic pain continuum [7]. However, a key defining feature of central sensitization may be its overlapping presentation with cognitive symptoms such as memory problems, fatigue, and mood disorders, highlighting the neurobiological underpinnings of the condition [7, 8].

Despite a lack of formal definition, the recognition of central sensitization and/or nociplastic pain has proven useful in guiding treatment. Evidence suggests that patients with these phenotypic features may respond better to centrally acting therapies, such as analgesics, while those with more localized pain are likely to have better outcomes from surgery [8].

1.2.2.1 Body Maps as an Assessment Tool

The presence of widespread pain has become a primary indicator for central sensitization/ nociplastic syndromes, spurring a renewed interest in body maps as a measurement tool [7]. Body maps have long been used for communication, but recent methodological advancements have refined body map collection and quantification, allowing for broader use in research and clinical practice. In 2011, the diagnostic criteria for fibromyalgia were updated to include the concept of widespread pain, listing 19 distinct body areas that should be assessed using the Widespread Pain Index [9]. In response, the Michigan Body Map was developed, which overlaid these areas on a graphic representation of a human body, providing a more intuitive experience for patients [10].

1.2.3 Transition from Acute to Chronic Pain

By definition, all pain will first appear as acute before it becomes chronic. As a consequence, chronic pain has been framed as an abnormally prolonged response to acute injury, suggesting that there is a transition point at which a healthy physiological process becomes pathological. However, some recent perspectives have argued that persistent pain is not simply an extension of acute pain but the product of a distinct disease process (or processes) that may occur in parallel to acute pain resolution [11].

This is not to say that tissue damage plays no role in the development of chronic pain. Persistent nociceptor activity has been shown to induce neuroplastic changes in the peripheral and central nervous system, in keeping with the concept of central sensitization described above. However, different types of noxious stimuli engage different neural pathways, reinforcing the understanding that there is no single mechanism underlying all chronic pain development [12].

Additionally, a growing body of evidence suggests that demographic and experiential factors may predispose someone to developing chronic pain. This underscores the importance of framing pain within the "biopsychosocial" model, which understands health as the result of the complex interplay of biological, psychological, and social factors [13]. Certain population groups are significantly more likely to report chronic pain, including women, veterans, older adults, and those with lower educational attainment and socioeconomic status [14]. Biopsychosocial factors can accurately predict one's risk of developing widespread chronic pain, with the most important factors including sleep difficulty, adverse life events, high body mass index (BMI), alcohol use, and employment status [15]. Mental health-related factors

were the strongest overall category of predictors, underscoring the relationship between pain and brain functioning.

1.2.4 Psychological Aspects of Pain

It has long been recognized that emotions play a large role in determining one's pain experience. Positive emotions tend to reduce pain perception and negative emotions heighten it; numerous studies have demonstrated this, most often by inducing emotions in participants through stimuli such as pictures, odors, tastes, or music, and measuring the impact on pain ratings and thresholds [16].

It follows, then, that an individual's thoughts and beliefs around pain can greatly influence their pain trajectory. The fear-avoidance model posits that enhanced fear and anxiety around pain leads to reduced physical activity, which in turn contributes to increasing disability over time through a destructive feedback cycle [17, 18]. Fear avoidance is highly correlated with pain catastrophizing, a cognitive response characterized by magnification, rumination, and feelings of helplessness [19]. Studies have shown that catastrophizing may be the single most important predictor of pain-related outcomes, including treatment response and long-term disability [19]. Catastrophizing is also linked to lower positive affective traits, such as optimism and self-efficacy, and higher negative psychosocial processes such as depression and anxiety [19].

Anxiety and depression (A/D) are the two most common mental health disorders worldwide and often co-occur with chronic pain conditions [20]. Roughly 1 in 20 US adults who participated in the 2019 National Health Interview Survey reported living with comorbid

chronic pain and A/D [21]. This study also showed that people with co-occurring mood and chronic pain disorders were most likely to experience functional limitations [21].

A natural question is one of cause and effect, i.e., whether chronic pain leads to the development of mood disorders or vice versa. One study of US adolescents conducted between 2001 and 2004 indicated that the onset of mental disorders largely preceded that of chronic pain, highlighting specific types of mental disorders (anxiety, affective, and behaviorial disorders) as potential risk factors [22]. While successful treatment of mental health disorders coincides with improved physical function in pain, the reverse correlation is weaker; improvement in physical function following treatment of musculoskeletal pain has not been shown to correspond with improvement of depression, and a very large functional improvement is needed to show any decrease in anxiety symptoms [23].

In light of these findings, there has been growing interest in brain-based treatment strategies for pain. Cognitive behavioral therapy (CBT), a family of psychological treatments aimed at helping patients change destructive thought patterns, has proven useful in treating chronic pain, although success is highly dependent on the individual's attitude [24]. Neuromodulation techniques, which directly modulate neural activity through electrical or chemical stimulation, have also been used to alleviate pain [24, 25]. The continued development and refinement of these strategies will require a clearer understanding of the shared neural mechanisms underlying pain and other affective and cognitive functions, which will be discussed more in following chapters.

Chapter 2

Chronic Musculoskeletal Pain

2.1 Introduction

Chronic low back pain (LBP) and knee osteoarthritis (OA) are two of the most common musculoskeletal disorders and are among the leading drivers of increased opioid prescription in the US [26]. Both disorders are marked by a low correlation between severity of imaging findings and pain reports, leading practitioners to focus on pain management in lieu of targeting the underlying cause [27]. This motivates the need to better understand the relationship between pain perception and peripheral pain drivers in order to develop more targeted treatments. The following sections will provide an overview of key anatomy and potential pain-generating mechanisms associated with these two disorders.

2.2 Low Back Pain

LBP is the leading cause of disability worldwide [28]. LBP can be a symptom of many different disorders, and a large majority (approximately 90%) of LBP cases are classified as non-specific, meaning that the etiology of the pain is unknown [29].

One cause of low back pain is nociceptive signaling from spinal tissues following injury or infection. However, spine abnormalities are often seen in pain-free individuals, highlighting the need to distinguish between pathological spine changes and those associated with normal aging [30, 31]. The spine is a site of much strenuous motion and weight-bearing, making it prone to degenerative changes [32]. Its tissues also receive a complex array of nerve connections, making it difficult to locate the origin of pain [33].

2.2.1 Spine Anatomy

The human spine, or vertebral column, is the long bony structure connecting the head to the pelvis. It serves to protect the spinal cord, bear the weight of the body, and enable motion.

The spine consists of many independent bones, called vertebrae, divided into five distinct sections moving inferiorly from the head: the cervical spine, thoracic spine, lumbar spine, sacrum, and coccyx. The vertebrae in the cervical, thoracic, and lumbar spines (aside from the first and second cervical vertebrae) are separated by intervertebral discs that provide cushioning and enable passage of nutrients and fluids to the spine and spinal cord. Vertebrae and discs are named according to their section (e.g. L1 is the first vertebra of the lumbar spine, and the L1-L2 disc resides between L1 and L2) [32]. Along the posterior column of the spine, the bony vertebrae extend into articular processes, called facets, that meet at the

facet joints, the only synovial joints of the spine.

The spinal cord is a bundle of nerves running through the vertebral column from the base of the skull to the first or second lumbar vertebra. It allows for communication between the brain and body; ascending tracts deliver sensory information to the brain, while descending tracts coordinate motor actions. The spinal cord contains 31 pairs of nerves, each of which emerges from a corresponding segment and innervates a specific anatomical region. The fibers that form the spinal nerves are divided into four sections, with the dorsal half comprising interneurons that receive input from either somatic or visceral sensory neurons, and the ventral half divided into visceral (autonomic) or somatic motor neurons [34]. At each level, dorsal (sensory) and ventral (motor) fibers, called roots, fuse laterally to form the nerves, while rami extend out of the cord to the rest of the body. The anterior rami interlace into complex bundles, called nerve plexuses, which mostly service the limbs. The combination of nerve fibers from multiple spinal segments ensures that damage to one nerve does not cause total limb paralysis [34].

2.2.2 Spine Pathophysiology

Causes of spinal pain can be grouped into mechanical (macroscopic) and nonmechanical (microscopic) mechanisms and further classified according to the anatomic sites of origin [33]. Mechanical mechanisms, such as disc herniation and nerve compression, may be seen on imaging. Nonmechanical mechanisms include the release of proinflammatory cytokines, which stimulate the nerves, as well as innervation and neovascularization of degenerating tissues [33].

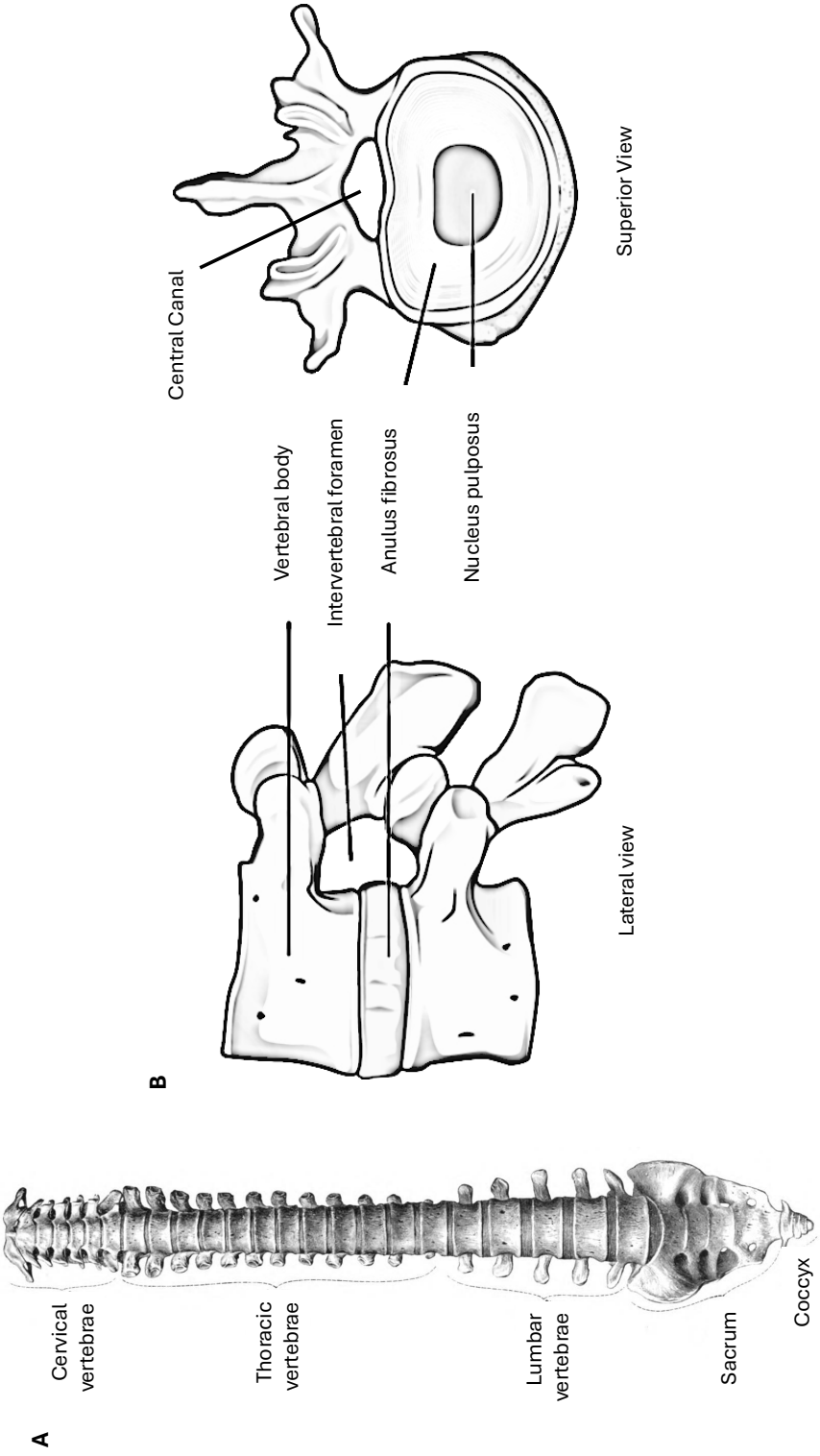

Figure 2.1 A) Frontal view of spine with section labels. B) Lateral and superior views of vertebral body and disc anatomy. Image adapted from Wikimedia Commons

A recent meta-analysis of 29 common spine imaging findings across five categories indicated that eleven were significantly associated with LBP, including discogenic (disc degeneration, disc herniation), osseous (type I Modic changes, endplate defects), neurogenic (spinal canal stenosis, nerve compression), and paraspinal (muscle fat infiltration) features [35]. While these authors did not find an association between any facetogenic features and LBP, this may be due to their search strategy, which did not extend to neuropathic pain specifically [35]. An earlier meta-analysis comparing rates of imaging findings between LBP patients and pain-free individuals reported largely similar results with some key differences, including a positive association with spondylolysis and no association with central canal stenosis [31]. These differences may also be attributed to the more recent study's exclusion of primary neuropathic pain [35]. An overview of relevant findings is provided below.

2.2.2.1 Discogenic

Intervertebral discs comprise a gelatinous inner core, called the nucleus pulposus, and a fibrous outer layer, the anulus fibrosus. The nucleus pulposus mostly contains type II collagen and proteoglycan, while the anulus fibrosus mostly consists of type I collagen. The gelatinous texture of the nucleus pulposus subserves its purpose as a shock absorber, while the fibrous structure of the anulus fibrosus helps it contain the nucleus and balance mechanical loads [33].

The discs are highly innervated by somatic and autonomic nerves from the levels above and below the point of entry as well as from the contralateral side, complicating pain localization [33]. Somatic afferents are associated with localized pain, while autonomic afferents convey diffuse pain. In healthy discs, sensory nerve fibers are limited to the outer third of the anulus

fibrosus, but deeper ingrowth has been observed in diseased discs, which is a likely cause of pain [33].

Disc degeneration is characterized by degradation of the nucleus pulposus, while disc herniation is the displacement of disc tissue outside of the space defined by the edges of the bordering vertebrae. In healthy discs, the nucleus pulposus is isolated from the immune system, but structural changes, such as aging or injury, can expose it to immune cells such as macrophages. This can initiate a cycle through which the nucleus pulposus cells generate inflammatory cytokines that activate nociceptors directly while also promoting the expression of nerve growth factor (NGF), causing deeper innervation of the disc [33].

Disc degeneration is often classified using the Pfirrmann grading system, which details grades of one through five with increasing severity based on features derived from MRI, including structure, signal intensity, disc height, and distinction between the nucleus and anulus [36]. Pfirrmann grade has a positive association with LBP, though this relationship may be mediated by confounding factors such as Modic changes and disc herniation [35].

2.2.2.2 Osseous

Osseous features can include pathological changes to the vertebral bone and endplate as well as structural abnormalities [35]. Endplate changes are strongly linked with LBP, while the relationship between pain and structural abnormalities is more tenuous.

The vertebral endplate consists of both an osseous component, which is part of the cortex of the vertebral body, and a cartilaginous component, which lies between the osseous endplate and the adjacent disc. A network of arteries in the osseous endplate allows nutrients to flow between the vertebral marrow and disc cells [33]. However, this porosity makes the endplate

especially susceptible to damage, which can enable contact between disc nuclei and vertebral marrow. This can provoke an inflammatory response in disc cells that may promote pain through multiple routes, including nerve sensitization, disc degeneration, and bone marrow changes [37].

Clinically significant endplate defects include Schmorl nodes, fractures, erosion and sclerosis. These can result from acute traumatic injury or from accumulated stress. Schmorl nodes are large focal endplate indentations representing contact between the disc and vertebra. These are common in asymptomatic individuals, but painful nodes are associated with concurrent bone marrow lesions and fibrovascular changes [37].

Modic endplate changes are identified by signal intensity changes on MRI and are classified into three types [38]. Modic type 1 findings indicate bone marrow edema and proliferation of blood vessels resulting from inflammation. The endplates adjacent to the fibrous bone marrow show increased presence of sensory nerve fibers, which is a likely root of chronic pain. In contrast, Modic types 2 and 3 are not associated with angiogenesis or neurogenesis and are not commonly associated with LBP, although types 1 and 2 have been shown to convert between each other and may represent different stages of a common pathologic process [33]. There are several theories regarding the biochemical origin of inflammation causing type 1 Modic changes. One posits that an initial injury to the osseous vertebral endplate causes microtrauma and fracturing to propagate, while a second theory suggests that disc disruption is the primary injury. Bacterial infection at the disc or vertebral endplate is another potential cause [33].

Commonly identified structural abnormalities include spondylolysis and spondylolisthesis. Spondylolysis is an anatomical defect or fracture of the vertebral arch, most often at the L5

vertebrae. It is commonly found in children and adolescents with LBP and is associated with sport-related stress [39]. In contrast to all other imaging findings discussed here, spondylolysis is rarely diagnosed with MRI but is mentioned for completeness. Spondylolysis can progress to spondylolisthesis, the anterior displacement of vertebral bodies [39]. Spondylolisthesis can cause compression of nerve roots resulting in radiculopathy in the lower extremities.

2.2.2.3 Neurogenic

Neurogenic features are mostly associated with neuropathic pain, which may be caused by mechanical nerve compression and/or nerve stimulation by cytokines and neurotransmitters. LBP is often accompanied by radiculopathy, a neuropathic abnormality involving the loss of sensory and/or motor function caused by nerve damage which may or may not be painful [33].

Mechanical nerve compression is often the result of stenosis, the narrowing of nerve canals. Central canal stenosis refers to compression of the dural sac and spinal cord, while foraminal stenosis involves narrowing of the subarticular zone through which nerve roots exit. Disc herniation is a common cause of stenosis. Severe types of herniation, called disc extrusions, are characterized by annulus damage that allows the nucleus to leak into the spinal canal, putting additional pressure on the spinal cord and triggering a larger immune response [32]. Herniation is most common in the lower lumbar spine, especially at the L4-L5 and L5-S1 discs, which can impinge the sciatic nerve that runs down the back of the legs and cause severe discomfort and functional limitations [32].

2.2.2.4 Facetogenic

The facet joints are highly innervated with proprioceptive and nociceptive nerves from two different spinal levels. They are also mobile and thus especially prone to mechanical stress. Degenerative changes can cause arthropathy, marked by cartilage loss, hypertrophy, and swelling, which can directly cause pain as well as inducing neuropathic symptoms by narrowing the subarticular zone and neural foramen [33]. In contrast to central canal stenosis, foraminal stenosis compresses specific nerves and is likely to cause more localized radiculopathy.

2.2.2.5 Paraspinal

The paraspinal muscles play an important role in stabilizing the spine and protecting it from damage. Key muscles include the Multifidii, Erector spinae, psoas, and Quadratus lumborum [35]. Types of muscle-related pain include myofascial pain, involving the interaction between muscles and their membranous surrounding tissue (fascia), and tendinopathy, regarding the tendons that connect muscle to bone [33]. Both are associated with and exacerbated by a release of proinflammatory cytokines and neurotransmitters resulting from muscle overuse, injury, or psychologic stress [33].

Common metrics used to assess the muscles on imaging include fat infiltration (FI) and cross-sectional area (CSA). Studies investigating a link between these measures and LBP have shown mixed results, but some have indicated an association with multifidus FI and CSA as well as erector spinae FI [35]. However, it is difficult to establish a chronological link between muscle morphology and pain, as nerve damage and/or inactivity is likely to induce muscle changes.

2.3 Knee Osteoarthritis

OA is the most prevalent chronic joint disease and a leading cause of disability in older adults [27]. Pain is the primary symptom of OA. This pain is usually localized to the affected joint, aggravated by use, and relieved by rest, though pain frequency increases with disease severity and will sometimes radiate to connected body parts.

While OA can affect many joints, the knee is most afflicted, with knee OA accounting for about 85% of global OA burden [40]. Articular cartilage thinning is a signature of OA and is most often recognized as joint space narrowing in radiographs. However, there is low concordance between radiographic OA and subjective pain. Among those with radiographic knee OA, reported rates of concurrent pain have ranged from 15 to 81% [41]. A better understanding of the pain generating factors in OA is necessary to develop more sensitive biomarkers and targeted treatments.

2.3.1 Knee Anatomy

The knee is a complex joint that bears a great deal of body weight and enables motion in three different planes (sagittal, transverse, and frontal) [42]. The knee joint consists of four bones: the femur, tibia, fibula, and patella. The femur sits atop the tibia, forming the femorotibial joint, which bears most of the weight. The patella, or kneecap, is a sesamoid bone sitting anteriorly to the femur that enables frictionless transfer of muscle forces during flexion and extension [42].

Two types of cartilage support the knee joint. Fibrocartilaginous menisci sit atop the tibia, forming a cushion for the femur. Articular cartilage covers the femoral and tibial

condyles, serving to reduce friction and absorb shock during movement [42]. Both menisci and articular cartilage are composed largely of collagen; menisci contain mainly type I collagen, and cartilage type II [43]. The knee joint also has four bursae, cavities filled with synovial fluid, which further reduce friction [42].

The knee is primarily stabilized by ligaments and secondarily by muscles. The anterior cruciate ligament (ACL) is thought to contribute a large majority (approximately 85%) of knee stabilization and is the most frequently injured [42]. The ACL works with the posterior cruciate ligament to prevent anterior movement of the tibia. The joint is also supported by two cruciate ligaments on the lateral and medial sides, preventing excessive vagus and valgus motion [42].

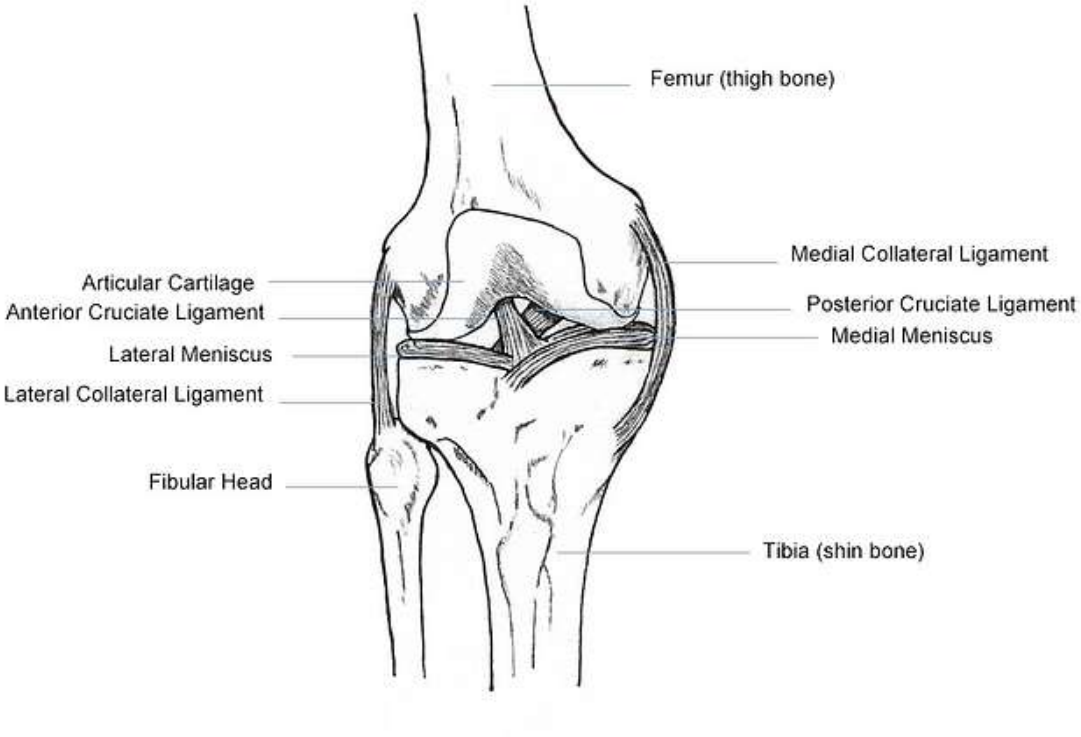

Figure 2.2 Knee anatomy. Image Source: Wikimedia Commons

2.3.2 Knee Pathophysiology

As in low back pain, nociception in OA is likely driven by both mechanical and chemical stimuli. Although cartilage loss is the most studied biomarker of OA, cartilage is not normally innervated and thus cannot directly generate pain, although neurovascular invasion has been shown in severe disease [27]. In mild and moderate disease, pain sensation is likely driven by innervated tissues such as the bone, ligaments, menisci, and synovium [27].

The most common structural abnormalities seen in patients with symptomatic OA include bone marrow lesions (BMLs) and synovitis. BMLs are lesions beneath the subchondral bone characterized by fat necrosis, marrow fibrosis, and microfractures [27]. Although the exact mechanism by which BMLs generate pain is unknown, bone marrow is highly innervated with nociceptors that are likely to become increasingly sensitized by mechanical and inflammatory mediators generated over the course of disease [44]. Additionally, pain is more prevalent in patients whose cartilage is denuded to the bone, suggesting a link between subchondral injury and pain generation. Synovitis, swelling of the synovial membrane, is similarly thought to drive pain through the production of inflammatory mediators and/or mechanical pressure [27].

The role of cartilage thickness in OA pathogenesis is complicated. In contrast to earlier belief that OA is a disease of cartilage "wear and tear", advancements in imaging have provided a more nuanced view. Studies have shown both cartilage thickening and thinning at different rates and locations of the knee over the course of the disease [45, 46, 47, 48]. Early stages of OA are characterized by cartilage changes including increased hydration, proteoglycan loss, and disruption of collagen fibers, which may appear as thickening as a

result of hypertrophy or swelling [45, 49, 50, 51]. Cartilage thinning over time has shown very minor correlation with worsening pain, a relationship that may be mediated by worsening synovitis [52]. However, this relationship may not be linear but instead escalate at later stages of disease, especially when cartilage is denuded to the point of bone exposure [53]. The knee connectome project described in a later chapter represents an attempt to better understand these complicated dynamics as they relate to OA development.

Chapter 3

Neuroscience of Pain

3.1 Introduction

The nervous system is the biological basis of both nociception and pain. Nociception begins in the peripheral nervous system, where specialized somatosensory neurons, called nociceptors, initiate a cascade of electrical activity in response to harmful or potentially harmful stimuli. This signal is transmitted to the central nervous system (i.e. the brain and spinal cord) so that an appropriate response may be enacted. Pain perception is thought to arise through the coordinated activity of a network of higher-order brain regions, most often as the result of suprathreshold nociceptor activation. This network involves brain regions associated not just with sensory processing but also with emotion, attention, and memory, all of which contribute to short and long term behavioral adaptation.

Scientists have long sought to identify a single structure or set of structures that encodes pain, sometimes referred to as the "pain matrix" or "neuromatrix". However, growing evidence suggests that there is no specific pattern of brain activity associated with all pain

but rather a set of networks that are engaged to varying degrees depending on context. These are often classified by their primary cognitive function, resulting in sensory-discriminative, affective-motivational, and cognitive-evaluative components.

Chronic pain is increasingly believed to arise as the result of reorganization within both the peripheral and nervous system. Numerous studies have shown structural and functional differences between chronic pain patients and pain-free individuals, some of which may be reversed after successful pain treatment. Longitudinal studies have even suggested a shift in the very representation of pain, with LBP subjects showing increasing activation of emotion and reward circuits during pain fluctuations as pain transitions from acute to chronic [54]. This supports the notion of chronic pain as a distinct disease process rather than an extension of the same neural processes underlying acute pain.

This chapter will discuss the neurobiology of pain perception and chronification. It begins with a review of basic anatomy and physiology of pain-related neural circuits. Then it will present key findings regarding neural abnormalities in chronic pain, with an emphasis on chronic LBP. Finally, it will outline potential mechanisms underlying central and peripheral sensitization.

3.2 Peripheral Nervous System

The cell bodies of sensory neurons form the peripheral ganglia. The ones innervating most of the body reside in the dorsal root ganglia alongside the spinal column, while those innervating the head and parts of the neck originate from the trigeminal ganglion, located near the temporal bone of the skull [55, 56]. Most primary somatosensory neurons are pseudounipolar,

meaning that they have one axon that emerges from the cell body and then bifurcates, with one end extending to peripheral tissue and the other extending centrally toward the spinal cord [56]. Within the spinal cord, these axons may enter the white matter and directly connect to higher spinal cord or brain levels, or they may synapse onto second-order interneurons in the dorsal horn of the spinal cord [34].

Peripheral nerve fibers are classified by their myelination, which constitutes their diameter and conducting velocity, and by their function relative to the central nervous system. Afferent nerves bring signals from the periphery to the central nervous system, while efferent nerves send signals outward [57]. Most afferent nerve fibers involved in nociception are C-fibers: thin, unmyelinated axons with conducting speeds of 0.4 to 1.4 m/s. A smaller portion are A-fiber nociceptors, most in the Aδ range, which have thinly myelinated axons and faster conducting speeds of 5 to 30 m/s [56]. Aδ fibers are associated with fast-onset acute pain, while C fibers mediate the slower, more diffuse pain that follows.

Nociceptors are also categorized by the type of stimulus they respond to (mechanical, thermal, or chemical). Most cutaneous C-fiber nociceptors are polymodal, meaning that they respond to all three stimuli, while A-fiber nociceptors are often sensitive to mechanical and/or noxious heat stimuli, with some also responding to extreme cold [56]. The visceral nociceptors innervating the internal organs are also predominantly C-fiber types responding to mechanical and/or chemical stimuli [58].

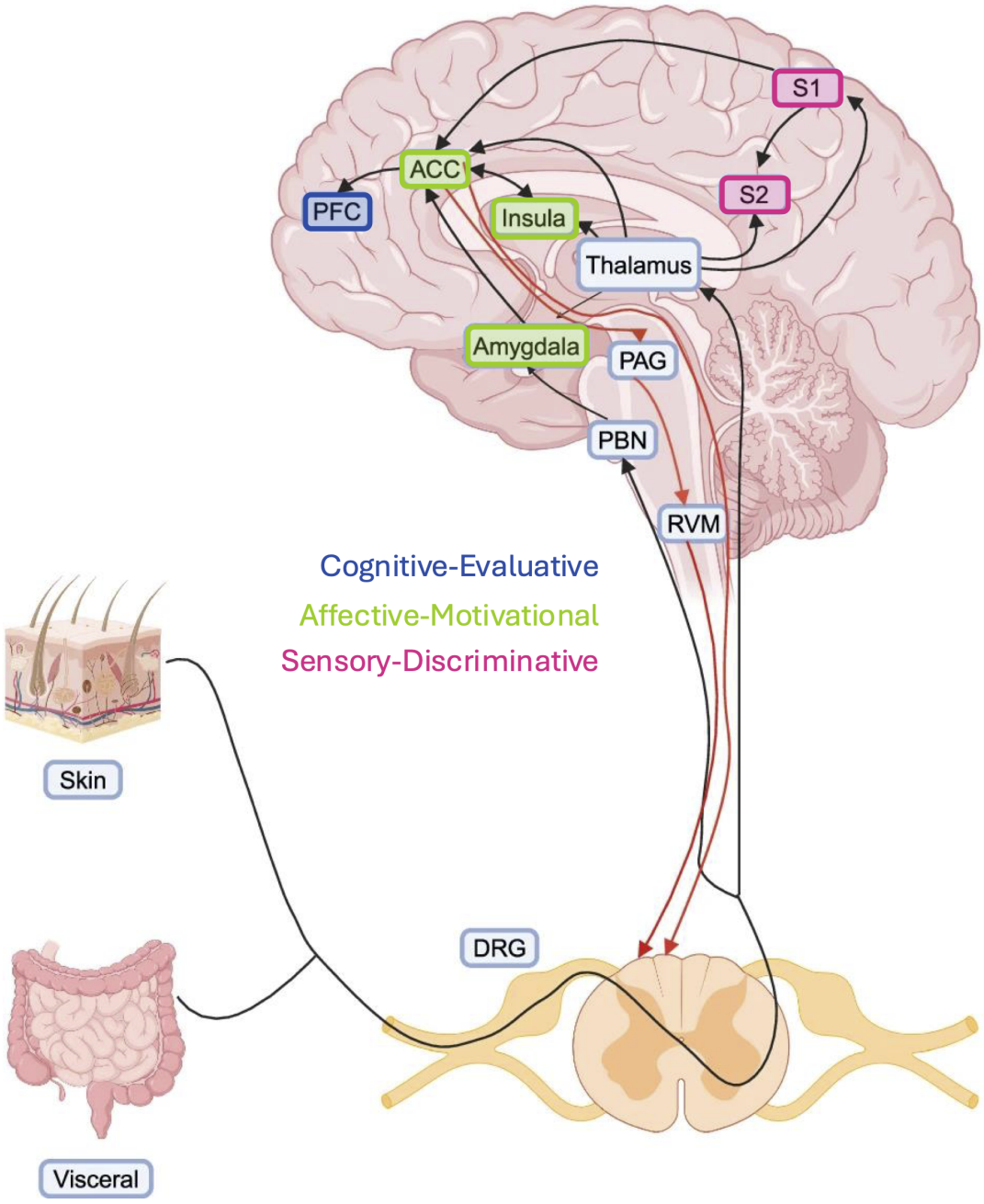

Figure 3.1 Neural circuits of nociception. The ascending pathway (black) sends nociceptive signals from the peripheral to central nervous system. Specialized primary somatosensory cells called nociceptors have cell bodies in the dorsal root ganglia and axons extending to the skin and viscera. These neurons project to the thalamus, brain stem, and cerebellum. The thalamus projects to higher order cortical regions coordinating the multidimensional pain experience, while the PBN projects to the amygdala, primarily involved in emotional regulation.The descending pathway (red) exerts top-down influence on neurons in the dorsal horn. Figure adapted from Chang et al., 2024[59].

3.3 Central Nervous System

3.3.1 Ascending Pathways

Nociceptive signals are transmitted to the brain through a series of parallel ascending pathways that synapse mainly in the diencephalon, cerebellum, and brain stem. The major ascending sensory pathways include the spinocerebellar, spinothalamic, and spinoreticulothalamic tracts [34]. The spinocerebellar tract mainly coordinates unconscious motor movements. Brain stem-directed tracts, such as the spinoreticular and spinomesencephalic axons, control affective and autonomic nervous system responses, such as increased heart rate and blood pressure, while also routing signal to higher order brain regions [34]. Spinoparabrachial axons relay nociceptive information to the amygdala, mediating emotional responses [60]. Direct connections between the spinal cord and limbic regions have also been described [61].

The thalamus is the main relay station between the spinal cord and the cortex. Though most spinothalamic tract fibers project to the thalamus, some also synapse on brain stem areas such as the periacqueductal grey (PAG) and the reticular formation [60]. Axons reaching the thalamus terminate in the lateral, posterior, or medial sections, with each section mediating a different dimension in the pain experience. Relay neurons in the lateral thalamus project to the primary (S1) and secondary (S2) sensory cortices; this is sometimes referred to as the sensory-discriminative or lateral system. The largest proportion of spinothalamic tract fibers synapse in the posterior thalamus, which contains relay neurons projecting to the posterior insula. Spinothalamic tracts synapsing in the medial thalamus project to the prefrontal cortex and parts of the cingulate, mostly those involved in motor processes. The medial thalamus also receives nociceptive signals indirectly from the reticular formation via

the spinoreticulothalamic tract. Together, the posterior and medial thalamus networks are believed to encode higher cognitive functions related to pain processing, such as affective and attentional modulation and the coordination of motor responses [60].

3.3.1.1 Sensory-Discriminative

The sensory-discriminative system primarily serves to determine the location, intensity, and type of pain, although affective states have been shown to influence pain processing in the somatosensory cortices [62]. S1 is located in the postcentral gyrus and is known for its somatotopic organization, in which specific cortical subregions receive input from specific body parts [63]. In addition to location, S1 neurons also encode tactile features like texture and intensity [62]. S2 is also located in the parietal cortex and is thought to mediate processing of sensory inputs to S1, such as memory formation, through connections to the amygdala and hippocampus [63]. Compared to S1, much less is known about the role of S2 in pain processing, although responses in S2 have been shown to correlate with pain intensity [62].

3.3.1.2 Affective-Motivational

The insula is the only cortical region that has been shown to induce pain from stimulation [24]. It is believed to act as a bridge between the sensory-discriminative and affective dimensions of pain; after receiving nociceptive input through reciprocal connections with the brain stem and thalamus, information within the insula appears to flow in a posterior-to-anterior gradient, with the posterior insula connecting to somatic regions such as S1, S2, and lateral thalamus, and the anterior insula connecting to cognitive regions such as orbitofrontal cortex, nucleus

accumbens, and medial thalamus [24, 64].

The ACC is involved in many functions, including socio-emotional processing, cognition, and sensation [24]. It is implicated in many aspects of pain, such as pain aversiveness and unpleasantness and empathic pain. It also has connections to the spinal cord, enabling top-down control of sensitivity thresholds independent from the main descending pathway originating in the brainstem [62].

Both the insula and ACC share reciprocal connections with the amygdala, a region long recognized as a key driver of emotion. The amygdala also receives direct nociceptive information through a unique pathway from the parabrachial nucleus (PBN) in the pons. This may in part explain its inconsistent activation in pain; unlike the insula and ACC, which are almost always activated by direct painful stimuli, the amygdala is thought to play a more specialized affective role [24].

3.3.1.3 Cognitive-Evaluative

The prefrontal cortex (PFC) is considered the main driver of the high-level cognitive dimensions of pain, like decision making and the formation of complex associations. The medial PFC (mPFC) is highly connected with the striatum, in particular the nucleus accumbens (NAc), subserving its role in reward appraisal, motivation, and behavior planning [60]. Connectivity strength of the cortico-striatal circuit has been proposed as a predisposing factor for developing chronic pain [65]. There are also reciprocal connections between medial PFC and amygdala which have been implicated in the generation of pain-associated cognitive decline [60].

3.3.2 Descending pathway

Transmission of nociceptive signals is modulated in a top-down manner through the descending pathway, mainly through the rostroventral medulla (RVM), which connects directly to neurons in the dorsal horn. The RVM receives input from higher order cortical and limbic structures both directly and indirectly via PAG. RVM's pain-mediating effects are controlled by two distinct neuronal classes, referred to as "on-cells" and "off-cells", which serve to enhance or inhibit nociceptive signaling, respectively. The descending pathway is a major target of analgesic drugs, including nonsteroidal anti-inflammatory drugs (NSAIDs), opioids, and cannabinoids, which all serve to alter the balance of on- and off-cell activity in RVM [66]. Interactions between affective states and pain perception, such as stress-induced analgesia and hyperalgesia, are likely mediated through this pathway. It is also likely to play a role in the development of chronic pain, as deactivation of RVM has been shown to induce hyperalgesia at the site of previous injuries after sensitization appears to resolve, and lesioning descending pain fibers has been shown prevent development of neuropathic pain while leaving acute pain responses intact [67, 12].

3.4 Brain Alterations in Chronic Pain

Chronic pain is associated with structural and functional changes throughout the brain. Morphometric analyses have consistently revealed gray matter differences in chronic pain patients compared to healthy controls, including reductions in gray matter volume and thickness in pain processing regions, including ACC, insula, and PFC. These measures have been shown to correlate with clinical parameters such as pain intensity and duration,

suggesting their potential as biomarkers [68, 69]. A recent analysis comparing over 10,000 participants with and without chronic pain revealed widespread reductions in cortical surface area across conditions and increased cortical thickness in the precuneus and orbitofrontal cortices. Reductions were most strongly correlated with chronic musculoskeletal pain and with pain in multiple sites. This study also suggested a particular role of the precuneus in mediating the comorbidity of pain and depression [70].

Differences in white matter integrity have also been shown, indicating reductions in many tracts connecting regions involved in pain and strengthening of circuits between these regions and the basal ganglia [68, 69]. In keeping with the theory of cortico-striatal connectivity predicting pain chronification, it has been suggested that white matter strength between mPFC-NAc may predispose someone to developing chronic pain [71].

Functional analysis has revealed substantial alterations in chronic pain patients. These include regional activity differences and widespread connectivity differences not just in areas traditionally associated with pain, such as insula and ACC, but also in visual and motor cortices [72]. Graph theoretic measures have further supported the view of chronic pain as a state of widespread brain network reorganization. Global disruption of degree rank order (k_D) has been demonstrated as a hallmark of chronic pain across conditions, suggesting that brain regions that are strongly connected in healthy controls are weakly connected in chronic pain and vice versa. Interestingly, this study also identified specific connectivity differences associated with certain conditions. LBP was correlated with decreased connectivity in ACC, supplementary motor area, and parts of the parietal lobe, and increased connectivity in the thalamus, hippocampus, NAc and mPFC. OA patterns were similar but also showed a specific decrease in S2 connectivity [73].

3.4.1 Peripheral and Central Sensitization

An underlying mechanism of chronic pain development is increased sensitization brought on by neuroplastic changes. Sensitization can occur at multiple levels and often results in a feedback loop of increasing pain signal amplification.

Peripheral sensitization occurs at the terminals or along the axons of nociceptors when mechanical or chemical insults lead to hyperexcitability and faulty signal transmission. At a molecular level, these changes are enacted through modified expression and sensitivity of ion channel receptors [60]. These changes are amplified by alterations in glia and autonomic neurons [74]. In the DRG, nociceptor cell bodies may show changes in membrane composition and synapse properties contributing to inappropriate signaling to the CNS [74]. These effects are propagated within the spinal cord, where changes in neuronal and glial mechanisms can interrupt the balance of excitation and inhibition and lead to overlap between nociceptive and non-nociceptive tactile circuits, which has been associated with mechanical allodynia [60].

Supraspinal changes can impact both the ascending and descending pathways. Central sensitization has been associated with functional connectivity increases within pronociceptive brain areas and decreased connectivity in antinociceptive areas. Insula hyperactivity appears especially critical in central sensitization and has been shown to correlate with self-reported pain, pain reduction, and increased sensitivity to multisensory stimuli. Decreased connectivity and activation of brainstem regions such as PAG is also shown, contributing to a reduction in activity of the descending analgesic pathways. [6].

Chapter 4

MRI

4.1 Introduction

Magnetic Resonance Imaging (MRI) is a medical imaging technique that has grown popular in both clinical care and research. The method exploits the fact that different tissues exhibit different properties when exposed to a strong magnetic field, allowing us to acquire non-invasive cross-sectional images of internal anatomy and physiology with no exposure to radiation. This chapter will explain the basic principles of MRI and specific sequences used in this thesis. It will then introduce the concept of the "connectome", a statistical object used to reveal novel relationships in MRI-derived data throughout the following chapters.

4.2 General physics

MRI is an application of the nuclear magnetic resonance (NMR) phenomenon. NMR describes a property exhibited by atoms with nonzero spin (i.e. those with unpaired nucleons) when

a magnetic field is applied, causing their protons to precess around an axis oriented in the direction of the field. Each element with a magnetic moment has a unique parameter called the gyromagnetic ratio that determines their precession frequency when experiencing a magnetic field, called the Larmor frequency. The net vector sum, or net magnetization vector, of many spins experiencing the same field creates its own small magnetic field, which can produce a detectable signal as it induces an electrical current in a receiving coil [75]. While most atomic elements have an isotope with nonzero nuclear spin, hydrogen protons are most commonly used in MRI due to their high abundance in tissue molecules such as water and fat [76].

Acquiring an MR image requires three main pieces of hardware: a main magnet, radiofrequency (RF) coils, and gradient coils. The magnet creates a strong homogeneous magnetic field (B0) necessary to align the spins into a net vector, usually on the order of 1.5 to 7 Tesla. The RF coils transmit a pulse that causes the spins to realign in the direction of the magnetic component of the pulse (B1) and to lock in phase. When the pulse is turned off, the spins begin to return to B0 and fall out of phase, emitting energy that is recorded as signal in the same RF coils. The gradient coils create slight perturbations in the main magnetic field at different locations throughout the magnet bore, creating variation in the resonance frequency that allows for spatial encoding of the signals [76]. This process is repeated many times to build a complete image. The time period between B1 excitation pulses is called the repetition time (TR), while the time between pulses and the recording the of the echo signal is called the time to echo (TE).

The signal a tissue transmits in an MR image is dependent on inherent properties that are determined by its molecular composition. The magnitude of a tissue's magnetization vector,

and thus its signal strength, depends on the number of mobile protons per unit volume that are available to line up with the magnetic field, called the proton density (N(H)). Tissues also exhibit unique time constants that determine their rate of returning to an equilibrium state following an RF excitation pulse. The time it takes for a tissue's magnetization vector to return to maximum alignment with B0 is called T1 (aka longitudinal or spin-lattice) relaxation time, which depends on qualities such as the material's magnetic susceptibility and the strength of B0. The time it takes for the spins to fully dephase is called T2 (aka transverse or spin-spin) relaxation time, which is caused by the magnetic fields of adjacent protons interfering with each other. In practice, dephasing is also accelerated by magnetic field homogeneities, resulting in a faster rate constant called T2*. By varying scan parameters such as TR and TE, one can emphasize the differences in these properties between tissues to maximize signals of interest. The specific design of parameters used to achieve an image is called a pulse sequence.

4.3 Contrast

In MRI, soft-tissue contrast is achieved by varying acquisition parameters to weight different tissue properties. T1-weighted sequences use short TR and TE to emphasize differences in T1 relaxation times. Because signal intensity is proportional to T1, substances that have a shorter T1 will recover signal faster and appear brighter at a short TE. T1-weighted images are especially useful for defining anatomical structure, as fatty tissues appear bright and water-based tissues are dark. Conversely, T2-weighted images are obtained using a long TR and TE, highlighting differences in signal decay over time. In T2-weighted images, water

appears brightest due to its long T2, while solid tissue appears dark. T2-weighted images are valuable for pathology detection, as most lesions, such as tumors and edema, will appear brighter than surrounding tissue. Proton density-weighted (PD) sequences de-emphasize T1 and T2 by using a long TR and short TE, producing images that highlight the inherent proton density of tissues. Fluid-filled structures tend to have higher mobile proton density than solids, making proton weighting especially useful in differentiating fluid and non-fluid structures [76].

4.4 Musculoskeletal Applications

Standard clinical assessment of the spine or knee will include a combination of T1, T2, and PD-weighted sequences in multiple planes, allowing radiologists to assess signs of damage in different tissues. The work presented in this thesis involves a few select measurements.

The investigations of low back pain focus on two imaging findings commonly associated with pain, type 1 Modic changes and stenosis. Modic type 1 changes are assessed using sagittal MRI, where they appear as hypointensity in T1-weighted images and hyperintensity in T2 [33]. Spinal canal stenosis is typically evaluated using sagittal T2 and axial T1-weighted images, while assessment for foraminal stenosis primarily uses sagittal T1.

The cartilage thickness measurements used to generate knee connectomes are derived from 3D double-echo steady-state (DESS) knee MR images, a complex sequence that involves the application of two echoes and combining the resulting signals to produce a single image per slice with enhanced T2 contrast [77].

4.5 Advanced Techniques

4.5.1 Diffusion MRI (DWI/DTI)

The structure-function modeling chapter of this thesis uses structural connectivity derived from Diffusion Tensor Imaging (DTI). DTI enables the reconstruction of long range fiber tracts in the brain corresponding to axonal connections between brain regions. DTI is an extension of Diffusion-weighted imaging (DWI), an advanced MR technique that leverages the random thermal motion, aka diffusion or Brownian motion, of water molecules in tissues to investigate their microstructural properties. A DWI sequence involves adding two gradients along the same axis, called diffusion-sensitizing or motion-probing gradients, to a T2-weighted spin-echo sequence before and after a 180° refocusing pulse. The motion of water molecules between the two pulses will result in less rephasing of proton spins, and thus a reduced signal, in a voxel compared to signal measured without the pulses. The signal decay is used to estimate the apparent diffusion coefficient (ADC), a metric of displacement over time.

4.5.2 Functional MRI (fMRI)

The brain functional connectivity analyses conducted in this thesis use data derived from Functional MRI (fMRI). fMRI is a technique that captures changes in blood flow associated with metabolic activity. Since its discovery in 1991, fMRI has become a leading modality in the study of whole brain function in humans.

The most common form of fMRI method uses blood oxygen level–dependent (BOLD) contrast, which relies on the fact that deoxygenated hemoglobin is paramagnetic while oxyhemoglobin is diamagnetic, causing magnetic field distortions near the blood cells and

vessels carrying deoxyhemoglobin. Protons near the distorted field will precess at different frequencies than surrounding particles, leading to MR signal attenuation that increases over time. Increases in brain region activity lead to increased blood flow and oxygenation in those areas, causing a local increase in T2 and T2*-weighted signal [78].

In contrast to other MRI methods, fMRI involves acquiring an entire brain volume image many times over the course of a scan using a sequence called echo planar imaging (EPI) [78]. A volume is collected every TR, usually about every two seconds, over a 5-20 minute scan, with some evidence suggesting that optimal test-retest reliability is achieved with a scan length of about 13 minutes [79]. During the scan, subjects are either presented with a task or stimulus or simply asked to lie still at rest, normally while fixating at a point on a screen [78].

4.5.2.1 Task vs. Rest

All of the fMRI studies presented in this thesis involve resting-state data (rsfMRI). There are many benefits to fMRI. Primarily, it is easier to collect, as it does not require additional equipment and avoids contamination of certain noise factors such as motion that may arise from performing a task. It also allows flexibility in analysis methods and is also suitable for many populations, including those who may have trouble performing a task consistently due to fluctuating symptoms, attention deficits, or fatigue [80].

However, there are also many limitations to rsfMRI. A core criticism of rsfMRI is that the brain is never truly at rest and that a lack of insight into a participant's dynamic mental activities clouds the data and inhibits interpretation. Task-based paradigms have generally been shown to provide higher information gain regarding specific neural responses and demonstrate superior predictive accuracy and reliability [81]. They can also lead to

better quality data due to higher participant engagement and less likelihood to fall asleep [82].

rsfMRI is particularly suitable for the applications provided here, in which it is used to investigate the properties of intrinsic connectivity arising as a product of underlying structure or in relation to spontaneous pain. In the study of chronic pain, rs-fMRI has contributed to an understanding of the disorder as a unique disease state by revealing widespread alterations that extend beyond the circuitry evoked by nociceptive stimuli. However, it is important to acknowledge the exploratory nature of these findings and their interpretive challenges. Future research would benefit from multimodal approaches combining rs-fMRI with task-based paradigms, structural imaging, and neurophysiological techniques.

4.5.2.2 fMRI Processing

Deciphering true neuronal signal from noise in fMRI data is an ongoing challenge. Time series extracted from fMRI can be contaminated with fluctuations caused by other physiological processes, such as respiration and cardiac pulsation, and data collection issues including hardware instabilities and artifacts. To mitigate this, much effort has been dedicated to designing acquisition protocols and post-acquisition processing pipelines that remove as much noise as possible while retaining true signal. Common steps include motion correction, slice timing correction, spatial and temporal filtering, and global intensity removal.

Motion is a particular concern in fMRI data. Signal can vary significantly in adjacent voxels, meaning that any motion from one whole-brain volume to the next can lead to poor spatial localization in the final analysis. One step to mitigate this involves image registration whereby all images collected during the scan are aligned to a reference, such

as the first, middle, or mean image of the time series. Further motion correction may be applied by modeling motion estimates based on parameters of the registration and regressing these estimates from the data. However, retrospective correction methods can fail if motion is extreme, necessitating researchers to exclude parts of time series (called "scrubbing") and sometimes entire datasets from analysis. This highlights the need to mitigate motion contamination at the data acquisition stage. To this end, prospective techniques have been developed, including real-time adjustment of imaging gradients in response to optical tracking of subject movement [78].

Slice timing correction is an attempt to mitigate the impacts of planar imaging on the time series. Scanners may acquire different slices of a volume in a sequential or interleaved order, meaning that images of adjacent voxels may be acquired hundreds of milliseconds apart. Although this is a relatively short amount of time, it is possible for neuronal activity dynamics to change in this interval. Slice timing correction involves temporally realigning all slices, typically by interpolating signal across spatially adjacent slices. The utility of this step is disputed, with some arguing that the slice time interval is relatively short compared to the length of the hemodynamic response measured by BOLD fMRI [78].

The main purpose of spatial smoothing is to improve signal to noise (SNR), which is directly proportional to voxel size, although this comes at the loss of spatial specificity and is not recommended when investigating smaller brain regions. This is usually performed with a 3D Gaussian kernel. Temporal filtering is performed to remove frequencies of non-neuronal origin through the application of high and low pass filters. Common sources of low frequency noise include scanner instabilities and settling of the head over the course of the scan, while high frequency noise comes from blood and CSF flow [78].

Global signal removal is a controversial topic in the field, especially as it relates to resting state fMRI. The term "global signal" refers to the mean time course over all voxels, and removal techniques include subtraction, regression, and normalization [83]. Global signal removal is an efficient method for cleaning artifacts and can be used to increase sensitivity to regional activations during tasks and control for scanner setting changes across runs. However, global signal is likely to contain a neuronal component as well, the removal of which must be considered when interpreting results. Additionally, global signal removal can introduce anti-correlations, which some argue may be an artifact of processing rather than a true representation of neuronal dynamics.

The inclusion of fMRI processing steps and the order in which they are performed can greatly impact the final analysis. This high degree of flexibility has likely contributed to the poor reproducibility plaguing psychology. In response, there has been growing emphasis on standardization and transparency within the neuroimaging community, leading to the development of common practices such as the Brain Imaging Data Structure (BIDS) and associated software tools [84, 85]. Unless otherwise noted, the neuroimaging data presented in this dissertation have been processed using these "BIDS apps", including *fMRIPrep* for basic preprocessing, *MRIQC* for image quality assessment, and *Nilearn* for confound removal and statistical analyses [86, 87, 88, 89, 90].

4.6 The "connectome"

All of the studies presented in the following chapters involve applications of a statistical object called the connectivity matrix, or "connectome". Given the growing popularity of this

term in many contexts, it is important to establish a definition as it applies to this body of work. Here, a connectome broadly refers to a matrix storing pairwise relationships between things. It is essentially a representation of a graph or network in formal mathematic terms, i.e. a triple of sets of nodes, edges, and "incidence" relations that associate each edge with an unordered pair of nodes [91].

The term "connectome" was first used in an academic context in 2005, when Olaf Sporns and colleagues published a position paper calling to establish a database of all neuronal connections in the human brain [92, 93]. Such mapping would formalize the conceptualization of the brain as a network, enabling the use of analytic tools borrowed from the field of graph theory and eventually leading to the birth of "connectomics" as its own research discipline [93]. Today, the term is still largely associated with neuroscience, popularized by the 2010 launch of the Human Connectome Project (HCP), a large neuroimaging effort funded by the National Institutes of Health (NIH) [94]. The connectome is not limited to humans, however; to date, complete neuronal wiring diagrams (i.e. structural connectomes) have been documented for several small organisms such as *Caenorhabditis elegans* (C. elegans, a nematode) [95, 96], *Drosophila melanogaster* (the common fruit fly) [97, 98], and parts of the mouse cortex [99, 100].

The connectome can represent data on any scale, from individual neuronal connections to white matter tracts spanning the whole brain. It can also represent data of varying modalities; a "structural connectome" can encode the physical connections between nodes, while a "functional connectome" may present similarity of dynamic signals, such as regional time series derived from brain fMRI. This dissertation will present many different applications of the connectome to reveal novel information about biological processes. First I present a

simple mathematical model for mapping brain activity patterns from structural networks. I will then show how individual differences in brain functional connectomes can predict whole-body somatosensory symptoms in patients with chronic low back pain. Finally, I apply the principles of connectomic analysis to a novel body part, the knee, in order to reveal patterns of long term cartilage thickness changes related to healthy aging and osteoarthritis development.

Chapter 5

Improving brain structure-function model with latent structural connectivity

The following manuscript is reformatted and reproduced with full permission from the publisher. It appeared as:

Cummings, J. A., Sipes, B., Mathalon, D. H., & Raj, A. (2022). Predicting Functional Connectivity from Observed and Latent Structural Connectivity via Eigenvalue Mapping. Frontiers in Neuroscience, 16, 810111. https://doi.org/10.3389/fnins.2022.810111

5.1 Introduction

Determining the correspondence between the brain's structural white matter connectivity (SC) network and its temporally dependent functional connectivity (FC) network is of fundamental import in neuroscience and may inform characteristics of brain disease. While complex dynamic neural activity must propagate over a static structural network, whether and to what extent the correlation structure of the latter can be directly predicted from the

former is a subject of active interest. Recently, graph based methods have been employed to relate the brain's SC to FC. Evolution of the structural and functional networks have been investigated using graph theoretical statistics [101, 102, 103, 104, 105]. Structurally coupled neural mass models (NMMs) use the brain's connections to couple anatomically connected neuronal assemblies and perform lengthy numerical simulations to approximate the brain's local and global activity. Using these techniques such simulation methods are able to achieve moderate correlation between simulated and empirical FC [106, 107, 108, 109, 110]. However, stochastic simulations are unable to provide a closed form solution and inherently suffer from lack of interpretability since dynamics are only achieved from iterative optimizations of high dimensional NMM parameters.

Due to these challenges many laboratories are exploring parsimonious models that leverage the brain's macroscale linearity through a relationship between structural and functional network eigenmodes. The key driving insight here is that the brain's activity is macroscopically linear to a large extent [111, 112, 113]. An early example of this was our proposal of using low-dimensional processes involving diffusion or random walks on the structural graph as a simple means of simulating FC from SC [111]. Graph diffusion models naturally employ the Laplacian of SC and have been generalized to yield spectral graph models whereby Laplacian eigenspectra were sufficient to reproduce functional patterns of brain activity using only a few eigenmodes [114, 115, 112]. Thus, a Laplacian matrix representation of a network can be used to find characteristic properties of the network, and its eigenvectors form an orthonormal basis that can represent any arbitrary patterns on the network. The Laplacian eigenmodes are therefore emerging as the substrate on which functional patterns of the brain may be established via several manners of network transmission [111, 114, 115, 116, 117].

A recent study from our group expanded this graph modeling work to accommodate phase delays in SC and proposed a complex Laplacian [118]. Higher-order walks on graphs have also been proposed as a method for accounting for both direct and indirect connections on the structural network; typically these methods involve a series expansion of the graph adjacency or Laplacian matrices [119, 120, 105]. Not surprisingly, the diffusion and series expansion methods are closely related, and most of these approaches may be interpreted as special cases of each other [116, 121, 122]. Recently, dynamically varying metrics quantifying structural eigenmode coupling strength to functional patterns were also introduced [117]. Whether using graph diffusion, eigenvalue mapping or series expansion, the eigen structure of the graph is integral to these models of spread.

However, no model using structural information outperforms a model that simply estimates a subject's connectivity matrix (connectome) as a function of the group average [121]. Previous studies that use parsimonious and global eigenvalue mapping techniques have reported correlations between predicted and empirical FC of only around $R \approx 0.2 - 0.4$. This implies that the majority of variance in FC is not being explained by SC-based models. Although much higher R values have been reported [119, 120, 105, 121], these studies typically involve large numbers of model parameters or do not attempt to predict unseen data. Thus, current models can be either parsimonious or accurate, not both.

5.1.1 Current contributions

In this study, we aimed to advance the eigenvalue mapping method of SC-FC relationship via two significant innovations. First, as demonstrated in Results (Figure 5.1), the exponential

relationship between the eigenvalues of SC and FC does not always hold, and especially low SC eigenvalues deviate from this relationship. There may be many reasons for this, not least of which is likely due to challenges in correctly estimating latent structural connections via diffusion-weighted MRI (DWI) tractography. Therefore we explore non-monotonically-decreasing eigen relationships, as typified by the well known Gamma function. Second, we investigate how the accuracy of linear structure-function models would be impacted by the incorporation of biologically relevant latent structural connections - small fibers between adjacent regions and gray-to-gray connections along non-myelinated axons [123]. Accounting for interhemispheric connectivity is yet another challenge presented when modeling the brain's function from the underlying structure. Within the brain, most interhemispheric fibers are contained in the corpus callosum. However, the presence of bilateral connectivity patterns in individuals without this structure suggests the existence of yet other sources of interhemispheric integration [124], e.g., the brainstem, which plays a critical role in coordinating neural activity [125, 126].

Therefore in this study we use Gamma-shaped eigenvalue mapping, followed by addition of adjacency and supplemental inter-hemispheric connectivity strength between homologous left and right structures in our structural connectome, and investigate the impact of these enhancements on the structure-function model. Since these additions do not have the same scale as the DWI-derived SC, it is not possible to determine *a priori* the scale of the additional elements. Therefore we sweep all our analysis results over a large range of weights, which are then optimized such that the predicted FC using these augmented SC matrices may achieve the best association with empirical FC. We show that the above enhancements lead to a SC-FC model that retains all the key benefits of the previous eigenvalue mapping

methods (e.g., parsimony, generalizability and interpretability) while greatly enhancing the ability to predict empirical FC. We applied our methods to two independent datasets of structural and functional matrices and achieved very similar performance on both.

5.2 Materials and Methods

5.2.1 Participants

Data were collected as part of a multi-site longitudinal study aimed at better understanding the brain mechanisms underlying psychosis development and provided by our collaborators in the Brain Imaging and EEG Laboratory at the San Francisco VA Medical Center. Sample includes fMRI and DTI data from 83 healthy controls (HC) and 49 early schizophrenia (ESZ) patients. ESZ participants met DSM-IV criteria for schizophrenia or schizoaffective disorder and were within 5 years of disease onset. Data from only the healthy group were used for the majority of this study except for comparison in Figure 7.

5.2.2 UCSF fMRI

Functional MRI data collection was completed at the UCSF Neuroimaging Center using a Siemens 3T TIM TRIO. Resting state data were collected with the following parameters: T2*-weighted AC-PC aligned echo planar imaging (EPI) sequence: TR = 2,000 ms, TE = 29 ms, flip angle = 75, FOV = 240 x 240, slice thickness = 3.5 mm, acquisition time = 6:22.

5.2.2.1 Anatomical data preprocessing

The T1-weighted (T1w) image was corrected for intensity non-uniformity (INU) with `N4BiasFieldCorrection` [127], distributed with ANTs 2.3.3 [128, RRID:SCR_004757], and used as a T1w-reference throughout the workflow. The T1w-reference was then skull-stripped with a *Nipype* implementation of the `antsBrainExtraction.sh` workflow (from ANTs), using OASIS30ANTs as target template. Brain tissue segmentation of cerebrospinal fluid (CSF), white-matter (WM) and gray-matter (GM) was performed on the brain-extracted T1w using `fast` [129, FSL 5.0.9, RRID:SCR_002823]. Volume-based spatial normalization to a standard space (MNI152NLin2009cAsym) was performed through nonlinear registration with `antsRegistration` (ANTs 2.3.3), using brain-extracted versions of both T1w reference and the T1w template. The *ICBM 152 Nonlinear Asymmetrical template version 2009c* [[130, RRID:SCR_008796]; TemplateFlow ID: MNI152NLin2009cAsym] was selected for spatial normalization.

5.2.2.2 Functional data preprocessing

Preprocessing was performed using *fMRIPrep* 20.2.3 ([86]; [87]; RRID:SCR_016216), which is based on *Nipype* 1.6.1 ([131]; [132]; RRID:SCR_002502). First, a reference volume and its skull-stripped version were generated using a custom methodology of *fMRIPrep*. The BOLD reference was then co-registered to the T1w reference using `flirt` [FSL 5.0.9, 133] with the boundary-based registration [134] cost-function. Co-registration was configured with nine degrees of freedom to account for distortions remaining in the BOLD reference. Head-motion parameters with respect to the BOLD reference (transformation matrices, and six

corresponding rotation and translation parameters) are estimated before any spatiotemporal filtering using `mcflirt` [FSL 5.0.9, 135]. BOLD runs were slice-time corrected using `3dTshift` from AFNI 20160207 [136, RRID:SCR_005927]. The BOLD time-series (including slice-timing correction when applied) were resampled onto their original, native space by applying the transforms to correct for head-motion. These resampled BOLD time-series will be referred to as *preprocessed BOLD in original space*, or just *preprocessed BOLD*. The BOLD time-series were resampled into standard space, generating a *preprocessed BOLD run in MNI152NLin2009cAsym space*. First, a reference volume and its skull-stripped version were generated using a custom methodology of *fMRIPrep*. Automatic removal of motion artifacts using independent component analysis [ICA-AROMA, 137] was performed on the *preprocessed BOLD on MNI space* time-series after removal of non-steady state volumes and spatial smoothing with an isotropic, Gaussian kernel of 6mm FWHM (full-width half-maximum). Corresponding "non-aggressively" denoised runs were produced after such smoothing. Additionally, the "aggressive" noise-regressors were collected and placed in the corresponding confounds file. Several confounding time-series were calculated based on the *preprocessed BOLD*: framewise displacement (FD), DVARS and three region-wise global signals. FD was computed using two formulations following Power (absolute sum of relative motions, [138]) and Jenkinson (relative root mean square displacement between affines, [135]). FD and DVARS are calculated for each functional run, both using their implementations in *Nipype* [following the definitions by 138]. The three global signals are extracted within the CSF, the WM, and the whole-brain masks. The head-motion estimates calculated in the correction step were also placed within the corresponding confounds file. Frames that exceeded a threshold of 0.5 mm FD or 1.5 standardised DVARS were annotated as motion outliers. All

resamplings can be performed with *a single interpolation step* by composing all the pertinent transformations (i.e. head-motion transform matrices, susceptibility distortion correction when available, and co-registrations to anatomical and output spaces). Gridded (volumetric) resamplings were performed using `antsApplyTransforms` (ANTs), configured with Lanczos interpolation to minimize the smoothing effects of other kernels [139]. Non-gridded (surface) resamplings were performed using `mri_vol2surf` (FreeSurfer).

Many internal operations of *fMRIPrep* use *Nilearn* 0.6.2 [89, 90, RRID:SCR_001362], mostly within the functional processing workflow. For more details of the pipeline, see `https://fmriprep.readthedocs.io/en/latest/workflows.html`the section corresponding to workflows in *fMRIPrep*'s documentation.[1]

5.2.2.3 Functional network generation

Average functional time series were extracted from 86 regions of interest (68 cortical, 18 subcortical) as defined by the Desikan-Killiany atlas [140]. Regional time series were bandpass filtered from 0.01 to 0.25Hz for functional connectivity analysis. Entries of FC matrices were defined as the Pearson correlation coefficient between the time series of each pair of brain atlas regions. All matrices were normalized by dividing by the sum of all entries.

[1]Copyright Waiver: The above boilerplate text was automatically generated by *fMRIPrep* with the express intention that users should copy and paste this text into their manuscripts *unchanged*. It is released under the CC0 license.

5.2.3 HCP Structural Connectivity

Due to the challenges, noise and processing issues involved in DWI acquisition and analysis on individual subjects, we chose to use a template structural connectome of healthy subjects. Therefore we obtained openly available diffusion MRI data from the MGH-USC Human Connectome Project to create an average template connectome [141]. The data acquisition and pre-processing of this cohort are thoroughly described elsewhere by the HCP consortium, e.g. [141].

5.2.3.1 Structural Connectivity Network Calculation

We constructed structural connectivity networks according to the Desikan-Killiany atlas where the brain images were parcellated into 68 cortical regions and 18 subcortical regions as available in the FreeSurfer software [142, 140]. The processing pipeline followed conventional and well-established procedures. Specifically, *Bedpostx* was used to determine the orientation of brain fibers in conjunction with *FLIRT*, as implemented in the *FSL* software [143]. Tractography was performed using *probtrackx2* to determine the elements of the adjacency matrix. We initiated 1000 streamlines from each seed voxel corresponding to a cortical or subcortical gray matter structure and tracked how many of these streamlines reached a target gray matter structure. The weighted connection between the two structures $c_{i,j}$ was defined as the number of streamlines initiated by voxels in region i that reach any voxel within region j, normalized by the sum of the source and target region volumes. This normalization prevents large brain regions from having extremely high connectivity.

5.2.4 Eigendecomposition Model

$$\frac{dx_i(t)}{dt} = \beta \left(\delta_i^{-1/2} \sum_j c_{i,j} \delta_i^{-1/2}(t) - x_i(t) \right) \tag{5.1}$$

where $c_{i,j}$ is the number of physical connections between the two regions, δ_i is the weighted degree of region i, and β is the decay rate of the system. When expanded to the entire network, this relationship becomes

$$\frac{dx(t)}{dt} = -\beta L x(t) \tag{5.2}$$

The Laplacian L of the structural connectome is defined here as

$$L = I - \Delta^{-1/2} C_s \Delta^{-1/2} \tag{5.3}$$

where C_s is the structural connectivity matrix and Δ is the degree matrix. The solution of Equation 2 can thus be used to estimate the functional connectome as

$$C_f = e^{-\beta L t} \tag{5.4}$$

Spectral graph models like [114] and others take this solution one step further by using the eigenvectors of the structural Laplacian as an orthonormal basis on which FC can be predicted. Following eigendecomposition:

$$L = U \Lambda U^H, \text{with } U = \{\mathbf{u}_i\},\ \Lambda = diag(\lambda_i), i \in [1, N] \tag{5.5}$$

where $\mathbf{u}_i$ are the eigenvectors and λ_i are the eigenvalues of L, we assume that the functional connectome and structural Laplacian share eigenvectors and their eigenvalues are related by an exponential relationship:

$$\lambda_f^{eig} = ae^{-\alpha\lambda_l} + b \tag{5.6}$$

The predicted functional connectome is thus given by

$$C_f^{eig} = a\sum_{i=1}^{N} e^{-\alpha\Lambda_l}\mathbf{u}_i\mathbf{u}_i^H + bI \tag{5.7}$$

The model parameters a, α, b are optimized per subject as the values that minimize the Frobenius norm of the difference between the true functional matrix and the predicted matrix C_f^{eig}.

5.2.5 Gamma Model

While previous modeling approaches using the exponential relationship between the eigenvalues give good results and have the benefit of being based on an implicit underlying linear model of functional dynamics [114], we have observed that frequently the diagonal elements of the projection matrix $U^H FU$ are not monotonically decreasing, as would be expected for a strictly exponential decay. Indeed, it was noted by [114] that the deviations from exponential fits of the eigenvalues might be due to global signal in FC and under-estimation of interhemispheric connections in SC. Whatever the reason, it is likely that other functional forms of the eigenvalue relationship might prove useful for certain subjects. In view of these points, we therefore explored a different mapping that retains the parsimony of the original

eigen model but is able to produce non-monotonic relationships. We chose the Gamma function $\Gamma(x|\gamma, k)$, with only a single width parameter γ, keeping the shape parameter at $k = 2$. Hence we define

$$\lambda_f^{\Gamma} = \Gamma(\lambda_l|\gamma, k) \tag{5.8}$$

Then the prediction of FC may be given as before by:

$$C_f^{\Gamma} = \sum_{i=1}^{N} \lambda_{f,i}^{\Gamma} \mathbf{u}_i \mathbf{u}_i^H \tag{5.9}$$

Some examples of the relationship between Laplacian eigenvalues and the projections onto FC are shown in Figure 5.1. An example of the Gamma function on real structure-function pairs is also provided for comparison, along with the previous exponential relationship. Please note, the Gamma function reduces to the exponential for the special case of $k = 1$.

5.2.6 Parameter Inference

The model parameters, denoted by θ - which consists of a, α, b for the eigendecomposition model, and λ for the Gamma function model - are optimized per subject as the values that minimize the Frobenius norm of the difference between the true functional matrix and the predicted matrix C_f. In this paper both models C_f^{eig} and C_f^{Γ} will be evaluated. For this purpose we implemented a constrained cost function minimization, available as `fmincon()` in MATLAB version R2019b. The parameters were given lower limits 0 (to ensure positive values). To ensure unique solutions from the inference procedure a small amount of

regularization was added via $\epsilon = 0.001$, to yield the cost function:

$$cost(\theta) = ||F - C_f(\theta)||_F + \epsilon||\theta||_1 \tag{5.10}$$

The cost function was evaluated against the traditional FC F.

5.2.7 Model Evaluation

We report Pearson's correlation R between the true FC matrix and the model-predicted matrix as a metric for model performance. Only the upper triangle, excluding diagonal, of each matrix is used in the calculation.

5.2.8 Adjacency Matrix Addition

We generate a local connectivity matrix in which the entries are a function of the surface area of the boundary shared between each pair of brain regions as defined in the Desikan-Killiany atlas [140]. The resulting matrix, referred to as the Adjacency matrix, is represented in Figure 5.1B. The original atlas image representing a given region is dilated by one pixel radius using the imdilate function in Matlab, and the number of voxels that overlap with a neighboring region in the dilated image are used to weigh the adjacency. This matrix, A, is then added to the original structural connectome with a range of weights w between 0 - 1,

$$C_s^{'} = C_s + wA \tag{5.11}$$

to generate an augmented $C_s^{'}$ to be used as the structural matrix in our model.

5.2.9 Interhemispheric Matrix Addition

We create a binary matrix the same size as the structural connectome in which all entries are zero except at the connection between homologous structures in the left and right lobes. This matrix, shown in Figure 5.1C, is then added to the structural connectome over a range of weights and the result is used in the model as described for the adjacency matrix.

5.3 Results

First we show what the mean SC matrix pertaining to the 86-region Desikan-Killiany parcellation looks like in Figure 5.1. The correlation R between the structural connectome and mean functional connectome is 0.37, while the R for each individual subject ranged from 0.18 - 0.32 with a mean of 0.24. The key driver of low correlations between the two is evident from a visual inspection of Figures 5.1A and 5.2C - lack of inter-hemispheric connectivity in SC, which is prominently present in FC. The regional adjacency matrix is shown alongside, and for reference the set of inter-hemispheric connections between left-right homologs is also shown. It is the inter-hemispheric connections that are largely unobserved in SC, and these are the connections whose addition in subsequent analysis have the highest chance of improving the structure-function relationship.

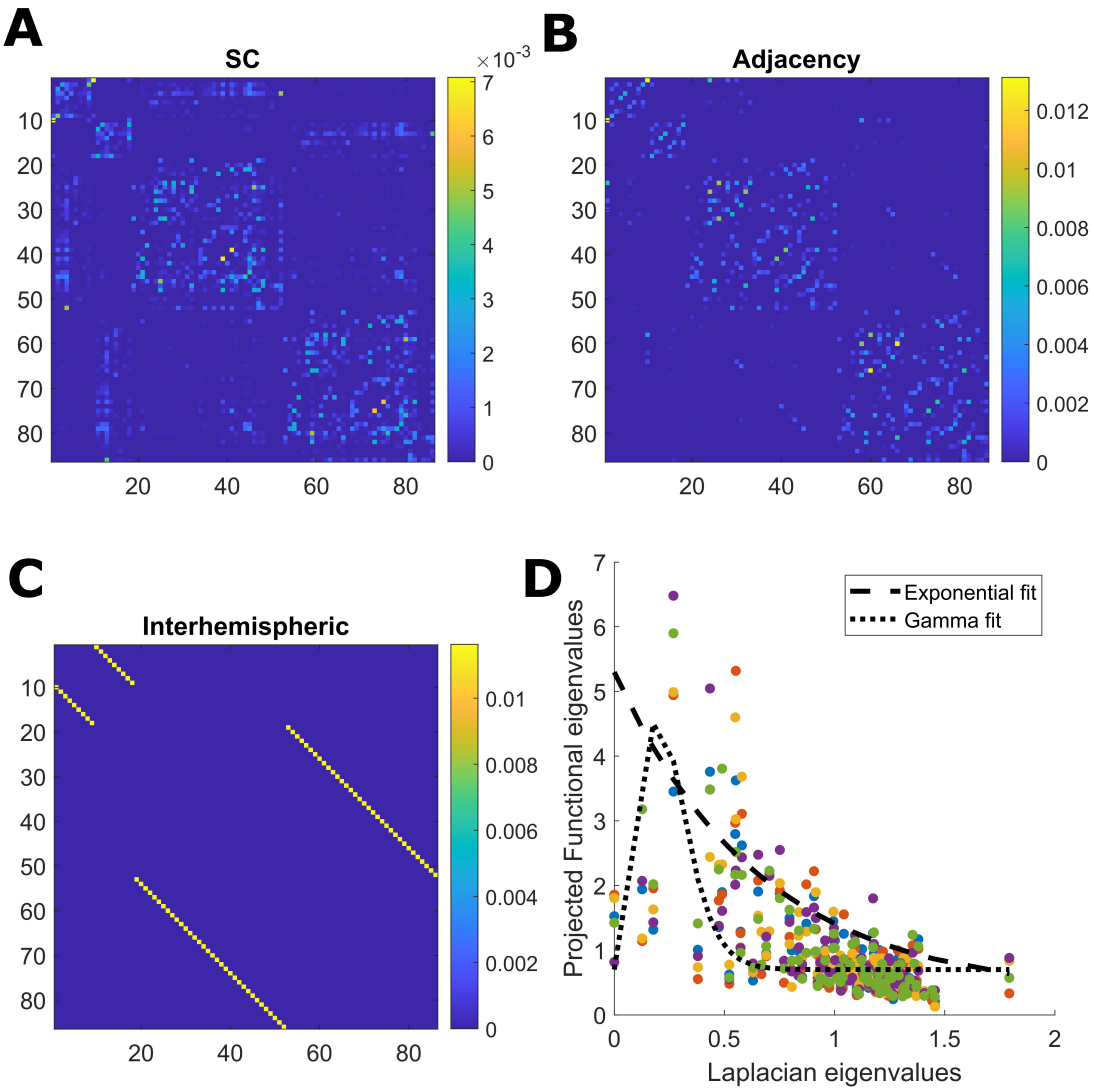

Figure 5.1 Visualization of connectivity matrices and scatter plot depicting structure-function relationship. A) Structural connectome derived from DTI. B) Adjacency matrix derived from the surface area of boundary between regions in brain atlas. C) Interhemispheric matrix representing connections between left and right homologous brain structures. D) Scatter plot of relationship between Laplacian eigenvalues and the projections onto FC given by UFU^H. Colors represent data from each of five different subjects. Dashed line provides an example of exponential fitting, while dotted line represents gamma fitting.

In order to motivate the use of eigen mapping between SC and FC, we show in Figure 5.1D some examples of the relationship between Laplacian eigenvalues and the projections onto FC given by UFU^H. It may be noted that while at the level of mean FC the relationship is roughly monotonic and well-described by the exponential decay function, this is not so at individual subjects level. In those cases, some small λ_i deviate from the exponential, and in those cases the exponential relationship would greatly over-estimate the corresponding entry in FC. To overcome this issue we propose the use of Gamma function as a parsimonious mapping between the eigenvalues. An example of the Gamma function on real structure-function pairs is provided in the figure panel for comparison, along with the previous exponential relationship. The width of the Gamma function is given by the model parameter γ, and it serves to control the range of Laplacian eigenvalues to include in the model.

5.3.1 Performance of gamma and eigendecomposition models

The performance for both the previous eigen model and the proposed Gamma model on our main UCSF dataset were thoroughly evaluated using the stated performance metric Pearson's R. The results of the Gamma model are shown in Figure 5.2, and of the exponential model in 5.3. The gamma model yields an R range of 0.22 - 0.42 with a mean of 0.30 (Figure 5.2A). The fitted γ parameter ranged between 0.16 - 0.27 with a mean of 0.22 (Figure 5.2B). The eigen model yields an R range of 0.22 - 0.40 with a mean of 0.28 (Figure 5.3A). Parameter a ranged between 0.10 - 0.34 with a mean of 0.11. Parameter α ranged between 0.18 - 2.64 with a mean of 0.99. Parameter b ranged between -0.14 - 0.001 with a mean of -0.04 (Figure 5.3B).

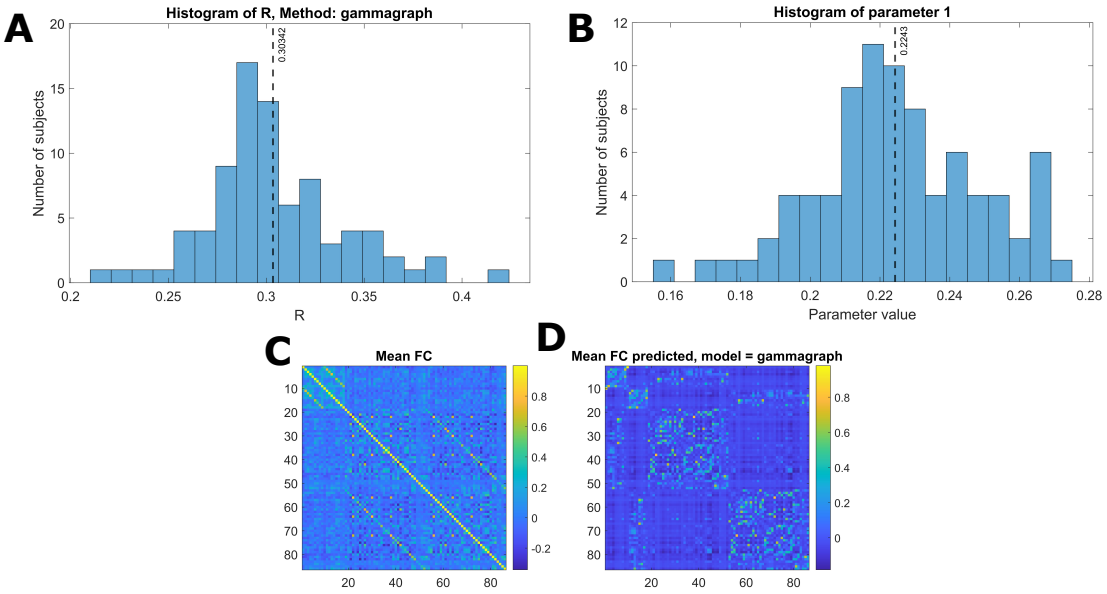

Figure 5.2 Gamma model performance. A) Histogram of R score. B) Histogram of fitted parameter. C) Mean functional connectome over all subjects. D) Mean functional connectome predicted by model

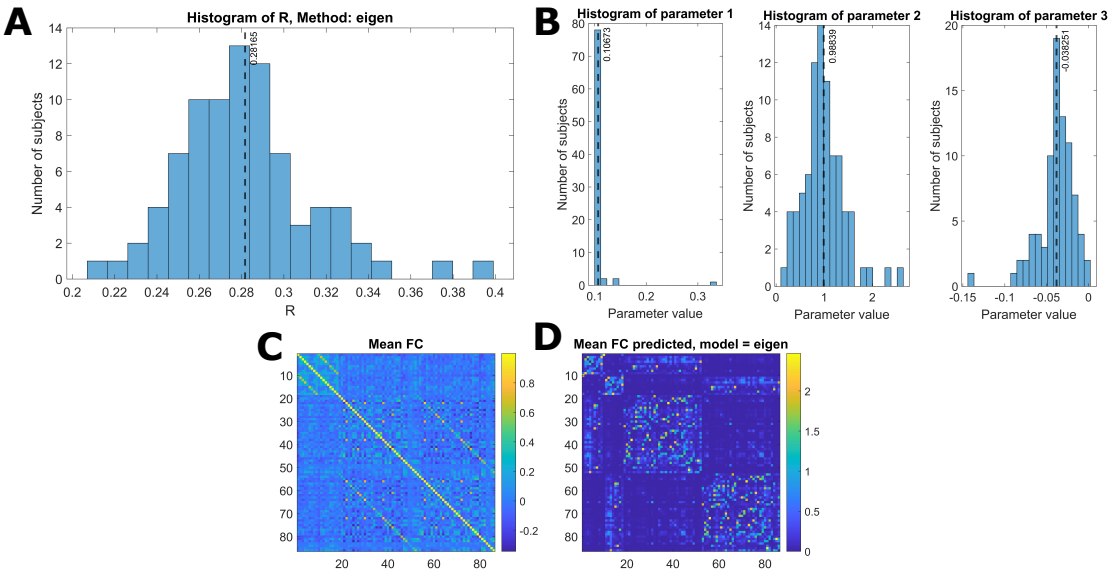

Figure 5.3 Eigen model performance. A) Histogram of R score. B) Histogram of fitted parameter. C) Mean functional connectome over all subjects. D) Mean functional connectome predicted by model

When comparing the two models, several aspects are evident. First, both produce comparable results, which are also comparable to prior published results using similar approaches [114]. However, the second aspect is that the Gamma model has somewhat higher performance. To test this statistically we performed a Fisher's R-to-z transform, followed by a student's t-test. The R scores produced by the two models are significantly different, with a p value of 1.52e-34 and a t statistic of 20.86 as determined by the two-sided t-test. Third, the improvement in the Gamma model came despite fewer model parameters to be inferred - γ compared to $\{a, \alpha, b\}$. Fourth, it may be noted that the inferred parameter distribution of γ is much tighter than that of the exponential model parameters, in terms of coefficient of variation. This implies that the Gamma model has a higher chance of fitting to and correctly predicting unseen cases.

5.3.2 Addition of adjacent and interhemispheric connections

All three structural connectivity networks discussed are shown in Figure 5.1. The structural connectome shown in Figure 5.1A can be thought of as a base to which the adjacency matrix and the interhemispheric matrix were added with varying weights. As shown in Figure 5.4, adjacency matrix had a modest impact on the R score. When applied to all subjects individually, the mean improvement gleaned from the addition of the adjacency matrix was 0.01. The weighting factor for which the model achieved the best R score for individual subjects ranged between 0 and 1 (Figure 5.4A). Model performance using the mean functional connectome ranged between 0.47 and 0.48 over all weights, with a peak R score at a weight of 0.26 (Figure 5.4B). The R between the adjacency matrix and FC is 0.31, and the R between

the adjacency matrix and SC is 0.74. This high correlation is a likely reason for the modest impact of adding one to the other; the adjacency matrix adds little new information.

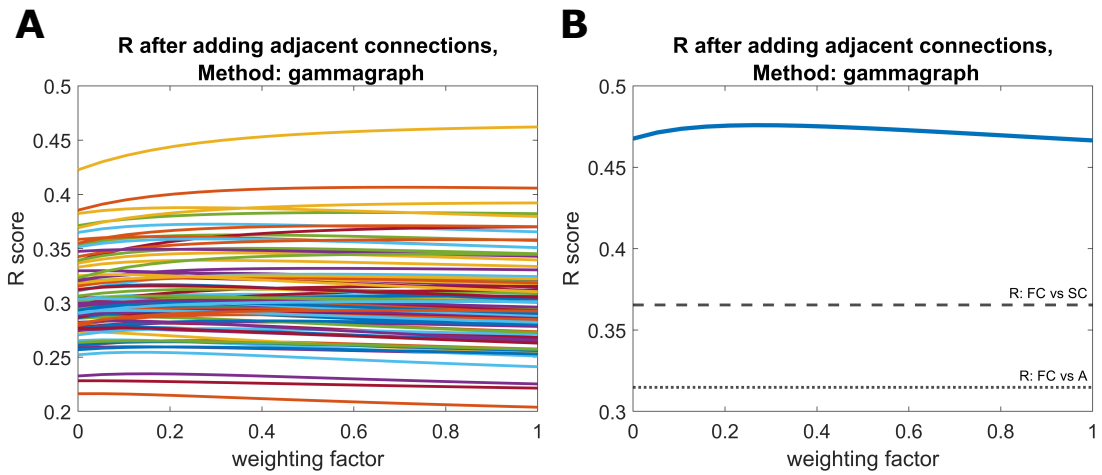

Figure 5.4 Plot of R vs weighting factor as adjacency matrix is added to SC. A) R vs weighting factor for all subjects, with each line representing an individual subject. B) Model performance for the mean functional connectome. Dotted line indicates raw correlation between functional connectome and adjacency matrix. Dashed line indicates correlation between functional connectome and structural connectome.

Adding the interhemispheric matrix had a more substantial impact. For individual subjects, the mean improvement was 0.12. Optimal weighting factors for interhemispheric matrix addition ranged between 0.38 and 0.53 (Figure 5.5A) for individual subjects. At the mean level, the peak R score of 0.66 occurred at a weight of 0.37 (Figure 5.5B). The R between the interhemispheric matrix and FC is 0.40, and the R between the interhemispheric matrix and SC is 0.06.

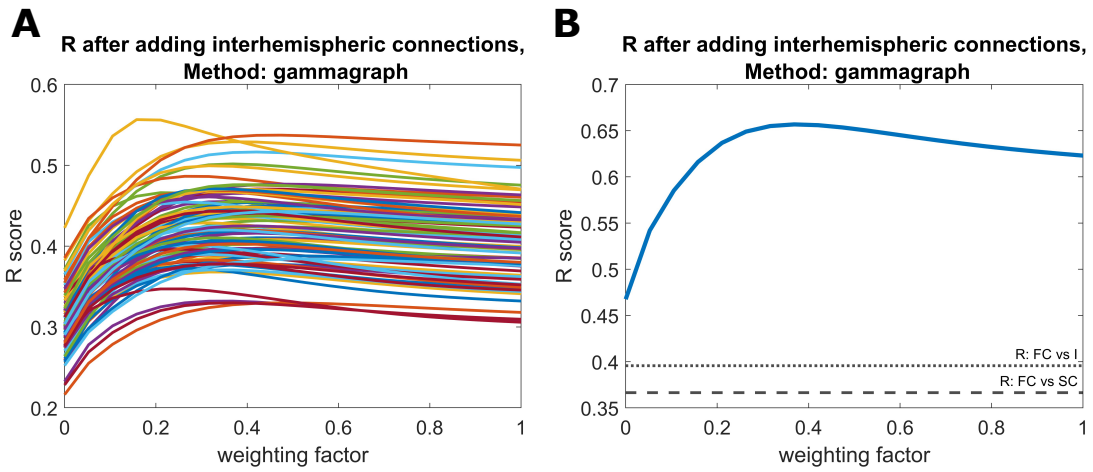

Figure 5.5 Plot of R vs weighting factor as interhemispheric matrix is added to SC. A) R vs weighting factor for all subjects, with each line representing an individual subject. B) Model performance for the mean functional connectome. Dotted line indicates raw correlation between functional connectome and interhemispheric matrix. Dashed line indicates correlation between functional connectome and structural connectome.

Figure 5.6 shows the results of applying the gamma model to all subjects using an "optimal" structural connectome comprised of the original structural connectome template and both the adjacency and interhemispheric matrices added with a weighting factor of 0.3. R values range between 0.31 - 0.58 with a mean of 0.42 (Figure 5.6A). These R values were compared to those obtained without including local and interhemispheric connections by applying the two-sided t-test to the results of a Fisher's R-to-z transform as previously described. The results are statistically significant with a p value of 8.26e-61 and a t statistic of -46.62. The fitted γ parameter ranged between 0.10 - 0.21 with a mean of 0.16 (Figure 5.6B).

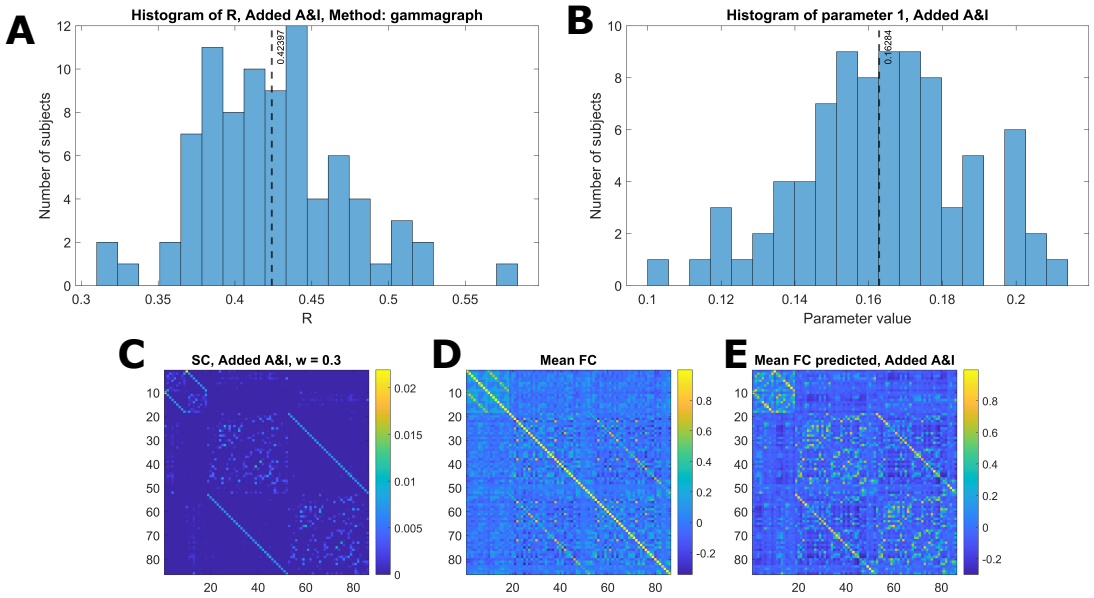

Figure 5.6 Model performance when using structural connectome comprised of original SC, adjacency matrix, and interhemispheric matrix. A) Histogram of R scores. B) Histogram of fitted parameter. C) Optimal structural connectome. D) Mean functional connectome across healthy subjects.

5.4 Discussion

5.4.1 Summary of key results

With this study, we aimed to investigate the relationship between the brain's structural wiring and its functional activity patterns. We present two substantial contributions to the eigen mapping method of relating brain structure and function. First, we propose a model that produces reliable recreations of functional networks by mapping structural Laplacian eigenmodes to functional ones using the well known Gamma function. This method performs as well as previous linear models of a similar nature and requires only one parameter. The models explored in this study are based on previous work that assume that functional connectivity patterns arise as the result of neural activity spreading over the structural

network [111, 114]. Second, we attempt to account for network paths often excluded from graph representations of the structural connectome and provide evidence of interhemispheric connectivity playing a crucial role in driving the structure-function relationship. Finally, we applied the method to multiple datasets of varying connectome sizes, noise levels and disease conditions. Our results on the Schizophrenia cohort in particular support the notion that the relationship between structural and functional eigenmodes is similar in both disease and healthy populations, as was previously reported in epilepsy subjects [144]. However, considering the well-documented differences in structural and functional connectivity seen in schizophrenia, e.g., [145, 146], a more thorough investigation of the structure-function relationship in schizophrenia subjects using personalized structural connectomes would be enlightening. At this stage it is not clear whether fitted parameters of a SC-FC model may be profitably employed as biomarkers of disease.

5.4.2 The shape of SC-FC eigen relationship

The base model used in this study is the exponential structure-function relationship suggested by [114]. This is not merely a statistical observation; instead was shown by [114] to arise from a simple diffusive spread of functional activity along the SC. Mathematically, the diffusion kernel on a graph involves a matrix exponential. This interpretation is not novel; in fact an explicit network diffusion model for SC-FC was also proposed by our group earlier, which also led to a similar eigen relationship [111].

Thus, a spectral graph theory of brain FC is emerging [112, 147, 148], whereby the eigenmodes of structural and functional connectivity are intimately related. The precise

nature of the eigen relationship is however an open question; while early proponents argued in favor of exponential relationship, e.g., [114], more recent work has explored matrix inversion [149] or power relationships with both negative and positive powers [150]. Others have reported more flexible polynomial relationships with higher degrees of freedom [119, 120, 121, 105]; these latter models may be considered to arise from higher order walks on the SC graph.

The first key contribution of the current proposal, the use of the Gamma function, is along these lines. The key motivation behind Gamma is the desirability and need for a non-monotonic relationship with as few parameters as possible. Gamma with $k = 2$ is perhaps the most obvious such choice. The precise shape is less important (see SI for $k > 2$) but it is important to suppress the first few (highest) functional eigenvalues. The reasons for this have been addressed earlier; in a nutshell the deviations from exponential fits of the early eigenvalues are likely due to global signal in FC and under-estimation of interhemispheric connections in SC. The Gamma function demonstrates a better ability than the exponential to select various regions of the Laplacian eigenspectrum. Its width γ serves to control the range of Laplacian eigenvalues to include in the model. The difference from exponential model is that the Gamma model no longer has a simple interpretation as a passive diffusive process, which the exponential model did. Notably, while the best results of the previous work were reported after excluding the first two structural eigenvalues when predicting the full network [114], we used all eigenvalues in the results presented here and did not find significantly different results when restricting the range of eigenvalues experimentally - clearly the Gamma serves to suppress those problematic eigenvectors. Based on the higher R statistics and narrower distribution of parameter fits shown above, we conjecture that the Gamma model has a higher chance of fitting to and correctly predicting unseen cases.

However, there may be other aspects behind Gamma's improvement - in general non-exponential eigen relationships may reflect higher order walks on the structural graph. In future work it would be interesting to explore the trade-off between parsimony (e.g. Gamma) or flexibility (e.g. series expansion). As indicated by [105], series expansion with up to a power of 5 improves greatly upon just a linear relationship. Perhaps a Gamma-style parametrization can achieve higher-order walks with far fewer parameters than the series expansion or polynomial approaches above.

5.4.3 Incorporating latent structural connections

The second key contribution of this study is to investigate how the incorporation of biologically relevant information about latent structural connections would impact the accuracy of linear structure-function models. Hence, it could be that conventional structural connectivity methods do not account for all structural network paths. Structural connectivity matrices are usually derived from DWI, which can only measure long, myelinated axons, representing just one part of the brain's structural network. Growing evidence suggests that local fiber networks within and between cortical layers play just as crucial a role in shaping functional connectivity as long-range white matter connections [123]. However, these networks are largely excluded from current DTI postprocessing methods. Connections within gray matter exhibit a lower FA signal due to their lack of myelination and are difficult to discriminate at average MRI spatial resolutions, as a single gray matter voxel will usually contain many overlapping fibers [151]. The lack of an *in* vivo imaging method for quantifying intracortical connections presents a significant challenge when trying to construct a complete network

representation of the human brain. One alternative solution is to use cortical volume data to approximate intracortical connectivity strength. Building on the method introduced in [115], we incorporated cortical surface regions into the structural connectome and weighed the adjacency of two neighboring regions proportionally to the surface area of the boundary between them.

Accounting for interhemispheric connectivity is yet another challenge presented when modeling the brain's function from the underlying structure. Most functional networks involve both brain hemispheres and exhibit a high degree of symmetry [152, 153], indicating the presence of a robust pathway enabling interhemispheric synchrony. Within the human brain, most interhemispheric fibers are contained in the corpus callosum, a densely packed structure containing both myelinated and unmyelinated fibers with varying diameters terminating in a wide range of cortical regions [154]. Given its complexity, it is likely that callosal fibers are underestimated by current DTI quantification methods. Moreover, the presence of bilateral connectivity patterns in individuals without this structure suggests the existence of yet other sources of interhemispheric integration [155, 156, 152]. Human and macaque studies have suggested that, in the absence of corpus callosum, smaller commissural fiber bundles such as the anterior or posterior commissure are sufficient in preserving interhemispheric functional connectivity [155, 157, 158]. Another possible factor driving interhemispheric synchrony is the existence of subcortical inputs such as the brainstem [158]. One study showed significant attenuation of bilateral functional connectivity in a patient with brainstem ischaemia, underscoring the possibility that subcortical structures play an important role in coordinating neural activity in both hemispheres. Imaging the brainstem is a difficult task, as it is obscured by major arteries and other sources of noise [125, 126], although recent

develops in mapping brainstem structural connectivity make this an exciting area of future research [159, 160].

Our study demonstrates the effect of adding these latent connections. Interestingly, introducing an adjacency matrix had a modest impact on the R score. We speculate the reason for this modest improvement is that adjacency is closely related to structural connectivity ($R = 0.74$). Thus, adding the adjacency matrix adds little new information. However, it would be interesting to repeat this analysis using subject-specific structural connectomes and adjacency matrices.

Adding the interhemispheric matrix had a more substantial impact. For individual subjects, the mean improvement was a highly significant 0.12. It is clear that interhemispheric connections are highly relevant for FC (they have a correlation of 0.40) but are just not present in SC (correlation of 0.06). One may speculate as to whether the addition of these connections compensates for the underestimation of true interhemispheric structural connectivity or acts as a proxy for subcortical inputs and other indirect connections [109]. Regardless, the fact that our SC-FC model shows a dramatic improvement with this addition suggests that this is an indispensable feature that future models of structure-function must tackle. It also highlights the role of left-right correlated sources - an aspect that is currently missing from graph models. Indeed, these correlated sources cannot be ignored even in studies of resting state. Finally, we may speculate that our work can in future studies be used to "invert" the model and infer missing connections that contribute to FC but are missing in SC. Although our current results provide a step in that direction, a comprehensive approach would require additional sparsity constraints and a proper Bayesian inference algorithm.

5.4.4 Study Limitations

As previously noted, one limitation of this work is the use of a template structural connectome and adjacency matrix. While this allows for higher interpretability, a future direction of this work would involve repeating these analyses with all subject-specific data. This would be especially interesting in clinical applications where subjects may exhibit different structural or functional properties. Another direction of future research would involve a more thorough investigation of the interhemispheric connections and their impact on generating functional connectivity, perhaps varying the weights by region. Although previous studies indicate robustness of the structure-function model to changes in the processing pipeline (e.g. [121]), it would be useful to investigate the impact of using different DWI generation techniques and finer-grained parcellation schemes. We also hope to apply these findings to a dynamic functional connectivity analysis in the future. We additionally acknowledge that the current work does not constitute a predictive model, though it is a step in that direction. Despite these limitations, we believe that these findings present advancements in our understanding of the relationship between brain structure and function.

5.5 Conclusions

This works presents two substantial contributions to the eigen mapping method of relating brain structure and function. First, we propose a model that produces reliable recreations of functional networks by mapping structural Laplacian eigenmodes to functional ones using the well known Gamma function. This method performs as well as previous linear models of a similar nature and requires only one parameter. Second, we attempt to account for

network paths often excluded from graph representations of the structural connectome and provide evidence of interhemispheric connectivity playing a crucial role in driving the structure-function relationship.

Chapter 6

Exploring the brain-body relationship in chronic lower back pain

6.1 Introduction

Low back pain (LBP) is the leading cause of disability worldwide, with approximately 90% of LBP patients classified as "non-specific" [28, 29]. This diagnostic ambiguity, coupled with the limited utility of structural imaging findings, which are prevalent in both symptomatic and asymptomatic individuals, has led to numerous ineffective, invasive, and costly interventions [31]. Despite the biopsychosocial model's growing adoption and the implementation of multidisciplinary treatment approaches, clinical outcomes remain modest [161], underscoring the critical need to identify distinct pain phenotypes that could benefit from targeted interventions.

Neuroscience may provide some guidance toward this goal. A growing body of evidence associates chronic LBP with structural and functional changes in the nervous system when

compared to pain free individuals [162, 163, 164]. Changes have been shown to coincide with the transition from acute to chronic pain and may even predict someone's likelihood to transition after injury [54, 65]. Additionally, studies have suggested that some neurobiological signatures may normalize after successful pain treatment [165].

While numerous studies have investigated neurobiological differences between chronic low back pain (LBP) patients and healthy controls, significantly less work has focused on parsing sources of phenotypic variation within the chronic LBP population itself. Despite widespread adoption of the mechanistic categorization framework proposed by the International Association for the Study of Pain (IASP), the neurobiological signatures underlying these distinct clinical presentations remain poorly understood. The complexity of these signatures is evident across pain types: the thalamus shows inconsistent involvement in neuropathic pain, with studies reporting both hyper- and hypoactivity [64, 166]; both neuropathic and nociplastic profiles demonstrate higher neuroimmune activity in S1 and stronger S1-thalamus functional connectivity compared to nociceptive types [167]; and nociplastic pain (recently adopted as a third IASP category) appears characterized by inhibited descending pathways and broad sensory processing abnormalities [6], making it particularly important for treatment planning [8]. These heterogeneous findings suggest that multivariate analytical approaches may be better suited to capturing the complex neurobiological patterns that differentiate pain mechanisms, ultimately aiding in more precise treatment planning for chronic pain patients.

In recent years, canonical correlation analysis (CCA) has risen to prominence for its ability to reveal complex relationships in multi-modal, high-dimensional data. CCA is a multivariate statistical method that maximizes the correlation between two or more datasets, making it uniquely suited for neuroscience datasets, which often contain many different types

of data (e.g. neuroimaging, behavioral, genetic, etc.) from the same subjects [168, 169, 170, 171]. Inspired by recent studies using CCA to stratify heterogeneity within a disease population, we hypothesized that the method may reveal hidden phenotypes in our LBP cohort [172, 173].

While numerical pain scales like the visual analog scale (VAS) or numeric rating scale (NRS) would provide the most direct analogy to behavioral measurements used in previous CCA studies, these are insufficient for capturing the full dimensionality of the chronic pain experience [174]. In contrast, self-reported pain maps contain a wealth of information but have long evaded use in research due to a lack of standardization and quantification practices. However, growing interest in the link between pain widespreadedness and central sensitization has brought a new focus on body maps as a measurement tool [10, 175, 7]. Body map data has already proven useful in guiding treatment planning, with those reporting a greater spatial extent of pain showing an increased likelihood to respond well to centrally acting therapies such as analgesics [8]. Thus, body maps seemed an ideal source from which we could mine measurements that would best capture the individual variability in our LBP subjects.

The goal of our study was to identify neurological signatures corresponding to unique somatosensory profiles in a dataset of nearly 300 subjects with chronic low back pain. To that end, we developed a computational pipeline for extracting meaningful measurements from hand-drawn body maps of three sensory abnormalities (pain, numbness, and pins and needles) while maintaining a balance between sensitivity and parsimony. We then applied regularized CCA to identify axes of common variability between resting state functional connectivity data and these body map-derived metrics, termed "brain-body dimensions", which were

validated in held-out test sets using a bootstrapped cross-validation procedure. Some of these dimensions show remarkable correspondence with the established mechanistic pain categories, providing new insight into the neurobiological signatures of these phenotypes. The model was also shown to predict pain reports in a novel data set of chronic pain patients, suggesting that they may not be unique to LBP patients. Finally, we investigated the relationship between these brain-body dimensions and several clinical, demographic, and psychosocial risk and prognostic factors.

To our knowledge, this study represents the first investigation to show an association between whole-body somatosensory patterns and brain connectivity recorded at rest. Our results provide new evidence supporting a link between chronic pain and brain network reorganization measurable in absence of any task or pain stimulus. These findings also underline the complexity of chronic LBP, showing that no single brain connectivity feature or somatosensory profile can describe all LBP subjects. We hope that these results will encourage further efforts toward stratifying the heterogeneous LBP population into clinically meaningful phenotypes with the ultimate goal of providing personalized effective treatments.

6.2 Methods

6.2.1 Participants

The data used in this analysis were collected as part of the ongoing comeBACK study (NIH Back Pain Consortium-BACPAC, 1U19AR076737-01), a multi-site longitudinal study of chronic lower back pain [176]. All participants are adults age ≥ 18 who had experienced low

back pain for at least three months and at least half the days of the past six months at the time of recruitment and who reported that the low back was their dominant pain location. Inclusion criteria were developed with the intention to enroll non-specific cLBP patients, meaning that participants with a history of disorders such as cancer, spine infection, vertebral fracture, and several autoimmune diseases were excluded. Other exclusion criteria included common contraindications for MRI (claustrophobia, internal hardware) and an inability to complete all time points [176].

From an initial cohort of 449 cLBP patients, we selected subjects for whom body maps and baseline fMRI were available and who were not taking opioid medication at the time of data collection. This resulted in a dataset of 275 individuals (117 males and 158 females, age: 54 $\pm$ 16, mean $\pm$ SD, age range: 18–91 years old)

6.2.2 Body maps acquisition

Participants filled out body maps on paper in front of an examiner during the baseline visit. They received blank diagrams of the front and back of a body and were instructed to shade in all areas where they had felt each of three sensations (pain, numbness, and pins and needles) over the past 7 days.

6.2.3 Body maps processing

To convert the body maps data into vector input suitable for CCA analysis, we aimed to extract a low-dimensional set of somatosensory patterns with which all subjects' data could be described. To this end, a processing pipeline was designed with the intention of eliminating

noise (e.g. inherent subject differences in marking style) while retaining valuable signal (e.g. a larger mark may indicate more salient pain). This pipeline is depicted in Figure 6.1.

For each of the three sensations (pain, numbness, and pins and needles), raw pixel counts were summed within 98 grid sections on the front and back, resulting in 196 grid section values for each sensation per subject. A two-step normalization procedure was applied to the raw pixel count data to achieve comparable values across all grid sections and subjects. This involved first dividing each section's pixel count data by the total number of pixels in that section (i.e., column normalization) and then scaling each subject's data between 0 and 1 (i.e., row normalization).

Next, in order to increase SNR and further account for inter-subject variability, we aimed to summarize section values within meaningful anatomical regions. A data-driven approach was used to assign grid sections to larger anatomical regions based on group-level similarity in pixel count patterns while accounting for spatial proximity. Spatially-aware clustering was performed using a method from graph theory called community detection. First, a graph (similarity matrix, S) was constructed as the covariance matrix (Cov) of all subjects' pixel data weighted by a spatial adjacency matrix (A), as defined below:

$$S = (1 - \alpha)Cov + \alpha(A) \tag{6.1}$$

A was constructed such that sections that share a boundary in 2D (front or back grid) have edge value = 1 and mirrored front-back sections have edge value = 0.5. Communities were detected using the Louvain Community Detection Algorithm implemented in the python package *NetworkX* [177]. Values of α were swept through 0-1 and the value that optimized

modularity was chosen. The algorithm was then rerun using the optimal α value, and the mean normalized pixel count percentage was taken for all sections within each community for all three sensations.

Finally, nonnegative matrix factorization (NMF) was performed on these data to identify a sparse set of body map factors, referred to as "body map patterns" or simply "patterns". The optimal number of NMF factors was determined using 5-fold cross-validation over 10 iterations with a range of factors from 2 to 10, selecting the number that minimized the acceleration of the cross-validation error curve (e.g. the elbow method). Descriptive statistics for each of the patterns are provided as the percent weight applied to each feature in the input "body part-sensation" space, with feature weights constituting more than 5% reported. Subjects' values for all of the resulting body map patterns were used as input to the rCCA algorithm.

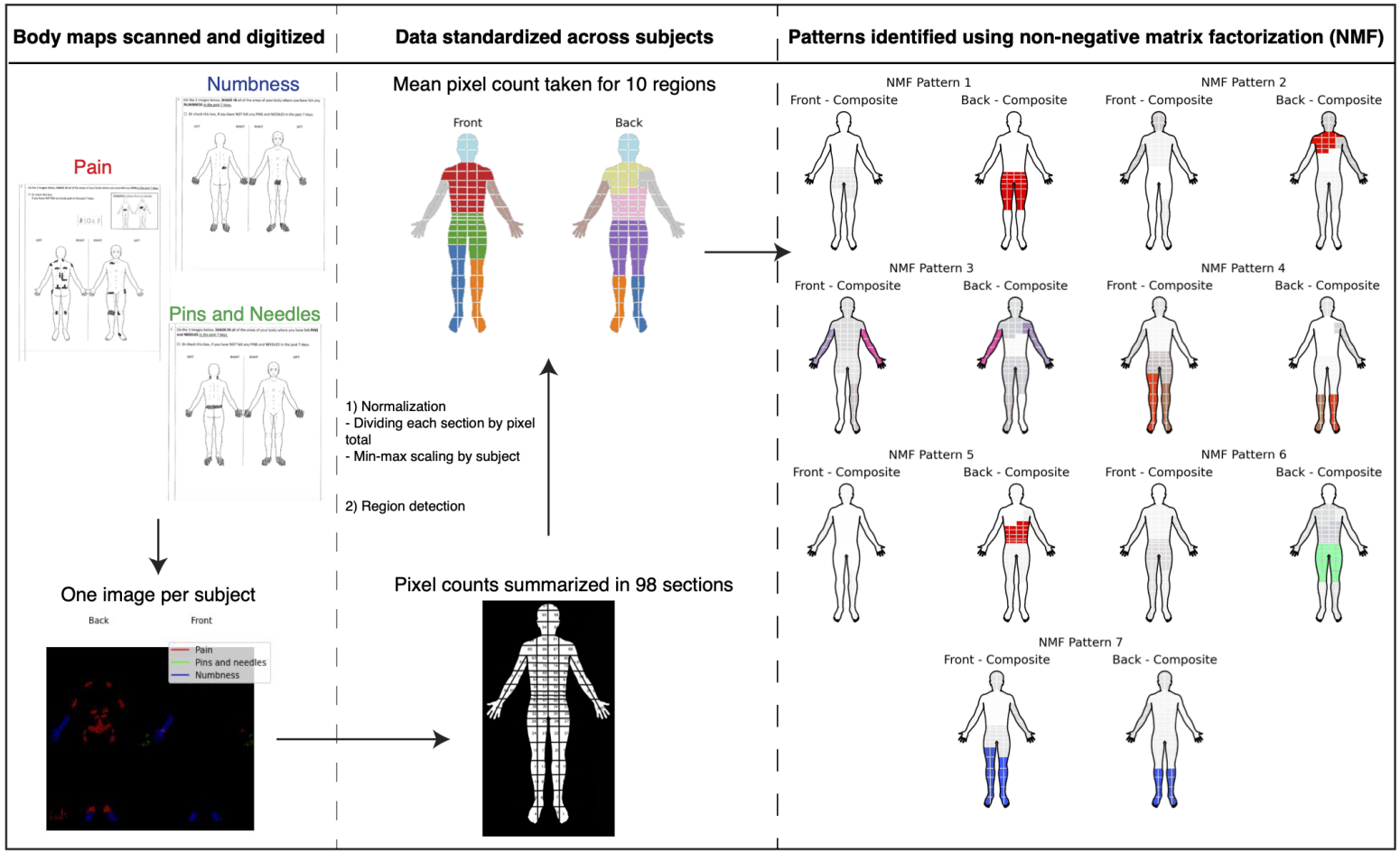

Figure 6.1 Body maps processing pipeline.

6.2.4 MRI data acquisition

Neuroimaging data were collected at four sites: University of California, San Francisco (UCSF), University of California, Davis (UCD), University of California, San Diego (UCSD), University of California, Irvine (UCI). All data were collected on 3T scanners from Siemens or GE. The protocol included structural T1-weighted scans and functional MRI with BOLD contrast with parameters as follows:

T1 structural scan: Repetition time (TR): 2500 ms (Siemens), 6 ms (GE); Echo time (TE): 3 ms; flip angle: 8; voxel size: $1 \times 1 \times 1$ mm.

BOLD fMRI: TR: 800 ms; TE: 30 ms; flip angle: 52; voxel size: 2.4 x 2.4 x 2.4 mm.

6.2.5 fMRI preprocessing

Neuroimaging data were preprocessed using *fMRIPrep* 20.2.7 [86, 87] and *Nilearn* [89]. A full fMRIPrep boilerplate file is provided in supplementary materials (Appendix B). Briefly, skull-stripped T1-weighted (T1w) MP-RAGE images were used for brain tissue segmentation and registration into standard MNI space. For BOLD data, susceptibility distortion correction was applied using fMRIPrep's fieldmap-less approach. The BOLD reference was co-registered to the T1w reference using boundary-based registration with 9 degrees of freedom. Head motion parameters were estimated before spatiotemporal filtering. BOLD runs were slice-time corrected and resampled into their original space and standard spaces (MNI152NLin2009cAsym, MNI152NLin6Asym). Several confounding time-series were calculated, including framewise displacement, DVARS, and global signals.

Further denoising and time series extraction was performed using the *NiftiLabelsMasker*

class in Nilearn. This included spatial smoothing (5-mm FWHM Gaussian kernel), temporal bandpass filtering (high pass = discrete cosines transformation, low pass = 0.08 Hz), nuisance signal regression (24 motion parameters, 2 white matter/CSF parameters), and scrubbing with a framewise displacement threshold of 0.5 mm. Subjects with less than 5 minutes of data retained after motion scrubbing were excluded from analysis. The Brainnetome atlas[178] was applied to extract mean BOLD time signals from 246 anatomically and functionally defined regions. Pearson's correlation was applied to each subject's time series to obtain a 246 x 246 functional correlation matrix ("functional connectome"/ FC). Each subject's FC was standardized using Fishers r-to-z transform.

6.2.6 Functional Connectivity Feature Selection

Feature selection was performed to identify a subset of the 30135 unique FC edges to use in CCA analysis using a resampled feature selection following Buch et al., 2023[173]. Over 100 iterations, Spearman's rank correlation coefficient was calculated between each FC edge and each body map pattern, and edges were ranked by the number of times they were found statistically correlated ($p < 0.001$) with at least one body map pattern.

6.2.7 Regularized CCA

Regularized CCA (RCCA) was performed between the body map patterns (Y) and FC features (X) using the python package *pyrcca* [179]. Parameter optimization was conducted through a repeated grid search over three variables: the regularization parameter λ, the number of canonical components (N_{CC}), and the number of FC features (N_{FC}). For each grid search

iteration, 99% of the dataset was randomly selected to train pyrcca's *CCACrossValidate* object class, which performs K-fold cross-validation to optimize λ and N_{CC}. This was performed using a variable number of top-ranked FC features ranging from 100 to 400, selecting the hyperparameter triplet that maximized the mean correlation over all components.

The number of canonical components calculated in CCA may be less than or equal to the minimum number of features in the input matrices. Given a lack of *a priori* knowledge regarding the optimal number of latent brain-body dimensions, an initial course grid search was performed to optimize the number of canonical components used in the model. Over 100 iterations, the grid search procedure described above was performed using 10-fold cross-validation with a hold-out size of 20% and a parameter grid as follows: λ: [10^{-7} to 10^{4}, 20 logarithmically spaced values], N_{CC}: [1 to 7 (the number of body map patterns)], N_{FC}: [100 to 400, step size of 20]. The most frequently occurring number of components over all grid search iterations was selected for the final model.

A bootstrapped permutation test was then performed to evaluate reproducibility in held-out data and to establish significance of the resulting canonical components (brain-body dimensions). Over 1000 iterations, data were randomly split into a training set and test set (test set size = 1%, 28 subjects). Grid search with 10-fold cross-validation was performed on the training set to optimize λ and N_{FC} while restricting N_{CC} to the optimal number obtained previously, with a refined parameter grid of λ: [10^{-8} to 10^{3}, 30 linearly spaced values] and N_{FC}: [180 to 400, step size of 20]. An RCCA model was then trained on the whole training set using the optimized parameters, and the held-out test set was projected into the trained RCCA space using pyrcca's *validate()* method. These steps were then repeated with the rows of Y randomly permuted to establish a null distribution, yielding a set of 1000 canonical

correlations for both the true and null test datasets. These distributions were compared using Welch's t-test testing the one-sided alternative hypothesis that null set correlations are greater.

Finally, RCCA was performed on the entire dataset. Parameter optimization was performed with 30-fold cross-validation using the same parameter grid, and a final RCCA model was trained using these optimized parameters, yielding a "brain-dimension" and "body-dimension" score for each subject and component. Spearman's correlation was calculated between each FC feature and each brain dimension score, as well as between each body part-sensation value and each body dimension score. Significant correlations following Bonferroni correction are presented for each component ($p_{brain} = 0.00014$, $p_{body} = 0.0016$).

6.2.8 Association with demographic, clinical, and psychosocial risk factors

Analysis was performed to investigate any associations between the final canonical components and common LBP risk factors. These were categorized by domain: demographic (biological sex, BMI, age), clinical (presence of imaging findings, score on Pain, Enjoyment and General Activity (PEG) scale, a 1-10 pain scale, mechanistic pain category), and psychosocial (Patient-Reported Outcomes Measurement Information System (PROMIS) measurements). A single score was obtained for each subject and component by projecting the subject's location in each component space to the y = x line. Correlation was then calculated between each component score and each variable of interest. Spearman Correlation was used for continuous variables (scatter plots), Mann-Whitney U test was used for binary categorical variables, and

Kruskal-Wallis test was used for categorical variables with more than 2 groups. Results are shown in Supplementary materials ((Appendix B).

6.2.9 Details of novel data set

Resting state data and pain body maps were provided for four novel subjects collected as part of a research trial of deep brain stimulation for refractory chronic neuropathic pain. Patient demographics and body map acquisition protocols have been previously described [180]. Briefly, participants completed digital body maps indicating pain location and intensity multiple times a day over a ten-day inpatient hospital stay. Data used in this analysis were collected at baseline.

Profiles of each of the four participants included in this study are provided below:

- RCS02: 58 yo F with history of R insular stroke with post stroke pain syndrome
- RCS04: 54 yo F with spinal DJD and chemotherapy induced neuropathy in feet and ankles
- RCS06: 49 yo M with cervical spine stenosis and spinal cord injury at T4
- RCS07: 51 yo F with pontine hemorrhage and one a half syndrome

Functional connectomes were derived for each novel subject using the same brain atlas and neuroimaging processing protocol described above. Predicted body map features were then computed as the dot product between the inverse of the body map weights and the

weighted novel functional data:

$$B_{novel} = b^{-1} \cdot (a' F_{novel}) \tag{6.2}$$

where a and b are the canonical weight vectors for the brain and body axes, respectively.

Model accuracy was assessed using binarized pain values for each body part. The presence or absence of pain was visually evaluated for each of the ten body parts per subject in the true data. These values were compared against binarized predicted body maps to generate an accuracy score per subject, i.e. the ratio of body parts with matching labels in true and predicted data.

6.3 Results

We performed rCCA to identify dimensions of common variation between resting state brain connectivity and whole body somatosensory patterns identified from patient-reported body maps. Parameter optimization was performed using k-fold cross-validation, yielding a final solution of 7 canonical components, which we refer to as "brain-body dimensions". All 7 dimensions were found significant in held-out validation sets using bootstrapped permutation testing (Supplementary Figure B.1). Model weights were then used to predict pain maps for a set of previously unseen subjects, suggesting an ability to identify the spatial distribution of chronic pain symptoms from brain activity recorded at rest.

6.3.1 A subset of brain networks predicts somatosensory symptoms

A subset of resting state functional connectivity features were selected as input to the rCCA model. Over 100 iterations, FC edges were ranked by the number of times they were significantly correlated with at least one body map feature. The number of top-ranked FC features was then optimized using 30-fold cross validation. A set of 350 FC features was selected, all of which are represented in Figure 6.2. Each plot provides a different view into the neural correlates of pain and sensory abnormalities in this cohort. The chord plot (top left) shows that features largely involved connectivity between a subset of cortical and subcortical networks. Specifically, connections between the somatomotor and frontoparietal networks are common, as well as connections between subcortical regions and parts of the DMN and dorsal attention networks. The glass brain (top right) shows specific nodes corresponding to regions of the Brainnetome atlas. Node sizes correlate with degree, meaning that larger nodes are involved in more of the edges chosen by the model. Three nodes are especially highly represented, each involved in more than 5% of the 350 features. These are the left and right homologues of region A2 of the postcentral gyrus, corresponding to the primary somatosensory cortex (S1), as well as the left region A20cl of the inferior temporal lobe. Finally, the bar plot (bottom) shows the summed degree of all nodes within each anatomical region, colored by node network. Here we see that a majority of connections involve regions of the parietal lobe and the thalamus.

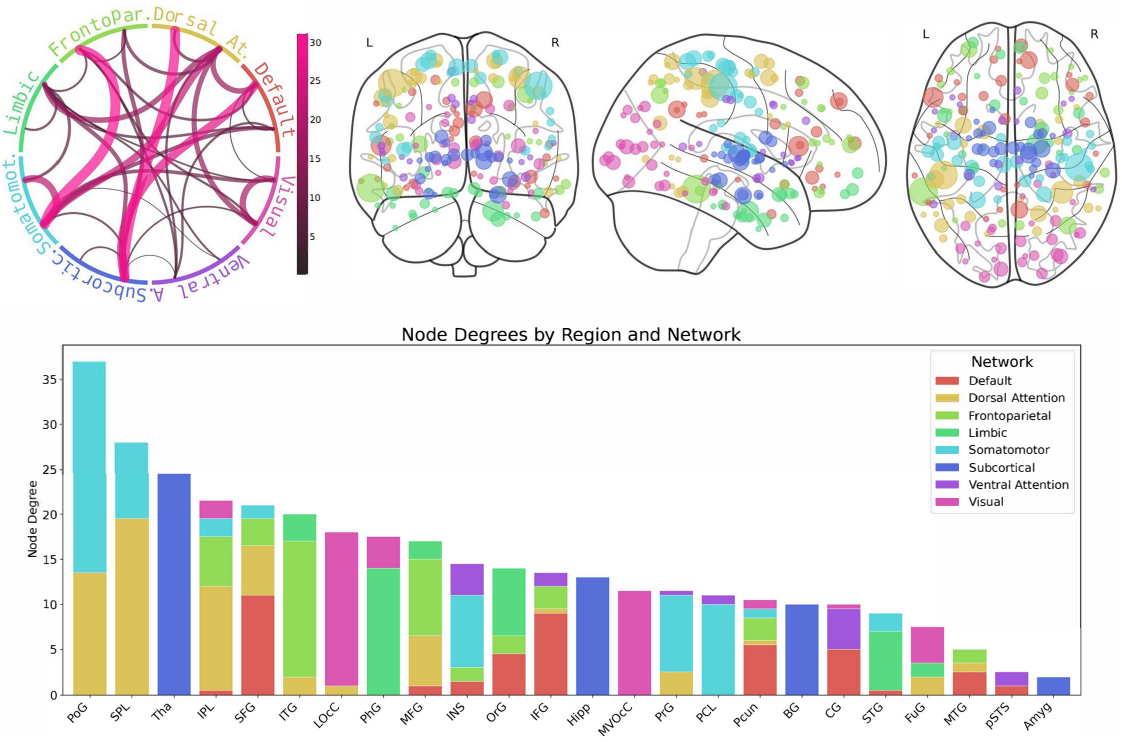

Figure 6.2 All 350 resting state FC features used in final model. Data are represented in three ways to aid in interpretation. Chord plot (upper left) shows network membership of all edges with line color and thickness indicating number of occurrences. Glass brain (upper right) shows anatomical locations of nodes, with nodes colored by network membership and sized by degree. Bar plot (bottom row) shows summed node degree by network and region in descending order. SFG: Superior Frontal Gyrus, MFG: Middle Frontal Gyrus, IFG: Inferior Frontal Gyrus, OrG: Orbital Gyrus, PrG: Precentral Gyrus, PCL: Paracentral Lobule, STG: Superior Temporal Gyrus, MTG: Middle Temporal Gyrus, ITG: Inferior Temporal Gyrus, FuG: Fusiform Gyrus, PhG: Parahippocampal Gyrus, pSTS: posterior Superior Temporal Sulcus, SPL: Superior Parietal Lobule, IPL: Inferior Parietal Lobule, Pcun: Precuneus, PoG: Postcentral Gyrus, INS: Insular Gyrus, CG: Cingulate Gyrus, MVOcC: MedioVentral Occipital Cortex, LOcC: Lateral Occipital Cortex, Amyg: Amygdala, Hipp: Hippocampus, BG: Basal Ganglia, Tha: Thalamus.

6.3.2 Brain-body dimensions resemble mechanistic pain categories

Each of the 7 components identified through rCCA represents a "brain-body dimension" in which somatosensory patterns are linearly correlated with resting state connectivity patterns. All components were strongly correlated (p range 0.77-0.83) and significant in held-out test sets compared to shuffled data (see supplementary figures). A figure showing the brain

and body features associated with each component is shown in the supplmentary materials ((Appendix B). Here, we focus our analysis on the first two components based on their distinctive alignment with previous literature. Specifically, we found that the body map patterns associated with these components showed remarkable correspondence with the established mechanism-based categories of persistent pain, providing novel insight into the neurobiological signatures of nociceptive pain, neuropathic, and nociplastic pain.

When interpreting these dimensions, it is crucial to note that a negative correlation does not imply an absence of a feature but rather a stronger association with the negatively correlated feature. Thus, we choose to discuss these dimensions in terms of spectra with distinct phenotypes at either end (A and B) representative of the negative and positive weights, respectively.

6.3.2.1 Nociplastic spectrum

The first brain-body dimension represents widespread bodily symptoms. Phenotype 1A is associated with more pain, numbness, and pins and needles throughout all regions of the body. This phenotype is also associated with weaker connectivity within and between several brain networks. This largely involves the left and right S1 region of the postcentral gyrus. These results suggest that widespread bodily symptoms are associated with weaker connectivity between S1 and other regions associated with somatomotor and attention networks. It is also correlated with weaker connectivity within the visual network, specifically the occipital cortex and fusiform gyrus, and within subcortical and limbic regions such as the parahippocampal gyrus, hippocampus and basal ganglia.

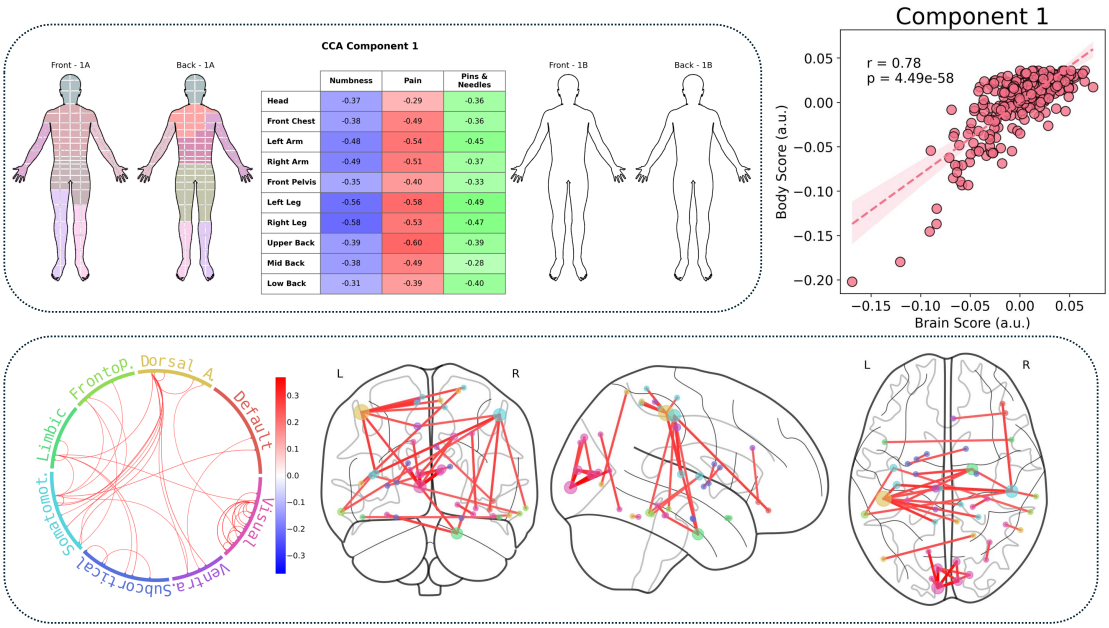

Figure 6.3 Canonical Component 1: The Nociplastic Dimension.

6.3.2.2 Nociceptive-neuropathic spectrum

The second dimension represents a gradient from back pain on one end to numbness in the low back and limbs on the other. Phenotype 2B, the numbness phenotype, is associated with stronger connectivity between subcortical regions, specifically the thalamus and basal ganglia, and parts of the DMN, dorsal attention, and frontoparietal networks, while the converse is true for Phenotype 2A, the axial low back pain phenotype. This dimension is also associated with connectivity between the somatomotor and visual networks. Specifically, Phenotype 2B exhibits stronger connectivity between the primary somatosensory/motor cortices and regions of the right lateral occipital lobe.

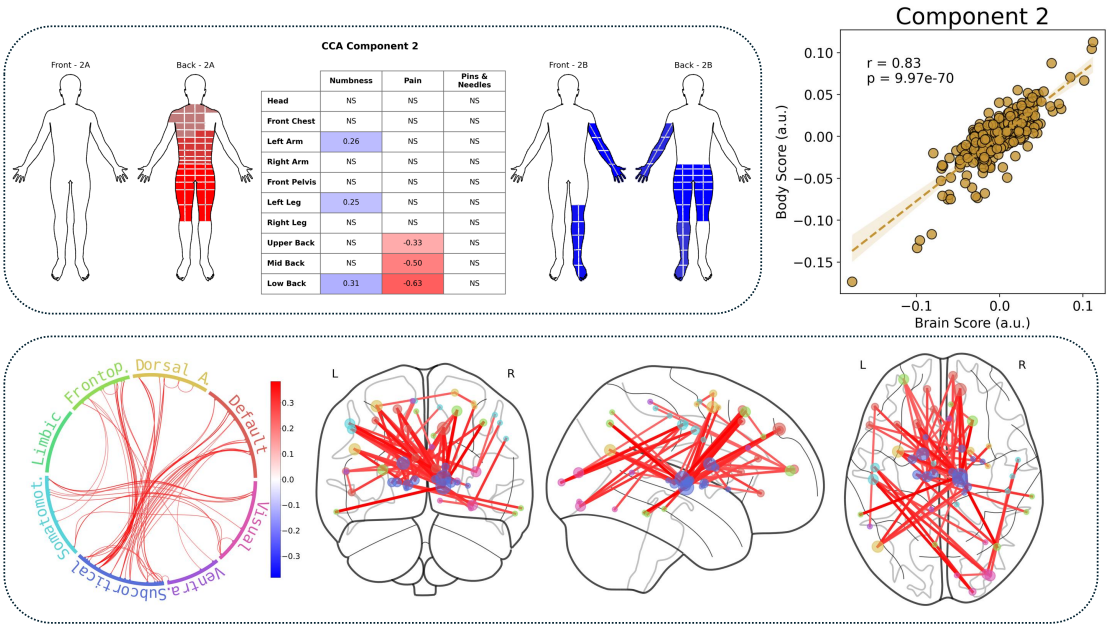

Figure 6.4 Canonical Component 2: Nociceptive-Neuropathic Dimension.

6.3.3 Model predicts spatial pain distribution in novel dataset

To test the generality of our model, we investigated whether it could predict body maps from resting state data in an unseen dataset. Body maps were predicted for four novel subjects by projecting each subject's resting state data into trained CCA space following the predictive framework outlined by Bilenko and Gallant[179]. In other words, an estimate for each body part and sensation was computed for each subject as a linear combination of his or her functional connectivity features and canonical weights calculated on our LBP cohort. Results of this test are shown in Figure 6.5. Visual inspection of these results indicates moderate correlation between predicted and true values, while a preliminary quantitative analysis suggests moderate predictive performance (accuracy score range 0.5-0.9).

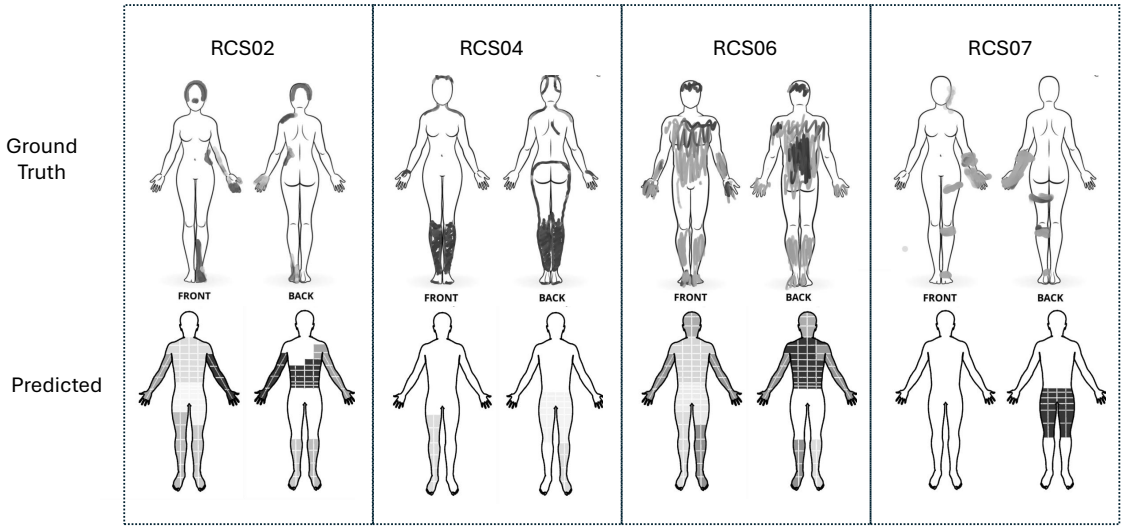

Figure 6.5 Body map predictions on novel dataset. Upper row is ground truth, lower row is predicted. All images are shown in grayscale to enable interpretation.

6.4 Discussion

With this study, we sought to identify neurobiological signatures underlying different phenotypes in our chronic LBP cohort. Our cross-decomposition analysis yielded seven brain-body dimensions, each representing a novel spectrum of somatosensory patterns correlated with resting-state functional connectivity. These dimensions form a low-dimensional space capable of predicting pain body maps in a previously unseen dataset, suggesting that these relationships extend beyond cLBP to chronic pain conditions more broadly.

Our model identified a subset of resting state functional connectivity features associated with somatosensory patterns. This involved many brain areas traditionally associated with nociceptive processing, including S1, thalamus, and frontal regions, as well as some less expected regions, such as the inferior temporal gyrus and lateral occipital cortex. The wide range of regions and networks in our predictive set is consistent with previous reports

associating chronic low back pain with global brain network reorganization [73].

Our multivariate approach represents a departure from the discrete categorization normally employed in studies of chronic pain. Rather than identifying subjects as belonging to a specific pain type, we show that patients can be distributed along a set of spectra. We also want to highlight the relative simplicity of this model. The continuous linear distributions shown for each dimension indicate not just that brain and body patterns are associated but that they are directly linearly correlated, suggesting that an incremental change in one set of features may predict change in another.

Our first dimension shows an association between widespread bodily symptoms and weaker connectivity between a network of brain regions with hubs in bilateral S1. This phenotype is also associated with cognitive dysfunction, specifically elevated anxiety and fatigue and diminished social functioning. This aligns with the emerging definition of nociplastic pain and provides a novel view into the related neurobiological mechanisms. S1 abnormalities, such as increased inflammatory activation, are increasingly recognized as a potential biomarker of nociplastic pain [181]. The involvement of occipital lobe interconnectivity is less expected. However, we are not the first to note visual network abnormalities in chronic pain subjects [182]. We hypothesize that this may be indicative of widespread sensory circuit reorganization.

We refer to our second dimension as a nociceptive-neuropathic spectrum. We show that the amount of self-reported numbness in the back and legs (characteristic of neuropathic phenotypes) is associated with stronger connectivity between the thalamus and various regions of the cortex associated with attention and higher cognitive functions, as well as between somatomotor regions and parts of the occipital cortex. The strong association with thalamic connectivity is consistent with previous literature suggesting altered thalamocortical activity

as a signature of neuropathic pain [64, 166]. Additionally, higher levels of cortical disinhibition have been shown in neuropathic pain patients compared to nociceptive patients [183]. It is possible that the somatomotor-visual connectivity seen in our neuropathic phenotype represents an extension of this effect observable at rest.

Perhaps the most compelling aspect of our findings is the ability to predict pain body maps in an independent dataset. Despite the numerous potential sources of variation in the novel data, including out-of-distribution subjects and differences in data acquisition and processing protocols, our model demonstrated moderate ability to predict spatial locations and intensity of pain from resting state fMRI data. This is especially noteworthy given the relative simplicity of our model, employing only a weighted linear combination of a relatively small subset of brain connectivity features. While we recognize the limitations of this very small and largely qualitative example, we intend to further explore this prospect in future work.

Our work has several important limitations. Primarily, we want to acknowledge the exploratory nature of this study; CCA analysis can only show correlations but does not provide any insight into causal links between our datasets, precluding any direct clinical utility. Additionally, our findings are restricted to individuals with cLBP who already exhibit altered neurocircuitry; this model is unlikely to generalize to healthy controls and may not even extend to other chronic pain conditions, although our preliminary results suggest a degree of universality. Methodologically, the subjective nature of body map reporting presents challenges in standardization and processing that could influence our results. Furthermore, we did not exclude participants based on medication use aside from opioids, which may confound the observed brain-body relationships.

Despite these limitations, the strong correlations and significance observed in our model suggests that it does capture meaningful associations between somatosensory abnormalities and brain connectivity in our cLBP cohort. These findings present resting state functional connectivity as a potential avenue for deriving pain biomarkers. Additionally, the resemblance of our components to documented chronic pain phenotypes further supports the utility of our approach for uncovering latent neurobiological signatures in the chronic pain population that may be leveraged to provide more targeted pain treatments.

Chapter 7

Leveraging the connectome model to investigate temporal and spatial dimensions of knee cartilage thickness change as they relate to osteoarthritis

The following manuscript is reformatted and reproduced with full permission from the publisher. It appeared as:

Cummings, J., Gao, K., Chen, V., Morales Martinez, A., Iriondo, C., Caliva, F., Majumdar, S. and Pedoia, V., 2024. The knee connectome: A novel tool for studying spatiotemporal change in cartilage thickness. Journal of Orthopaedic Research, 42(1), pp.43-53.

7.1 Introduction

Osteoarthritis (OA) is a common joint disease characterized by pain and decreased range of motion. OA is one of the most prevalent causes of global disability and is likely to grow more pervasive with increasing life expectancy and obesity rates [184]. The knee is the most afflicted joint, with knee OA accounting for about 85% of global OA burden [40].

While growing evidence suggests that OA involves a complex pathogenesis of structural changes to the cartilage, bone, ligaments, and muscles [185, 186], articular cartilage changes are the most studied feature of OA progression [187, 188]. Early stages of OA are characterized by cartilage changes including increased hydration, proteoglycan loss, and disruption of collagen fibers, while later changes include dehydration and thinning of the cartilage, resulting in denudation of the underlying bone [51].

Cartilage thickness and volume changes measured with Magnetic Resonance Imaging (MRI) have proven useful in predicting OA progression [189, 190]. However, the exact nature of this relationship remains to be characterized. Studies have shown both cartilage thickening and thinning at different rates and locations of the knee in healthy and diseased subjects [45, 46, 47, 48]. Given the complexity and long timescale of OA progression, it is likely that differences in the length of time between thickness measurements and in disease states between patient groups account for some of these discrepancies. Knees at earlier stages of the disease have shown cartilage thickening and thinning in the medial femorotibial compartment with similar proportions, while later stages are more associated with thinning. This is consistent with animal studies showing that early OA cartilage may appear to thicken as a result of hypertrophy or swelling [45, 49, 50]. Cartilage changes have also been shown

following anterior cruciate ligament (ACL) injury, a substantial risk factor for developing OA. Overall femorotibial cartilage thickness was found to increase in the 5 years following injury, particularly in the medial femorotibial compartment, but subregional thinning and thickening was observed within the same cartilage plate [191]. A recent study attempted to capture the longitudinal dynamics of cartilage thickness by quantitatively assessing the cartilage thickness trajectories of several knee compartments at 7 timepoints over the course of 8 years [192]. These results indicated that knees with nonstable trajectories, including both net thickening and net thinning, had higher adjusted odds of OA incidence than stable trajectories.

While most studies of knee cartilage thickness have obtained just a few data points from the entire cartilage plate of a bone, usually by measuring at select locations or averaging over a large portion of the surface, growing evidence suggests that spatially localized cartilage thickness changes hold clinical relevance. Cartilage thickness has been shown to vary on the scale of millimeters within the medial and lateral weight-bearing regions of the femur in healthy knees [193]. Another study of healthy subjects reported that the most distal points of femoral condylar cartilage, which engage the tibia most during extension, are thinner than the most posterior points, which engage the tibia during flexion, and that the posterior-medial cartilage is thicker than lateral [194]. Furthermore, evidence suggests that spatial distributions of cartilage thickness grow increasingly variable during OA progression. One study of female subjects demonstrated the most thickening in the peripheral subregions of the central medial femur at early stages of the disease, while knees at later stages showed pronounced thinning throughout the central medial femur [195]. Another study associated late-stage OA with thinner cartilage in anterior parts of the medial femoral condyle and

thicker cartilage in the posterior condyle [196, 197]. It is likely that spatial variation in cartilage thickness has previously been obscured by the practice of averaging over large areas of cartilage without accounting for spatial differences in geometry and function [195].

The objective of this study was to better understand both the temporal and spatial dimensions of knee cartilage thickness change as they relate to osteoarthritis protection and risk factors. Leveraging recent advancements in deep learning, we employed automatic segmentation methods to obtain cartilage thickness measurements from a spatially dense point cloud representation of the femur cartilage for 1418 knees at seven time points over the course of 8 years. We then made use of an analysis method traditionally employed in functional neuroimaging studies, the connectivity matrix, or "connectome", to explore the statistical relationships between cartilage thickness trajectories at each subregion. With this tool, we aimed to elucidate patterns of functional connectivity in the knee joint that may serve as biomarkers of healthy or pathological knee aging.

7.2 Methods

7.2.1 Study Population and Data Selection

The Osteoarthritis Initiative (OAI) data set was used for this study. This is a multi-center prospective longitudinal study [198]. The study enrolled 4,796 participants with or at risk of OA in the United States between February 2004 and May 2006. OAI subjects were monitored across 12 time points, from an initial baseline visit to a final 108 month visit [198]. Out of these 12 time points, MRI scans were performed at seven time points [0,12,24,36,48,72,96] months,

resulting in an imaging span of eight years 0-96 months. Demographic data such as age, body mass index (BMI), and sex were also recorded during each visit. Kellgren-Lawrence (KL) grading was performed by trained musculoskeletal radiologists on radiographs of both knees at the enrollment visit, 12-month, 24-month, 36-month, and 48-month for all the participants in the OAI. KL grading depicts structural abnormalities and is the accepted standard for OA diagnosis as well as the most widely used structural outcome in epidemiological studies and clinical trials [199]. OAI MRI imaging protocol includes a 3D double-echo steady-state (3D-DESS,3T Siemens) which is the only sequence used for cartilage thickness biomarker extraction. MRI parameters included: TR/TE 16.2/4.7; FOV, 14 cm; matrix, 307x384; bandwidth, 71 kHz; and image resolution, [0.365, 0.456, 0.7] mm).

From the total of 9,592 3D-DESS knee MRIs acquired from bilateral examination of 4,796 participants at the baseline time point, we selected knees that did not have a diagnosis of radiographic OA at baseline (KL grade < 2) and for which data was available for all follow-up visits. With these inclusion/exclusion criteria we obtained a data set of 1418 knees (1035 unique subjects). On the total of 1418 knees included in this study, 232 (16%; at least one knee from 218 unique subjects) had incident radiographic OA (KL grade > 1) over the course of the study, resulting in a control group of 1186 knees and an OA incidence group of 232. Demographics at baseline for the control and OA incidence groups are shown in Table 7.1.

Table 7.1 Demographics of Control and OA Incidence subject group. Demographics of Control and OA Incidence subject groups. Continuous variables (age, bmi) shown as mean (standard deviation). Categorical variables (sex, knee alignment) shown as raw count (% of total). Varus and valgus data (italicized) calculated on a subset of knees (454 in Control Group, 229 in OA Incidence Group). $^{*}p < .05$ and $^{**}p < 0.001$

	Control (n = 1186)	OA Incidence (n = 232)
Sex = Female	**641 (54%)**	**163 (70%) ****
Age [years]	58.7 (8.5)	59.6 (8.7)
BMI [kg/m^2]	**27.1 (4.2)**	**28.7 (4.3) ****
Varus Alignment	***143 (31.5%)***	***57 (24.9%) ****
Valgus Alignment	***8 (1.8%)***	***10 (4.4%) ****

7.2.2 Knee Alignment Classification

Femur–tibia angle (FTA) data at baseline were available for a subset of the knees in the study (n = 683, 45.9% of all knees in study), consisting of 454 knees that did not develop OA and 229 knees that did. These data were used to classify the subset into varus, neutral, and valgus alignment groups. FTA data were first translated to hip-knee-ankle (HKA) angle equivalent using a previously proposed formula[200]: $HKA_{eq} = FTA * 0.98 + 4.0$. The following thresholds were then used to define groups: Varus = $HKA_{eq}leq - 2degree$; Neutral = $-2degree < HKA_{eq} < 2degree$; Valgus = $HKA_{eq}geq2degree$. Varus and valgus alignment for knees within each subset of the control and OA incidence groups are shown in Figure 7.1.

7.2.3 Image Processing

A bone and a cartilage segmentation model ensemble based on multiple 2D and 3D V-nets were trained on 72 and 148 manually annotated 3D-DESS volumes to automatically segment the femur, tibia, and patella bones and corresponding cartilage. The two models were extensively validated and tested obtaining Dice Score Coefficient (DSC) equal to 98.0% ± 0.32%, 98.0% ± 0.26%, and 96.4% ± 0.70% for the femur, tibia, and patella bone respectively. The cartilage segmentation test dice scores were 90.0% ± 0.74%, 88.6% ± 1.3%, and 85.7% ± 2.5% for the femoral, tibial, and patellar cartilage respectively. Implementation details and evaluation strategies are reported in previously published work [192, 201, 202] and summarized in Figure 7.1. The trained models were used in inference to segment all the 3D-DESS volumes available in OAI (45,789); cartilage thickness maps were obtained from the segmented masks using a distance transform method previously proposed [192]. Automatic evaluation results were compared with the ones performed manually, which are publicly available on the OAI website (N=4,299). We observed strong correlations and mean absolute errors within the voxel resolution. Pearson r values ranged between 0.850 in central Lateral Femur and 0.955 in Lateral Tibia; average absolute difference ranged between 0.108 mm in Medial Tibia and 0.143 mm in central Lateral Femur.

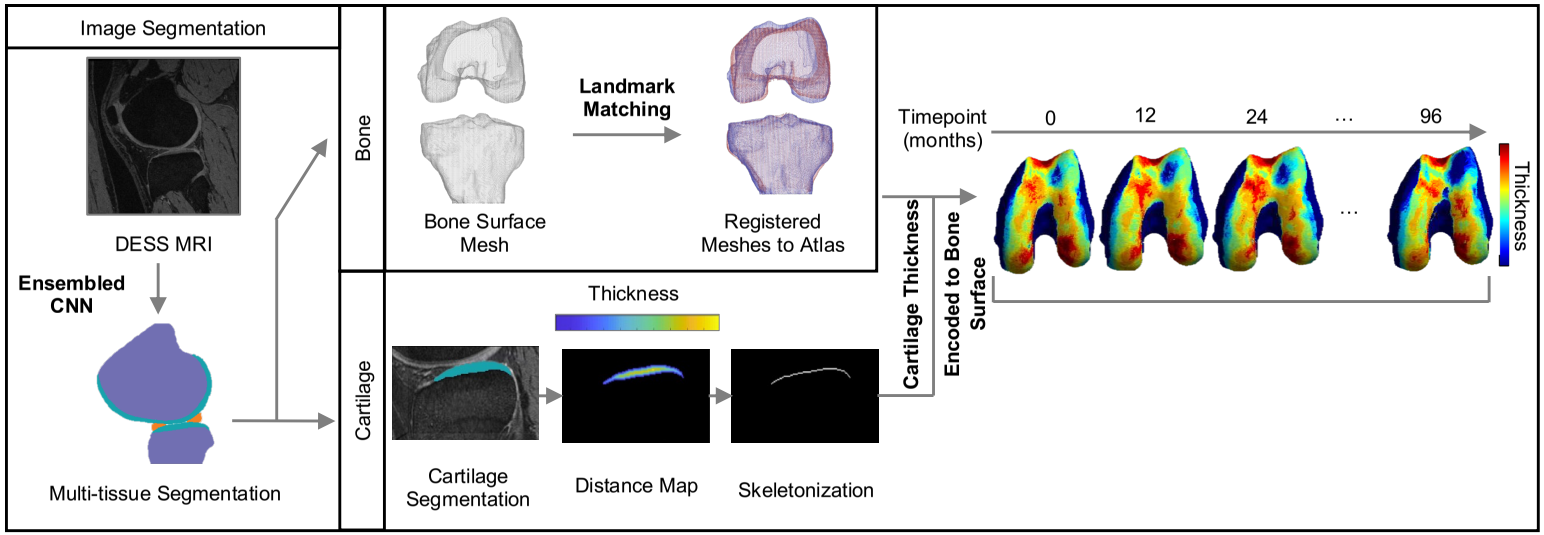

Figure 7.1 Overview of image processing pipeline. A segmentation model ensemble was used to automatically segment bone and cartilage in sagittal slices of knee MRI volumes. Bone meshes were registered to a reference bone surface. Per sagittal slice, a Euclidean distance transform and skeletonization was performed on cartilage segmentations. The distance map was projected to the underlying bone mesh to obtain a dense cartilage thickness map for each knee volume at each time point. Implementation details can be found in Iriondo et al., 2020 [192].

A normal vector spanning from each point in the bone surface was used to sample the overlying cartilage thickness by averaging the thickness values at all skeleton points within a radius of 0.729 mm, empirically set to double the in-plane pixel resolution. With this procedure we obtained dense thickness maps for each knee and each time point encoded in a triangulated mesh of a variable number of vertices spanning between 46816-124422. All meshes were than registered to a single atlas bone surface selected to match the average demographic distribution of the used data set. The landmark matching strategy used in this study was based on the one proposed by Lombaert, H. et al [203]. The maximum and minimum local curvatures were used for coupling homologous points on two surfaces. Both these features were locally defined on the surfaces and used to identify the landmark matching solved using Coherent Point Drift [204].

7.2.4 Knee Connectome

We created a parcellation of the femur cartilage by dividing the cartilage mask into two equally spaced sections along the medial-lateral axis and three equally spaced sections along the anterior-posterior axis, with the middle third labeled as the weight-bearing section. The medial and lateral sides were further divided along the medial-lateral axis into five subsections each. Three of these subsections fell out of the cartilage mask due to the curvature of the bone, including the outermost subregions of the anterior medial and anterior lateral compartments and the most central subregion of the posterior medial compartment, resulting in 27 subregions total (4-5 subregions per compartment). The resulting atlas is shown in Figure 7.2. Cartilage thickness trajectories were calculated for each subject for each of the

27 subregions by averaging the thickness measurements at all vertices within each subregion at each time point.

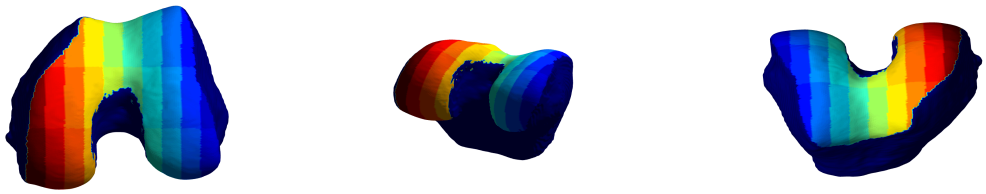

(a) Central View **(b)** Posterier View **(c)** Anterior View

Figure 7.2 Cartilage Parcellation Atlas. An atlas was created by dividing the three-dimensional reference cartilage mask into 27 subregions (4-5 subregions per compartment), each represented by a different color.

Pearson correlation coefficient r was used to represent the similarity between each pairwise combination of 27 time series, resulting in a correlation matrix, or connectome, with 729 entries for each subject. The connectome generation process is represented in Figure 3. We consider the r value a representation of functional connectivity between a pair of subregions and thus refer to each entry of the connectome as a "connection". Group average connectomes were obtained by averaging across connectomes of all subjects within a given group, meaning that each entry in the average matrix is an average of r values at that entry across all group members (e.g., 1186 knees in the average healthy control group). As the connectome is a symmetric matrix, only the lower triangle was considered in analysis and is shown in figures.

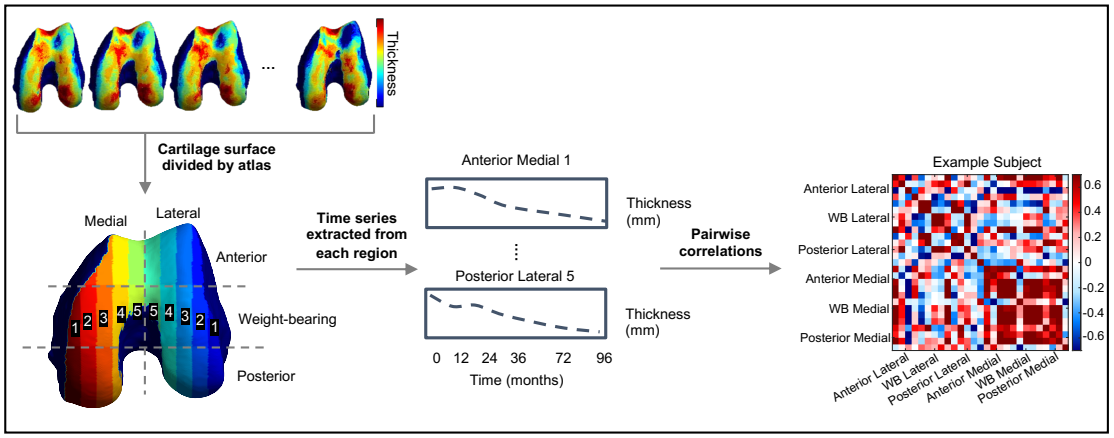

Figure 7.3 Schematic of connectome generation. Cartilage thickness values at all vertices within each subregion of the cartilage atlas were averaged to obtain a single value per subregion. This was performed at all time points to obtain cartilage thickness trajectories for all subregions. Pearson correlation coefficient r was used to represent the similarity between each pairwise combination of time series, resulting in a symmetric correlation matrix (connectome) for each knee. Each row/column entry in the connectome represents the correlation between the thickness trajectories of a pair of the 27 subregions. Every labeled compartment in the connectome contains 4-5 subregions.

7.2.5 Statistical Analysis

The aim of our analysis was to investigate whether the connectome would reveal spatiotemporal patterns of cartilage thickness change that are associated with OA protection or risk factors. We first sought to identify consistent patterns in the cohort of subjects that did not develop OA over the course of the study. We averaged connectomes across all healthy knees to obtain group-level descriptive statistics. We then separated connectomes from healthy knees into groups defined by sex and BMI and used the two-sample t-test to evaluate differences between these groups. A BMI $\geq$ 30 was considered high when dividing control subjects into high and low BMI groups for comparison. Finally, we compared the connectomes of knees that remained control throughout the study with those that developed OA. Partial correlation was used to control for demographic differences including sex, BMI, and knee angle when

comparing control and OA incidence groups within the subset of knees for which knee angle data were available. Where applicable, mean r scores are reported as [Mean Positive R; Mean Negative R], indicating that means were obtained over positive correlations and negative correlations separately. Bonferroni correction was applied to control for multiple comparisons, resulting in a p-value threshold of 1.42e-04.

7.3 Results

7.3.1 Features of Healthy Knee Connectome

As a first aim, we report the key descriptive features of the average connectome of the 1186 knees that did not develop OA during the 8 years of observation Figure 7.4. We consider the average control connectome a model for the spatial-temporal relationship of cartilage thickness longitudinal changes related to healthy aging.

The first feature of note is that intracorrelations, meaning the correlations between different subregions within a region, are stronger than intercorrelations, the correlations between subregions of different regions (Figure 7.4A). The mean r for positive and negative intracorrelations is [0.42; -0.17], while mean r for intercorrelations = [0.14; -0.07].

A second notable feature is that, within the weight-bearing and posterior intracorrelations, we observe weak to moderate negative correlations in addition to the more expected strong positive correlations (Figure 7.4B). Mean r for weight-bearing medial intracorrelations = [0.44; -0.17]; weight-bearing lateral intracorrelations = [0.45; -0.22]; posterior medial intracorrelatons = [0.27; -0.20]; posterior lateral intracorrelations = [0.38; -0.09]. While the average of negative

correlations is just moderate, this was observed to be a consistent pattern on the control connectome. This observation means that the cartilage thickness trajectory of different regions can diverge, but at a synchronous rate: while one region is thinning over time another appears to be thickening.

Third, we observe that associations between thickness trajectories in the anterior and weight-bearing regions tend to be stronger in the medial side than the lateral side: Medial anterior vs. weight-bearing intercorrelations = [0.30; -0.07]; Lateral anterior vs. weight-bearing intercorrelations = [0.17; -0.05] (Figure 7.4C). Finally, we show a consistent anticorrelation pattern between medial and lateral weight-bearing regions: Medial vs. lateral intercorrelations = [0.17; -0.10] (Figure 7.4D).

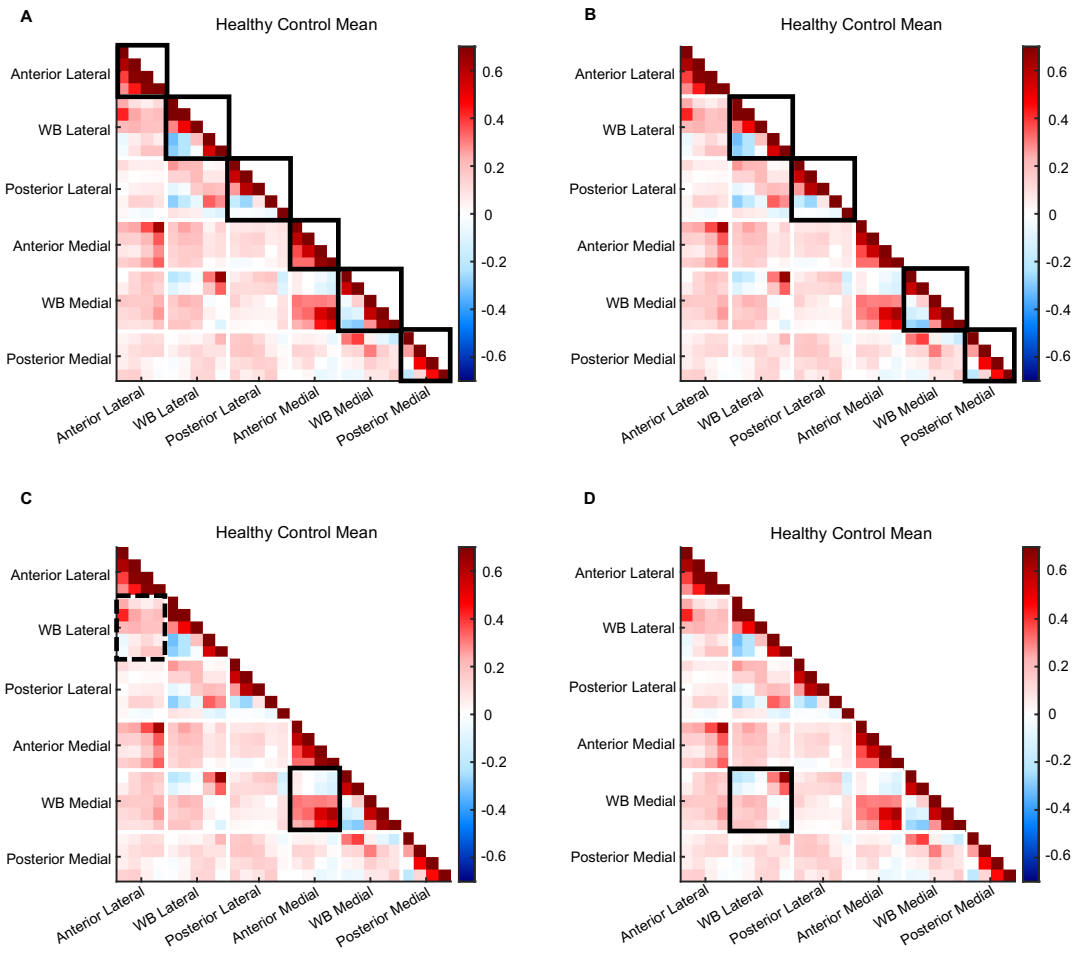

Figure 7.4 Illustration of key descriptive features of average control connectome. A) Intracorrelations (solid boxes) are generally stronger than intercorrelations (all else). B) Weight-bearing and posterior regions (solid boxes) have strong positives but also weak to moderate negatives. C) Associations between anterior and weight-bearing compartments are stronger in medial (solid) than lateral (dashed) sides. D) Consistent anticorrelation pattern observed between medial and lateral weight-bearing regions (solid box).

7.3.2 Population differences within control group

Comparing male and female subjects, we find 38 statistically significant connection differences (p values = 2.94e-11 - 1.22e-04) (Figure 7.5A-C). Of these, 55.3% involve the anterior medial region, with anterior medial intracorrelations comprising 15.8% of all significant connections, and 31.6% involve the anterior lateral region. Nearly all significant connections involving

the anterior medial and lateral regions have a positive mean for females, apart from one connection between the anterior medial region and weight-bearing medial region, which is weakly negative. 7 of these same connections have a negative mean in the male population: 2 between anterior lateral and weight-bearing lateral, 2 between anterior lateral and anterior medial, 1 between anterior medial and posterior lateral, 1 between anterior medial and weight-bearing lateral, and 1 between anterior medial and weight-bearing medial. This includes the one connection that is negative for females, for which the male mean is more strongly negative. 26.3% of the significant connections involve the weight-bearing medial region, and 39.5% involve weight-bearing lateral. 2 of the 3 significant weight-bearing lateral intracorrelations have a negative mean for both groups, while the other is positive for both. Connections involving posterior medial and lateral regions comprise 7.9% and 13.2%, respectively. 1 is a posterior lateral intracorrelation, which is weakly positive for both on average, but stronger for the female group. There are 2 significant connections for which females have a negative mean and males have a positive mean: 1 between weight-bearing medial and weight-bearing lateral, and 1 between posterior medial and weight-bearing lateral. Of all connections which are positive on average for both groups, 55.5% are more strongly positive for the female group. For all connections that have a negative mean for both, the male mean is more strongly negative.

Comparing the connectomes of the high and low BMI groups, we find two statistically significant differences (p values = 3.03e-05 - 5.22e-05) (Figure 7.5D-F). Both involve the weight-bearing lateral region. One is with the anterior medial region and has a positive mean for the low BMI group and negative for the high BMI group. The other is with the posterior medial region and is weakly negative on average for the low BMI group and positive for the

high BMI group.

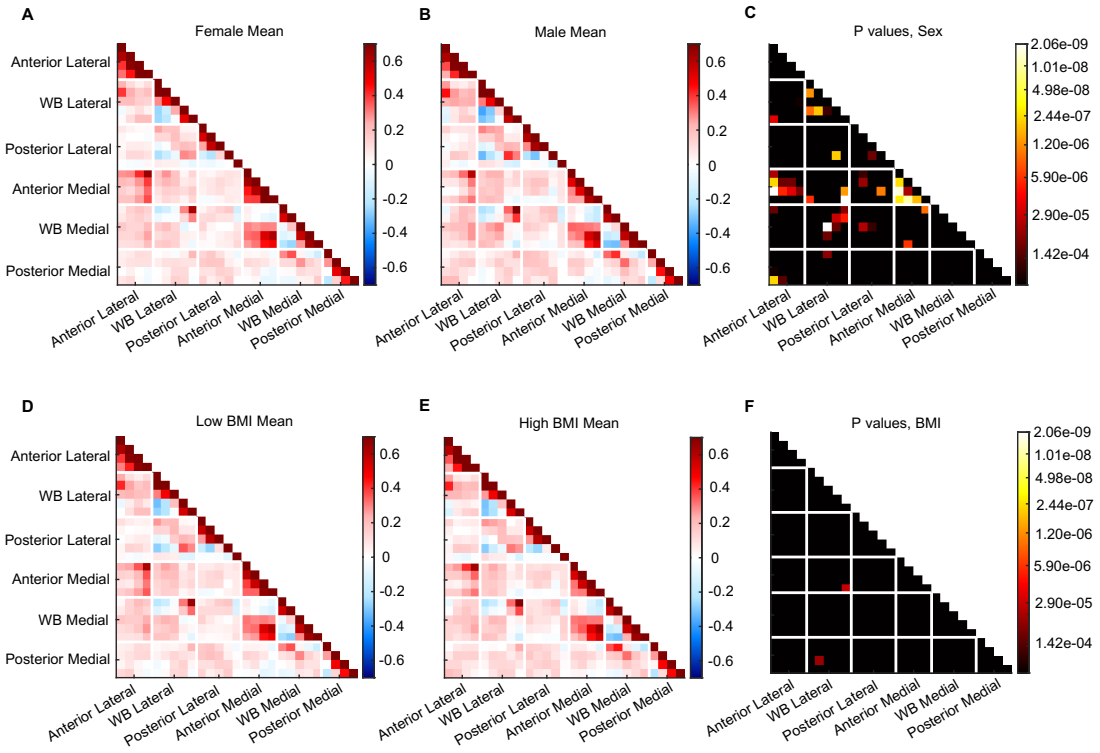

Figure 7.5 Population differences within control group. A) Mean connectome for female subjects. B) Mean connectome for male subjects. C) P-value matrix comparing male and female mean connectomes. D) Mean connectome for subjects with a BMI below 30. E) Mean connectome for subjects with BMI $\geq$ 30. F) P-value matrix comparing mean connectomes for high and low BMI subjects.

7.3.3 Control vs. OA Incidence Groups

When comparing the control and OA incidence groups, there are 20 significantly different functional connections (p values = 4.07e-14 - 1.35e-04) (Figure 7.6A-C). After controlling for confounding variables (sex, BMI, age, and knee alignment), there are six remaining statistically significant connections (p values = 5.02e-08 - 1.23e-04) (Figure 7.6D). 66.7% of these involve the weight-bearing medial region, with weight-bearing medial intracorrelations comprising 33.3% and the other half involving intercorrelations with the weight-bearing

lateral region. Of the two remaining significant connections, one is between weight-bearing lateral and anterior lateral regions, and the other is a posterior medial intracorrelation. 4 of the 6 connections have a positive mean for both groups, 3 of which are more strongly positive for the control group than the OA incidence group. One connection between the weight-bearing medial and weight-bearing lateral regions has a negative mean for the OA incidence group and positive for controls, while one weight-bearing medial intracorrelation has a negative mean for the control group and positive for the incidence group.

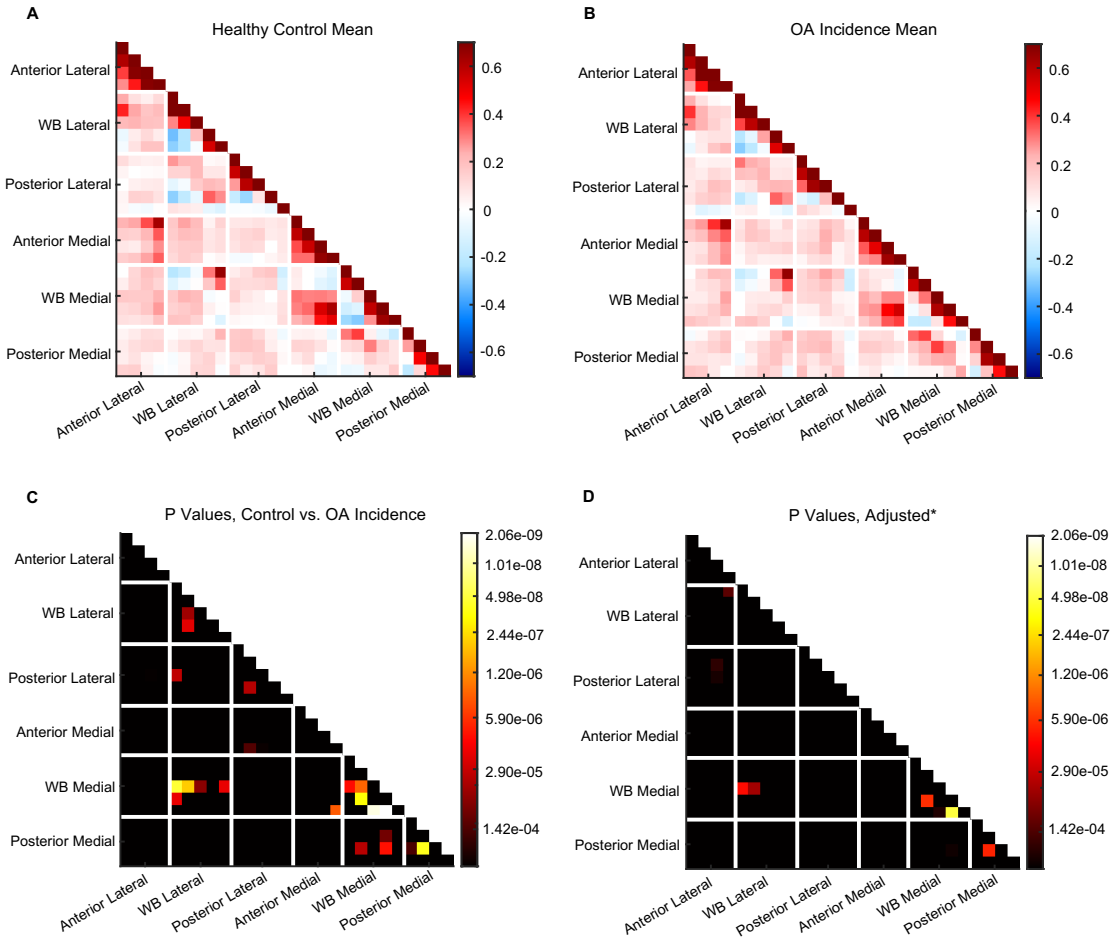

Figure 7.6 Comparison between control and OA incidence groups. A) Mean connectome for control group. B) Mean connectome for OA incidence group. C) P-value matrix comparing control and OA incidence groups. D) P-value matrix of partial correlation analysis comparing control and OA incidence groups while controlling for sex, BMI, and knee alignment.

7.4 Discussion

In this study, we present the first application, to our knowledge, of the connectome as a tool for studying longitudinal cartilage thickness changes in the knee.

Consistent correlation patterns are seen in the connectomes of healthy control subjects, which we present as potential biomarkers of healthy joint aging. We note that these features are evident when averaging across all 1186 healthy knees, supporting the consistency of these results. The trajectories of subregions within a given functional region are strongly correlated. This is an expected feature, as it is not surprising that adjacent subregions progress more synchronously than regions located in portions of the articular surface that might be loaded or engaged differently during movements such as knee flexion vs standing weight-bearing.

One notable aspect is the presence of negative correlations, meaning that one subregion must be thinning while another is thickening. While we are not the first to report the presence of both thickening and thinning within the same joint [45, 205], our findings add another dimension to this analysis, suggesting a functional relationship underlying these changes. Importantly, the use of correlation as our main metric provides a means of capturing temporal dynamics that have not previously been studied. When treating the trajectory of measurements as a raw time signal, we observe waveforms indicating fluctuations in cartilage thickness between each time point. The presence of negative correlations between these time series suggests that these fluctuations are not simply capturing intrinsic changes in the subject's state (e.g., differences in hydration at scan time), which would likely result in global cartilage thickness changes, but are actually representing relationships in which thinning in one spatial location on the cartilage surface is accompanied by thickening in another.

There are several potential explanations for this. One hypothesis is that our results represent a process by which the femur cartilage maintains homeostasis; if one part of the cartilage is always thickening when another is thinning, there is no widespread cartilage degeneration. The causes of this could be mechanical (e.g., shifts in weight distribution leading to changes in compression), biological (inflammation at one site recruiting resources from another), or a combination of the two. It is well known that early stages of OA are characterized by increases in cartilage thickness, which have been attributed to an influx of water to the extracellular matrix following increases in aggrecan production by proliferating chondrocytes [40, 206]. It is possible that the dynamics we report here represent transient instances of synthetic chondrocyte activity which serve to repair tissue without initiating long-term inflammation and degradation [207].

Furthermore, most negative correlations exist between subregions that are more central to the knee midline and ones located on the periphery. Previous studies have shown topographical differences on a molecular level within knee cartilage, with peripheral regions of the tibial plateau exhibiting a more organized matrix of collagen fibers and smaller, flatter chondrocytes oriented tangentially to the surface [208]. These results suggest that local cartilage structure develops in response to the direction of maximum load it receives, which will vary along the cartilage surface as a function of underlying bone geometry. It is thus possible that our results capture spatial variations in cartilage response to changes in the global state of the joint (e.g., a change in physical activity patterns eliciting different responses in different anatomical locations depending on variations in load experienced locally). The consistency of these patterns among the control group over an eight-year span suggests that this pattern plays a role in maintaining joint health.

Female sex and obesity are two strong risk factors in developing OA [209]. By investigating the connectome differences between these groups in the control population, we sought to determine whether patterns of cartilage thickness changes exist that are specific to a given demographic. When comparing female and male connectomes within the control group, we see several significant differences, most of which involve the anterior and weight-bearing regions of the femur. We also note the presence of weaker positive correlations and stronger negative correlations in men than women, indicating more widespread similarity in cartilage thickness trajectories in women (i.e., more subregions thickening or thinning simultaneously). Several sex differences have been suggested as possible factors leading to higher OA risk in women that may also relate to the differences seen here. Women tend to have thinner cartilage in the knee joint as well as smaller cartilage volume and surface area [210]. Relatedly, female sex is associated with a thinner patella and femur and a smaller lateral tibial condyle compared to the medial tibial condyle [211, 212]. Sexual dimorphisms in the molecular structure of cartilage may also play a role. It has been shown that estrogen receptors exist in articular cartilage and that estrogen replacement therapy may protect against the development of OA, indicating that hormonal differences impact cartilage properties [212, 213].

Interestingly, we don't see much difference between the connectomes of high and low BMI subjects within our control group. This suggests that subjects with higher BMI who do not develop OA exhibit similar functional cartilage properties to their lower BMI counterparts. It is worth noting that Pearson's correlation is a scale-invariant metric, meaning that it is not influenced by overall cartilage thickness itself but by the amount a change in one time series can be predicted by change in another. Thus, while higher BMI has been associated with changes in overall cartilage thickness related to increased joint loading [214, 215],

the similarities we show here between high and low BMI control subjects may represent a protective mechanism that is not based on absolute cartilage thickness but on cartilage dynamics. Growing evidence suggests that the link between obesity and OA, and the etiology of OA more generally, is not simply attributed "wear-and-tear" in the joints but involves a complex interaction of inflammatory and metabolic processes that may be heightened in high-fat environments [216]. Furthermore, it has been suggested that knee angle plays a large role in mediating the impact of BMI on OA progression [217, 218, 219]. Finally, we acknowledge that alternative metrics to BMI, such as waist circumference and body fat percentage, may provide more information in parsing the relationship between weight and knee OA, although previous studies have found such variables to be highly correlated and affirmed the role of BMI in risk prediction [220, 221].

We observe several significant differences between the connectomes of healthy knees and those that developed OA, many of which involve connections where the control group exhibits stronger negative correlations than the OA incidence group. Much of this statistical relationship appears to be accounted for by the confounding variables of sex, BMI, and knee alignment, although the reduction in subject number when excluding subjects without knee angle data may also decrease the level of statistical power. Our results suggest that cartilage thickness changes within the weight-bearing region of the femur play a particularly important role in OA development. This agrees with previous literature [222]. One particularly relevant study found that cartilage volume loss in OA subjects after 24 months was most pronounced in the central (weight-bearing) areas of the medial and lateral condyles, with medial volume loss exceeding lateral [223]. Interestingly, our results point to a stronger correlation between medial and lateral weight-bearing compartments in the control group compared to OA, suggesting

that asynchronous or imbalanced change between the two weight-bearing compartments may play a role in OA development. Similarly, higher absolute intracorrelation within the medial weight-bearing region in the control group may indicate an adaptive functional relationship between subregions that is less present in the OA group.

Importantly, we acknowledge that the collection of knee MRI images over such a long time scale and at such high resolution is not feasible nor warranted for clinical use [224]. However, our results suggest that a consistent pattern of both thinning and thickening within the same knee cartilage may be a trademark of healthy knee aging, which may provide a new outcome metric for the development of OA therapies. It would be valuable to investigate whether such dynamics are observable on a shorter time scale. Another limitation of our study is the use of only baseline demographics, and future study might involve a more in-depth analysis of knee cartilage changes in relation to changes in knee angle over time as well as associated factors such as BMI, injury incidence, and pain scores. Future research may also involve development of a more complex, patient-specific cartilage parcellation scheme that accounts for anatomical landmarks such as meniscus coverage.

In summary, we present the connectome as a novel analysis method for studying spatiotemporal dynamics of tissue change and demonstrate its utility when applied to knee cartilage thickness trajectories. A key conclusion of this study is that finer-grained parcellation of cartilage reveals differences in longitudinal thickness trajectories that may hold clinical relevance. Consistent patterns are observed in the cartilage thickness trajectories of healthy knees over the span of eight years which are characterized by the presence of synchronous thickening and thinning within different subregions of the same femur surface. Male and female subjects within the control group exhibit highly divergent patterns of

cartilage thickness change. Differences are also found between knees that did and did not develop OA over the course of the study, most of which involve the weight bearing regions of the femur. Sex, BMI, and knee alignment account for some but not all significant differences.

References

[1] Andrew SC Rice, Blair H Smith, et al. "Pain and the global burden of disease". In: *Pain* 157.4 (2016), pp. 791–796.

[2] Srinivasa N Raja, Daniel B Carr, et al. "The revised International Association for the Study of Pain definition of pain: concepts, challenges, and compromises". In: *Pain* 161.9 (2020), pp. 1976–1982.

[3] Rolf-Detlef Treede, Winfried Rief, et al. "Chronic pain as a symptom or a disease: the IASP Classification of Chronic Pain for the International Classification of Diseases (ICD-11)". In: *pain* 160.1 (2019), pp. 19–27.

[4] Muath A Shraim, Hugo Masse-Alarie, et al. "Systematic review and synthesis of mechanism-based classification systems for pain experienced in the musculoskeletal system". In: *The Clinical journal of pain* 36.10 (2020), pp. 793–812.

[5] Muath A Shraim, Hugo Massé-Alarie, et al. "Methods to discriminate between mechanism-based categories of pain experienced in the musculoskeletal system: a systematic review". In: *Pain* 162.4 (2021), pp. 1007–1037.

[6] Steven E Harte, Richard E Harris, et al. "The neurobiology of central sensitization". In: *Journal of Applied Biobehavioral Research* 23.2 (2018), e12137.

[7] Mary-Ann Fitzcharles, Steven P Cohen, et al. “Nociplastic pain: towards an understanding of prevalent pain conditions”. In: *The Lancet* 397.10289 (2021), pp. 2098–2110.

[8] Daniel J Clauw. “Why don’t we use a body map in every chronic pain patient yet?” In: *Pain* 165.8 (2024), pp. 1660–1661.

[9] Frederick Wolfe, Daniel J Clauw, et al. “The American College of Rheumatology preliminary diagnostic criteria for fibromyalgia and measurement of symptom severity”. In: *Arthritis care & research* 62.5 (2010), pp. 600–610.

[10] Chad M Brummett, Rishi R Bakshi, et al. “Preliminary validation of the Michigan body map”. In: *Pain* 157.6 (2016), pp. 1205–1212.

[11] Nanna B Finnerup, Lone Nikolajsen, et al. “Transition from acute to chronic pain: a misleading concept?” In: *Pain* 163.9 (2022), e985–e988.

[12] Paul Glare, Sarah Overton, et al. “Transition from acute to chronic pain: where cells, systems and society meet”. In: *Pain Management* 10.6 (2020), pp. 421–436.

[13] George L Engel. “The need for a new medical model: a challenge for biomedicine”. In: *Science* 196.4286 (1977), pp. 129–136.

[14] S Michaela Rikard. “Chronic pain among adults—United States, 2019–2021”. In: *MMWR. Morbidity and Mortality Weekly Report* 72 (2023).

[15] Christophe Tanguay-Sabourin, Matt Fillingim, et al. “A prognostic risk score for development and spread of chronic pain”. In: *Nature Medicine* 29.7 (2023), pp. 1821–1831.

[16] Matthias J Wieser and Paul Pauli. "Neuroscience of pain and emotion". In: *Neuroscience of Pain, Stress, and Emotion*. Elsevier, 2016, pp. 3–27.

[17] Johan WS Vlaeyen and Steven J Linton. "Fear-avoidance and its consequences in chronic musculoskeletal pain: a state of the art". In: *Pain* 85.3 (2000), pp. 317–332.

[18] Emily L Zale and Joseph W Ditre. "Pain-related fear, disability, and the fear-avoidance model of chronic pain". In: *Current opinion in psychology* 5 (2015), pp. 24–30.

[19] SM Meints and RR Edwards. "Evaluating psychosocial contributions to chronic pain outcomes". In: *Progress in Neuro-Psychopharmacology and Biological Psychiatry* 87 (2018), pp. 168–182.

[20] Kurt Kroenke. "Improvements in Pain or Physical Function and Changes in Depression and Anxiety Symptoms". In: *JAMA Network Open* 6.6 (2023), e2320474–e2320474.

[21] S Jennifer, Benjamin R Brady, et al. "Co-occurrence of chronic pain and anxiety/depression symptoms in US adults: prevalence, functional impacts, and opportunities". In: *Pain* 165.3 (2024), pp. 666–673.

[22] Marion Tegethoff, Angelo Belardi, et al. "Comorbidity of mental disorders and chronic pain: chronology of onset in adolescents of a national representative cohort". In: *The Journal of Pain* 16.10 (2015), pp. 1054–1064.

[23] Wei Zhang, Som P Singh, et al. "Improvements in physical function and pain interference and changes in mental health among patients seeking musculoskeletal care". In: *JAMA Network Open* 6.6 (2023), e2320520–e2320520.

[24] N Mercer Lindsay, C Chen, et al. “Brain circuits for pain and its treatment”. In: *Sci Transl Med* 13.619 (2021).

[25] Prasad Shirvalkar. “Neuromodulation for neuropathic pain syndromes”. In: *CONTINUUM: Lifelong Learning in Neurology* 30.5 (2024), pp. 1475–1500.

[26] Se Won Lee, Jasal Patel, et al. “Use of opioid analgesics in patients with chronic low back pain and knee osteoarthritis”. In: *American Journal of Physical Medicine & Rehabilitation* 98.8 (2019), e97–e98.

[27] Terence W O’Neill and David T Felson. “Mechanisms of osteoarthritis (OA) pain”. In: *Current osteoporosis reports* 16 (2018), pp. 611–616.

[28] Aimin Wu, Lyn March, et al. “Global low back pain prevalence and years lived with disability from 1990 to 2017: estimates from the Global Burden of Disease Study 2017”. In: *Annals of translational medicine* 8.6 (2020).

[29] Chris Maher, Martin Underwood, et al. “Non-specific low back pain”. In: *The Lancet* 389.10070 (2017), pp. 736–747.

[30] Scott D Boden, DO Davis, et al. “Abnormal magnetic-resonance scans of the lumbar spine in asymptomatic subjects. A prospective investigation.” In: *JBJS* 72.3 (1990), pp. 403–408.

[31] Waleed Brinjikji, Patrick H Luetmer, et al. “Systematic literature review of imaging features of spinal degeneration in asymptomatic populations”. In: *American journal of neuroradiology* 36.4 (2015), pp. 811–816.

[32] Brody A Frost, Sandra Camarero-Espinosa, et al. “Materials for the spine: anatomy, problems, and solutions”. In: *Materials* 12.2 (2019), p. 253.

[33] Yoshiaki Ota, Michael Connolly, et al. “Mechanisms and origins of spinal pain: from molecules to anatomy, with diagnostic clues and imaging findings”. In: *Radiographics* 40.4 (2020), pp. 1163–1181.

[34] Jahangir Moini and Pirouz Piran. *Functional and clinical neuroanatomy: a guide for health care professionals*. Academic Press, 2020.

[35] Jasper W van der Graaf, Robert Jan Kroeze, et al. “MRI image features with an evident relation to low back pain: a narrative review”. In: *European Spine Journal* 32.5 (2023), pp. 1830–1841.

[36] Christian WA Pfirrmann, Alexander Metzdorf, et al. “Magnetic resonance classification of lumbar intervertebral disc degeneration”. In: *spine* 26.17 (2001), pp. 1873–1878.

[37] JC Lotz, AJ Fields, et al. “The role of the vertebral end plate in low back pain”. In: *Global spine journal* 3.3 (2013), pp. 153–163.

[38] Michael T Modic, PM Steinberg, et al. “Degenerative disk disease: assessment of changes in vertebral body marrow with MR imaging.” In: *Radiology* 166.1 (1988), pp. 193–199.

[39] Paul Gagnet, Kent Kern, et al. “Spondylolysis and spondylolisthesis: A review of the literature”. In: *Journal of orthopaedics* 15.2 (2018), pp. 404–407.

[40] David J Hunter and Sita Bierma-Zeinstra. “Osteoarthritis”. In: *The Lancet* 393.10182 (2019), pp. 1745–1759.

[41] John Bedson and Peter R Croft. "The discordance between clinical and radiographic knee osteoarthritis: a systematic search and summary of the literature". In: *BMC musculoskeletal disorders* 9 (2008), pp. 1–11.

[42] Jawad F Abulhasan and Michael J Grey. "Anatomy and physiology of knee stability". In: *Journal of Functional Morphology and kinesiology* 2.4 (2017), p. 34.

[43] Sebastian Kopf, Manuel-Paul Sava, et al. "The menisci and articular cartilage: a life-long fascination". In: *EFORT open reviews* 5.10 (2020), pp. 652–662.

[44] Jason J Ivanusic. "Molecular mechanisms that contribute to bone marrow pain". In: *Frontiers in Neurology* 8 (2017), p. 458.

[45] RJ Buck, BT Wyman, et al. "Osteoarthritis may not be a one-way-road of cartilage loss–comparison of spatial patterns of cartilage change between osteoarthritic and healthy knees". In: *Osteoarthritis and Cartilage* 18.3 (2010), pp. 329–335.

[46] Sanjeewa Pradeep Wijayaratne, AJ Teichtahl, et al. "The determinants of change in patella cartilage volume-a cohort study of healthy middle-aged women". In: *Rheumatology* 47.9 (2008), pp. 1426–1429.

[47] Flavia Cicuttini, Anita Wluka, et al. "The determinants of change in patella cartilage volume in osteoarthritic knees." In: *The Journal of rheumatology* 29.12 (2002), pp. 2615–2619.

[48] F Cicuttini, Judy Hankin, et al. "Comparison of conventional standing knee radiographs and magnetic resonance imaging in assessing progression of tibiofemoral joint osteoarthritis". In: *Osteoarthritis and cartilage* 13.8 (2005), pp. 722–727.

[49] RJ Buck, W Wirth, et al. "Frequency and spatial distribution of cartilage thickness change in knee osteoarthritis and its relation to clinical and radiographic covariates–data from the osteoarthritis initiative". In: *Osteoarthritis and cartilage* 21.1 (2013), pp. 102–109.

[50] Sebastian Cotofana, Robert Buck, et al. "Cartilage thickening in early radiographic knee osteoarthritis: A within-person, between-knee comparison". In: *Arthritis care & research* 64.11 (2012), pp. 1681–1690.

[51] Xiaojuan Li and Sharmila Majumdar. "Quantitative MRI of articular cartilage and its clinical applications". In: *Journal of Magnetic Resonance Imaging* 38.5 (2013), pp. 991–1008.

[52] Kathryn Bacon, Michael P LaValley, et al. "Does cartilage loss cause pain in osteoarthritis and if so, how much?" In: *Annals of the rheumatic diseases* 79.8 (2020), pp. 1105–1110.

[53] Xiang-Dong Wu, Di Wu, et al. "Relation between cartilage loss and pain in knee osteoarthritis". In: *Annals of the Rheumatic Diseases* 81.7 (2022), e127–e127.

[54] Javeria A Hashmi, Marwan N Baliki, et al. "Shape shifting pain: chronification of back pain shifts brain representation from nociceptive to emotional circuits". In: *Brain* 136.9 (2013), pp. 2751–2768.

[55] Ellen A Lumpkin, Kara L Marshall, et al. "Review series: The cell biology of touch". In: *The Journal of cell biology* 191.2 (2010), p. 237.

[56] Adrienne E Dubin, Ardem Patapoutian, et al. "Nociceptors: the sensors of the pain pathway". In: *The Journal of clinical investigation* 120.11 (2010), pp. 3760–3772.

[57] Ivan Varga and Boris Mravec. “Nerve fiber types”. In: *Nerves and nerve injuries*. Elsevier, 2015, pp. 107–113.

[58] Luke Grundy, Andelain Erickson, et al. “Visceral pain”. In: *Annual review of physiology* 81.1 (2019), pp. 261–284.

[59] Xiaoli Chang, Haiyan Zhang, et al. “Neural circuits regulating visceral pain”. In: *Communications Biology* 7.1 (2024), p. 457.

[60] Rohini Kuner and Thomas Kuner. “Cellular circuits in the brain and their modulation in acute and chronic pain”. In: *Physiological reviews* (2020).

[61] Glenn J Giesler Jr, James T Katter, et al. “Direct spinal pathways to the limbic system for nociceptive information”. In: *Trends in Neurosciences* 17.6 (1994), pp. 244–250.

[62] Linette Liqi Tan and Rohini Kuner. “Neocortical circuits in pain and pain relief”. In: *Nature Reviews Neuroscience* 22.8 (2021), pp. 458–471.

[63] Harsha Raju and Prasanna Tadi. “Neuroanatomy, somatosensory cortex”. In: *StatPearls [Internet]*. StatPearls Publishing, 2022.

[64] Luis Garcia-Larrea and Roland Peyron. “Pain matrices and neuropathic pain matrices: a review”. In: *PAIN®* 154 (2013), S29–S43.

[65] Marwan N Baliki, Bogdan Petre, et al. “Corticostriatal functional connectivity predicts transition to chronic back pain”. In: *Nature neuroscience* 15.8 (2012), pp. 1117–1119.

[66] Horacio Vanegas, Enrique Vazquez, et al. “NSAIDs, opioids, cannabinoids and the control of pain by the central nervous system”. In: *Pharmaceuticals* 3.5 (2010), pp. 1335–1347.

[67] Qiliang Chen and Mary M Heinricher. "Shifting the balance: how top-down and bottom-up input modulate pain via the rostral ventromedial medulla". In: *Frontiers in Pain Research* 3 (2022), p. 932476.

[68] Iris Coppieters, Mira Meeus, et al. "Relations between brain alterations and clinical pain measures in chronic musculoskeletal pain: a systematic review". In: *The Journal of Pain* 17.9 (2016), pp. 949–962.

[69] M Catherine Bushnell, Marta Čeko, et al. "Cognitive and emotional control of pain and its disruption in chronic pain". In: *Nature reviews neuroscience* 14.7 (2013), pp. 502–511.

[70] Ravi R Bhatt, Elizabeth Haddad, et al. "Mapping brain structure variability in chronic pain: the role of widespreadness and pain type and its mediating relationship with suicide attempt". In: *Biological psychiatry* 95.5 (2024), pp. 473–481.

[71] Ali R Mansour, Marwan N Baliki, et al. "Brain white matter structural properties predict transition to chronic pain". In: *PAIN®* 154.10 (2013), pp. 2160–2168.

[72] Xingyao Chen, Nuo Chen, et al. "Multimodal abnormalities of brain function in chronic low back pain: a systematic review and meta-analysis of neuroimaging studies". In: *Frontiers in Neuroscience* 19 (2025), p. 1535288.

[73] Ali Mansour, Alex T Baria, et al. "Global disruption of degree rank order: a hallmark of chronic pain". In: *Scientific reports* 6.1 (2016), p. 34853.

[74] Kathleen Meacham, Andrew Shepherd, et al. "Neuropathic pain: central vs. peripheral mechanisms". In: *Current pain and headache reports* 21 (2017), pp. 1–11.

[75] Joseph P Hornak. *"The Basics of NMR"*. Rochester: Rochester Institute of Technology, 2024.

[76] Ray Hashman Hashemi, William G Bradley, et al. *MRI: the basics: The Basics*. 4th ed. Lippincott Williams & Wilkins, 2018.

[77] Peter A Hardy, Michael P Recht, et al. "Optimization of a dual echo in the steady state (DESS) free-precession sequence for imaging cartilage". In: *Journal of Magnetic Resonance Imaging* 6.2 (1996), pp. 329–335.

[78] Peter A Bandettini. *Fmri*. MIT Press, 2020.

[79] Rasmus M Birn, Erin K Molloy, et al. "The effect of scan length on the reliability of resting-state fMRI connectivity estimates". In: *Neuroimage* 83 (2013), pp. 550–558.

[80] Burak Kocak. "Artificial intelligence to predict task activation from resting state fMRI". In: *European Radiology* 31.7 (2021), pp. 5251–5252.

[81] Julia Tuominen, Karsten Specht, et al. "An information-theoretic analysis of resting-state versus task fMRI". In: *Network Neuroscience* 7.2 (2023), pp. 769–786.

[82] Emily S Finn. "Is it time to put rest to rest?" In: *Trends in cognitive sciences* 25.12 (2021), pp. 1021–1032.

[83] Thomas T Liu, Alican Nalci, et al. "The global signal in fMRI: Nuisance or Information?" In: *Neuroimage* 150 (2017), pp. 213–229.

[84] Krzysztof J Gorgolewski, Tibor Auer, et al. "The brain imaging data structure, a format for organizing and describing outputs of neuroimaging experiments". In: *Scientific data* 3.1 (2016), pp. 1–9.

[85] Russell A Poldrack, Chris I Baker, et al. "Scanning the horizon: towards transparent and reproducible neuroimaging research". In: *Nature reviews neuroscience* 18.2 (2017), pp. 115–126.

[86] Oscar Esteban, Christopher Markiewicz, et al. "fMRIPrep: a robust preprocessing pipeline for functional MRI". In: *Nature Methods* (2018). DOI: 10.1038/s41592-018-0235-4.

[87] Oscar Esteban, Ross Blair, et al. "fMRIPrep". In: *Software* (2018). DOI: 10.5281/zenodo.852659.

[88] Oscar Esteban, Daniel Birman, et al. "MRIQC: Advancing the automatic prediction of image quality in MRI from unseen sites". In: *PloS one* 12.9 (2017), e0184661.

[89] Alexandre Abraham, Fabian Pedregosa, et al. "Machine learning for neuroimaging with scikit-learn". English. In: *Frontiers in Neuroinformatics* 8 (2014). ISSN: 1662-5196. DOI: 10.3389/fninf.2014.00014. URL: https://www.frontiersin.org/articles/10.3389/fninf.2014.00014/full.

[90] Nilearn contributors. *nilearn*. DOI: https://doi.org/10.5281/zenodo.8397156. URL: https://github.com/nilearn/nilearn.

[91] Rangaswami Balakrishnan and Kanna Ranganathan. *A textbook of graph theory*. Springer Science & Business Media, 2012.

[92] Olaf Sporns, Giulio Tononi, et al. "The human connectome: a structural description of the human brain". In: *PLoS computational biology* 1.4 (2005), e42.

[93] O Sporns. *Discovering the Human Connectome*. The MIT Press, 2012.

[94] Jennifer Stine Elam, Matthew F Glasser, et al. “The human connectome project: a retrospective”. In: *NeuroImage* 244 (2021), p. 118543.

[95] John G White, Eileen Southgate, et al. “The structure of the nervous system of the nematode Caenorhabditis elegans”. In: *Philos Trans R Soc Lond B Biol Sci* 314.1165 (1986), pp. 1–340.

[96] Steven J Cook, Travis A Jarrell, et al. “Whole-animal connectomes of both Caenorhabditis elegans sexes”. In: *Nature* 571.7763 (2019), pp. 63–71.

[97] Philipp Schlegel, Yijie Yin, et al. “Whole-brain annotation and multi-connectome cell typing of Drosophila”. In: *Nature* 634.8032 (2024), pp. 139–152.

[98] Sven Dorkenwald, Arie Matsliah, et al. “Neuronal wiring diagram of an adult brain”. In: *Nature* 634.8032 (2024), pp. 124–138.

[99] Alessandro Motta, Manuel Berning, et al. “Dense connectomic reconstruction in layer 4 of the somatosensory cortex”. In: *Science* 366.6469 (2019), eaay3134.

[100] Nicholas L Turner, Thomas Macrina, et al. “Reconstruction of neocortex: Organelles, compartments, cells, circuits, and activity”. In: *Cell* 185.6 (2022), pp. 1082–1100.

[101] Anushree Chatterjee, Yiannis N Kaznessis, et al. “Tweaking biological switches through a better understanding of bistability behavior”. In: *Current opinion in biotechnology* 19.5 (2008), pp. 475–481.

[102] Danielle S Bassett and Edward T Bullmore. “Small-world brain networks revisited”. In: *The Neuroscientist* 23.5 (2017), pp. 499–516.

[103] Ed Bullmore and Olaf Sporns. "Complex brain networks: graph theoretical analysis of structural and functional systems". In: *Nature reviews neuroscience* 10.3 (2009), pp. 186–198.

[104] Biyu J He, John M Zempel, et al. "The temporal structures and functional significance of scale-free brain activity". In: *Neuron* 66.3 (2010), pp. 353–369.

[105] Hualou Liang and Hongbin Wang. "Structure-function network mapping and its assessment via persistent homology". In: *PLoS computational biology* 13.1 (2017), e1005325.

[106] Paul L Nunez. "The brain wave equation: a model for the EEG". In: *Mathematical Biosciences* 21.3-4 (1974), pp. 279–297.

[107] Viktor K Jirsa and Hermann Haken. "A derivation of a macroscopic field theory of the brain from the quasi-microscopic neural dynamics". In: *Physica D: Nonlinear Phenomena* 99.4 (1997), pp. 503–526.

[108] PA Valdes, Juan C Jiménez, et al. "Nonlinear EEG analysis based on a neural mass model". In: *Biological cybernetics* 81.5 (1999), pp. 415–424.

[109] Christopher J Honey, Olaf Sporns, et al. "Predicting human resting-state functional connectivity from structural connectivity". In: *Proceedings of the National Academy of Sciences* 106.6 (2009), pp. 2035–2040.

[110] Andreas Spiegler and V Jirsa. "Systematic approximations of neural fields through networks of neural masses in the virtual brain". In: *Neuroimage* 83 (2013), pp. 704–725.

[111] Farras Abdelnour, Henning U Voss, et al. "Network diffusion accurately models the relationship between structural and functional brain connectivity networks". In: *Neuroimage* 90 (2014), pp. 335–347.

[112] Ashish Raj, Chang Cai, et al. "Spectral graph theory of brain oscillations". In: *Human brain mapping* 41.11 (2020), pp. 2980–2998.

[113] Erfan Nozari, Jennifer Stiso, et al. "Is the brain macroscopically linear? A system identification of resting state dynamics". In: *arXiv preprint arXiv:2012.12351* (2020).

[114] Farras Abdelnour, Michael Dayan, et al. "Functional brain connectivity is predictable from anatomic network's Laplacian eigen-structure". In: *NeuroImage* 172 (2018), pp. 728–739.

[115] Selen Atasoy, Isaac Donnelly, et al. "Human brain networks function in connectome-specific harmonic waves". In: *Nature communications* 7.1 (2016), pp. 1–10.

[116] Peter A Robinson, X Zhao, et al. "Eigenmodes of brain activity: Neural field theory predictions and comparison with experiment". In: *NeuroImage* 142 (2016), pp. 79–98.

[117] Maria Giulia Preti and Dimitri Van De Ville. "Decoupling of brain function from structure reveals regional behavioral specialization in humans". In: *Nature communications* 10.1 (2019), p. 4747.

[118] Xihe Xie, Chang Cai, et al. "Emergence of canonical functional networks from the structural connectome". In: *NeuroImage* 237 (2021), p. 118190.

[119] Jil Meier, Prejaas Tewarie, et al. "A mapping between structural and functional brain networks". In: *Brain connectivity* 6.4 (2016), pp. 298–311.

[120] Cassiano O Becker, Sérgio Pequito, et al. "Spectral mapping of brain functional connectivity from diffusion imaging". In: *Scientific reports* 8.1 (2018), pp. 1–15.

[121] Samuel Deslauriers-Gauthier, Mauro Zucchelli, et al. "A unified framework for multi-modal structure-function mapping based on eigenmodes". In: *Medical Image Analysis* 66 (2020), p. 101799. ISSN: 1361-8415. DOI: https://doi.org/10.1016/j.media.2020.101799.

[122] Prejaas Tewarie, Bastian Prasse, et al. "Mapping functional brain networks from the structural connectome: Relating the series expansion and eigenmode approaches". In: *NeuroImage* 216 (2020), p. 116805.

[123] Sébastien Naze, Timothée Proix, et al. "Robustness of connectome harmonics to local gray matter and long-range white matter connectivity changes". In: *NeuroImage* 224 (2020), p. 117364.

[124] Julia P Owen, Yi-Ou Li, et al. "Resting-state networks and the functional connectome of the human brain in agenesis of the corpus callosum". In: *Brain connectivity* 3.6 (2013), pp. 547–562.

[125] Florian Beissner, Ralf Deichmann, et al. "fMRI of the brainstem using dual-echo EPI". In: *NeuroImage* 55.4 (2011), pp. 1593–1599.

[126] Jonathan Charles William Brooks, Olivia Kate Faull, et al. "Physiological noise in brainstem FMRI". In: *Frontiers in human neuroscience* 7 (2013), p. 623.

[127] N. J. Tustison, B. B. Avants, et al. "N4ITK: Improved N3 Bias Correction". In: *IEEE Transactions on Medical Imaging* 29.6 (2010), pp. 1310–1320. ISSN: 0278-0062. DOI: 10.1109/TMI.2010.2046908.

[128] B.B. Avants, C.L. Epstein, et al. "Symmetric diffeomorphic image registration with cross-correlation: Evaluating automated labeling of elderly and neurodegenerative brain". In: *Medical Image Analysis* 12.1 (2008), pp. 26–41. ISSN: 1361-8415. DOI: 10.1016/j.media.2007.06.004. URL: http://www.sciencedirect.com/science/article/pii/S1361841507000606.

[129] Y. Zhang, M. Brady, et al. "Segmentation of brain MR images through a hidden Markov random field model and the expectation-maximization algorithm". In: *IEEE Transactions on Medical Imaging* 20.1 (2001), pp. 45–57. ISSN: 0278-0062. DOI: 10.1109/42.906424.

[130] VS Fonov, AC Evans, et al. "Unbiased nonlinear average age-appropriate brain templates from birth to adulthood". In: *NeuroImage* 47, Supplement 1 (2009), S102. DOI: 10.1016/S1053-8119(09)70884-5.

[131] K. Gorgolewski, C. D. Burns, et al. "Nipype: a flexible, lightweight and extensible neuroimaging data processing framework in Python". In: *Frontiers in Neuroinformatics* 5 (2011), p. 13. DOI: 10.3389/fninf.2011.00013.

[132] Krzysztof J. Gorgolewski, Oscar Esteban, et al. "Nipype". In: *Software* (2018). DOI: 10.5281/zenodo.596855.

[133] Mark Jenkinson and Stephen Smith. "A global optimisation method for robust affine registration of brain images". In: *Medical Image Analysis* 5.2 (2001), pp. 143–156. ISSN: 1361-8415. DOI: 10.1016/S1361-8415(01)00036-6. URL: http://www.sciencedirect.com/science/article/pii/S1361841501000366 (visited on 07/27/2018).

[134] Douglas N Greve and Bruce Fischl. "Accurate and robust brain image alignment using boundary-based registration". In: *NeuroImage* 48.1 (2009), pp. 63–72. ISSN: 1095-9572. DOI: 10.1016/j.neuroimage.2009.06.060.

[135] Mark Jenkinson, Peter Bannister, et al. "Improved Optimization for the Robust and Accurate Linear Registration and Motion Correction of Brain Images". In: *NeuroImage* 17.2 (2002), pp. 825–841. ISSN: 1053-8119. DOI: 10.1006/nimg.2002.1132. URL: http://www.sciencedirect.com/science/article/pii/S1053811902911328.

[136] Robert W. Cox and James S. Hyde. "Software tools for analysis and visualization of fMRI data". In: *NMR in Biomedicine* 10.4-5 (1997), pp. 171–178. DOI: 10.1002/(SICI)1099-1492(199706/08)10:4/5<171::AID-NBM453>3.0.CO;2-L.

[137] Raimon H. R. Pruim, Maarten Mennes, et al. "ICA-AROMA: A robust ICA-based strategy for removing motion artifacts from fMRI data". In: *NeuroImage* 112.Supplement C (2015), pp. 267–277. ISSN: 1053-8119. DOI: 10.1016/j.neuroimage.2015.02.064. URL: http://www.sciencedirect.com/science/article/pii/S1053811915001822.

[138] Jonathan D. Power, Anish Mitra, et al. "Methods to detect, characterize, and remove motion artifact in resting state fMRI". In: *NeuroImage* 84.Supplement C (2014), pp. 320–341. ISSN: 1053-8119. DOI: 10.1016/j.neuroimage.2013.08.048. URL: http://www.sciencedirect.com/science/article/pii/S1053811913009117.

[139] C. Lanczos. "Evaluation of Noisy Data". In: *Journal of the Society for Industrial and Applied Mathematics Series B Numerical Analysis* 1.1 (1964), pp. 76–85. ISSN:

0887-459X. DOI: 10.1137/0701007. URL: http://epubs.siam.org/doi/10.1137/0701007.

[140] Rahul S Desikan, Florent Ségonne, et al. "An automated labeling system for subdividing the human cerebral cortex on MRI scans into gyral based regions of interest". In: *Neuroimage* 31.3 (2006), pp. 968–980.

[141] Jennifer A. McNab, Brian L. Edlow, et al. "The Human Connectome Project and beyond: Initial applications of 300mT/m gradients". In: *NeuroImage* (2013). ISSN: 10538119. DOI: 10.1016/j.neuroimage.2013.05.074.

[142] Bruce Fischl, David H Salat, et al. "Whole Brain Segmentation : Automated Labeling of Neuroanatomical Structures in the Human Brain". In: *Neuron* 33 (2002), pp. 341–355.

[143] Mark Jenkinson, Christian F. Beckmann, et al. "FSL". In: *NeuroImage* 62.2 (Aug. 2012), pp. 782–790. ISSN: 1053-8119. DOI: 10.1016/J.NEUROIMAGE.2011.09.015. URL: https://www.sciencedirect.com/science/article/pii/S1053811911010603?via%7B%5C%%7D3Dihub.

[144] Farras Abdelnour, Michael Dayan, et al. "Algebraic relationship between the structural network's Laplacian and functional network's adjacency matrix is preserved in temporal lobe epilepsy subjects". In: *NeuroImage* 228 (2021), p. 117705.

[145] Alex Fornito, Andrew Zalesky, et al. "Schizophrenia, neuroimaging and connectomics". In: *Neuroimage* 62.4 (2012), pp. 2296–2314.

[146] Martijn P Van Den Heuvel and Alex Fornito. "Brain networks in schizophrenia". In: *Neuropsychology review* 24.1 (2014), pp. 32–48.

[147] Weiyu Huang, Thomas AW Bolton, et al. "A graph signal processing perspective on functional brain imaging". In: *Proceedings of the IEEE* 106.5 (2018), pp. 868–885.

[148] John D Medaglia, Weiyu Huang, et al. "Functional alignment with anatomical networks is associated with cognitive flexibility". In: *Nature human behaviour* 2.2 (2018), pp. 156–164.

[149] ML Saggio, P Ritter, et al. "Analytical Operations Relate Structural and Functional Connectivity in the Brain". In: *PLoS ONE* 11.8 (2016), 11(8): e0157292. DOI: 10.1371/journal.pone.0157292. URL: https://doi.org/10.1371/journal.pone.0157292.

[150] Raphael Liegeois, Augusto Santos, et al. "Revisiting correlation-based functional connectivity and its relationship with structural connectivity". In: *Network Neuroscience* 4.4 (Dec. 2020), pp. 1235–1251. ISSN: 2472-1751. DOI: 10.1162/netn_a_00166. eprint: https://direct.mit.edu/netn/article-pdf/4/4/1235/1867105/netn_a_00166.pdf. URL: https://doi.org/10.1162/netn%5C_a%5C_00166.

[151] Christoph WU Leuze, Alfred Anwander, et al. "Layer-specific intracortical connectivity revealed with diffusion MRI". In: *Cerebral Cortex* 24.2 (2014), pp. 328–339.

[152] Julia P Owen, Yi-Ou Li, et al. "The structural connectome of the human brain in agenesis of the corpus callosum". In: *Neuroimage* 70 (2013), pp. 340–355.

[153] David E Stark, Daniel S Margulies, et al. "Regional variation in interhemispheric coordination of intrinsic hemodynamic fluctuations". In: *Journal of Neuroscience* 28.51 (2008), pp. 13754–13764.

[154] Mara Fabri, Chiara Pierpaoli, et al. "Functional topography of the corpus callosum investigated by DTI and fMRI". In: *World journal of radiology* 6.12 (2014), p. 895.

[155] Lucina Q Uddin, Eric Mooshagian, et al. "Residual functional connectivity in the split-brain revealed with resting-state fMRI". In: *Neuroreport* 19.7 (2008), p. 703.

[156] J Michael Tyszka, Daniel P Kennedy, et al. "Intact bilateral resting-state networks in the absence of the corpus callosum". In: *Journal of Neuroscience* 31.42 (2011), pp. 15154–15162.

[157] Jill X O'Reilly, Paula L Croxson, et al. "Causal effect of disconnection lesions on interhemispheric functional connectivity in rhesus monkeys". In: *Proceedings of the National Academy of Sciences* 110.34 (2013), pp. 13982–13987.

[158] Lucina Q Uddin. "Complex relationships between structural and functional brain connectivity". In: *Trends in cognitive sciences* 17.12 (2013), pp. 600–602.

[159] Antonio Meola, Fang-Cheng Yeh, et al. "Human connectome-based tractographic atlas of the brainstem connections and surgical approaches". In: *Neurosurgery* 79.3 (2016), pp. 437–455.

[160] Yu Zhang, Andrei A Vakhtin, et al. "Diffusion tensor tractography of brainstem fibers and its application in pain". In: *PloS one* 15.2 (2020), e0213952.

[161] Steven J Kamper, Andreas T Apeldoorn, et al. "Multidisciplinary biopsychosocial rehabilitation for chronic low back pain". In: *Cochrane Database of Systematic Reviews* 9 (2014).

[162] Jeroen Kregel, Mira Meeus, et al. "Structural and functional brain abnormalities in chronic low back pain: a systematic review". In: *Seminars in arthritis and rheumatism*. Vol. 45. 2. Elsevier. 2015, pp. 229–237.

[163] Shin-ichi Konno and Miho Sekiguchi. “Association between brain and low back pain”. In: *Journal of Orthopaedic Science* 23.1 (2018), pp. 3–7.

[164] Xuyang Li, Fancheng Meng, et al. “The Alterations in the Brain Corresponding to Low Back Pain: Recent Insights and Advances”. In: *Neural Plasticity* 2024.1 (2024), p. 5599046.

[165] David A Seminowicz, Timothy H Wideman, et al. “Effective treatment of chronic low back pain in humans reverses abnormal brain anatomy and function”. In: *Journal of Neuroscience* 31.20 (2011), pp. 7540–7550.

[166] Zeynab Alshelh, Flavia Di Pietro, et al. “Chronic neuropathic pain: it’s about the rhythm”. In: *Journal of Neuroscience* 36.3 (2016), pp. 1008–1018.

[167] Zeynab Alshelh, Ludovica Brusaferri, et al. “Neuroimmune signatures in chronic low back pain subtypes”. In: *Brain* 145.3 (2022), pp. 1098–1110.

[168] Harold Hotelling. “Relations between two sets of variates”. In: *Breakthroughs in statistics: methodology and distribution*. Springer, 1992, pp. 162–190.

[169] Hao-Ting Wang, Jonathan Smallwood, et al. “Finding the needle in a high-dimensional haystack: Canonical correlation analysis for neuroscientists”. In: *NeuroImage* 216 (2020), p. 116745.

[170] Xiaowei Zhuang, Zhengshi Yang, et al. “A technical review of canonical correlation analysis for neuroscience applications”. In: *Human brain mapping* 41.13 (2020), pp. 3807–3833.

[171] Agoston Mihalik, James Chapman, et al. "Canonical correlation analysis and partial least squares for identifying brain–behavior associations: A tutorial and a comparative study". In: *Biological Psychiatry: Cognitive Neuroscience and Neuroimaging* 7.11 (2022), pp. 1055–1067.

[172] Andrew T Drysdale, Logan Grosenick, et al. "Resting-state connectivity biomarkers define neurophysiological subtypes of depression". In: *Nature medicine* 23.1 (2017), pp. 28–38.

[173] Amanda M Buch, Petra E Vértes, et al. "Molecular and network-level mechanisms explaining individual differences in autism spectrum disorder". In: *Nature neuroscience* 26.4 (2023), pp. 650–663.

[174] Regina LM van Boekel, Kris CP Vissers, et al. "Moving beyond pain scores: Multidimensional pain assessment is essential for adequate pain management after surgery". In: *PLoS One* 12.5 (2017), e0177345.

[175] Kristen Hymel Scherrer, Maisa S Ziadni, et al. "Development and validation of the Collaborative Health Outcomes Information Registry body map". In: *Pain reports* 6.1 (2021), e880.

[176] Trisha F Hue, Jeffrey C Lotz, et al. "Design of the COMEBACK and BACKHOME Studies, Longitudinal Cohorts for Comprehensive Deep Phenotyping of Adults with Chronic Low-Back Pain (cLBP): a part of the BACPAC Research Program". In: *medRxiv* (2024).

[177] Aric A. Hagberg, Daniel A. Schult, et al. “Exploring Network Structure, Dynamics, and Function using NetworkX”. In: *Proceedings of the 7th Python in Science Conference*. Ed. by Gaël Varoquaux, Travis Vaught, et al. Pasadena, CA USA, 2008, pp. 11–15.

[178] Lingzhong Fan, Hai Li, et al. “The human brainnetome atlas: a new brain atlas based on connectional architecture”. In: *Cerebral cortex* 26.8 (2016), pp. 3508–3526.

[179] Natalia Y Bilenko and Jack L Gallant. “Pyrcca: regularized kernel canonical correlation analysis in python and its applications to neuroimaging”. In: *Frontiers in neuroinformatics* 10 (2016), p. 49.

[180] Jereen Kwong, Joanna Lin, et al. “Quantifying Pain Location and Intensity with Multimodal Pain Body Diagrams”. In: *JoVE (Journal of Visualized Experiments)* 197 (2023), e65334.

[181] Muath A Shraim, Hugo Massé-Alarie, et al. “Neuroinflammatory activation in sensory and motor regions of the cortex is related to sensorimotor function in individuals with low back pain maintained by nociplastic mechanisms: A preliminary proof-of-concept study”. In: *European Journal of Pain* 28.9 (2024), pp. 1607–1626.

[182] Wei Shen, Yiheng Tu, et al. “Visual network alterations in brain functional connectivity in chronic low back pain: A resting state functional connectivity and machine learning study”. In: *NeuroImage: Clinical* 22 (2019), p. 101775.

[183] Peter Schwenkreis, Andrea Scherens, et al. “Cortical disinhibition occurs in chronic neuropathic, but not in chronic nociceptive pain”. In: *BMC neuroscience* 11 (2010), pp. 1–10.

[184] David J Hunter, Lyn March, et al. "Osteoarthritis in 2020 and beyond: a Lancet Commission". In: *The Lancet* 396.10264 (2020), pp. 1711–1712.

[185] Richard F Loeser, Steven R Goldring, et al. "Osteoarthritis: a disease of the joint as an organ". In: *Arthritis and rheumatism* 64.6 (2012), p. 1697.

[186] Steven R Goldring and Mary B Goldring. "Changes in the osteochondral unit during osteoarthritis: structure, function and cartilage–bone crosstalk". In: *Nature Reviews Rheumatology* 12.11 (2016), pp. 632–644.

[187] Sunhee Jang, Kijun Lee, et al. "Recent Updates of Diagnosis, Pathophysiology, and Treatment on Osteoarthritis of the Knee". In: *International journal of molecular sciences* 22.5 (2021), p. 2619.

[188] Yuriy Nalapko, Dmytro Klokol, et al. "Novel Bioregenerative Options for Chondrocyte Restoration in Osteoarthritis". In: *Stem Cells Regen Med* 6.1 (2022), pp. 1–8.

[189] F Eckstein, JE Collins, et al. "Brief report: cartilage thickness change as an imaging biomarker of knee osteoarthritis progression: data from the Foundation for the National Institutes of Health Osteoarthritis Biomarkers Consortium". In: *Arthritis & rheumatology* 67.12 (2015), pp. 3184–3189.

[190] W Wirth, DJ Hunter, et al. "Predictive and concurrent validity of cartilage thickness change as a marker of knee osteoarthritis progression: data from the Osteoarthritis Initiative". In: *Osteoarthritis and cartilage* 25.12 (2017), pp. 2063–2071.

[191] F Eckstein, W Wirth, et al. "Five-year followup of knee joint cartilage thickness changes after acute rupture of the anterior cruciate ligament". In: *Arthritis & rheumatology* 67.1 (2015), pp. 152–161.

[192] Claudia Iriondo, Felix Liu, et al. "Towards understanding mechanistic subgroups of osteoarthritis: 8-year cartilage thickness trajectory analysis". In: *Journal of Orthopaedic Research®* 39.6 (2021), pp. 1305–1317.

[193] Hugo Babel, Patrick Omoumi, et al. "New insight on the subchondral bone and cartilage functional unit: Bone mineral density and cartilage thickness are spatially correlated in non-osteoarthritic femoral condyles". In: *Osteoarthritis and Cartilage Open* 2.3 (2020), p. 100079.

[194] Romil F Shah, Alejandro M Martinez, et al. "Variation in the thickness of knee cartilage. The use of a novel machine learning algorithm for cartilage segmentation of magnetic resonance images". In: *The Journal of arthroplasty* 34.10 (2019), pp. 2210–2215.

[195] M-P Hellio Le Graverand, RJ Buck, et al. "Subregional femorotibial cartilage morphology in women–comparison between healthy controls and participants with different grades of radiographic knee osteoarthritis". In: *Osteoarthritis and cartilage* 17.9 (2009), pp. 1177–1185.

[196] Julien Favre, Sean F Scanlan, et al. "Patterns of femoral cartilage thickness are different in asymptomatic and osteoarthritic knees and can be used to detect disease-related differences between samples". In: *Journal of biomechanical engineering* 135.10 (2013), p. 101002.

[197] Julien Favre, Jennifer C Erhart-Hledik, et al. "Anatomically standardized maps reveal distinct patterns of cartilage thickness with increasing severity of medial compartment knee osteoarthritis". In: *Journal of orthopaedic research* 35.11 (2017), pp. 2442–2451.

[198] Charles G Peterfy, Erika Schneider, et al. "The osteoarthritis initiative: report on the design rationale for the magnetic resonance imaging protocol for the knee". In: *Osteoarthritis and cartilage* 16.12 (2008), pp. 1433–1441.

[199] Mark D Kohn, Adam A Sassoon, et al. "Classifications in brief: Kellgren-Lawrence classification of osteoarthritis". In: *Clinical Orthopaedics and Related Research®* 474.8 (2016), pp. 1886–1893.

[200] T Iranpour-Boroujeni, J Li, et al. "A new method to measure anatomic knee alignment for large studies of OA: data from the Osteoarthritis Initiative". In: *Osteoarthritis and cartilage* 22.10 (2014), pp. 1668–1674.

[201] Alejandro Morales Martinez, Francesco Caliva, et al. "Learning osteoarthritis imaging biomarkers from bone surface spherical encoding". In: *Magnetic resonance in medicine* 84.4 (2020), pp. 2190–2203.

[202] Alejandro G Morales, Jinhee J Lee, et al. "Uncovering associations between data-driven learned qMRI biomarkers and chronic pain". In: *Scientific reports* 11.1 (2021), pp. 1–14.

[203] Herve Lombaert, Leo Grady, et al. "FOCUSR: feature oriented correspondence using spectral regularization–a method for precise surface matching". In: *IEEE transactions on pattern analysis and machine intelligence* 35.9 (2012), pp. 2143–2160.

[204] Paul J Besl and Neil D McKay. "Method for registration of 3-D shapes". In: *Sensor fusion IV: control paradigms and data structures*. Vol. 1611. Spie. 1992, pp. 586–606.

[205] Dan R Jørgensen, Martin Lillholm, et al. "On subregional analysis of cartilage loss from knee MRI". In: *Cartilage* 4.2 (2013), pp. 121–130.

[206] Maricela Maldonado and Jin Nam. "The role of changes in extracellular matrix of cartilage in the presence of inflammation on the pathology of osteoarthritis". In: *BioMed research international* 2013.1 (2013), p. 284873.

[207] Thomas P Andriacchi, Anne Mündermann, et al. "A framework for the in vivo pathomechanics of osteoarthritis at the knee". In: *Annals of biomedical engineering* 32.3 (2004), pp. 447–457.

[208] AM Chaudhari, Paul L Briant, et al. "Knee kinematics, cartilage morphology, and osteoarthritis after ACL injury." In: *Medicine and science in sports and exercise* 40.2 (2008), pp. 215–222.

[209] V Silverwood, M Blagojevic-Bucknall, et al. "Current evidence on risk factors for knee osteoarthritis in older adults: a systematic review and meta-analysis". In: *Osteoarthritis and cartilage* 23.4 (2015), pp. 507–515.

[210] SC Faber, F Eckstein, et al. "Gender differences in knee joint cartilage thickness, volume and articular surface areas: assessment with quantitative three-dimensional MR imaging". In: *Skeletal radiology* 30.3 (2001), pp. 144–150.

[211] Kirby Hitt, John R Shurman, et al. "Anthropometric measurements of the human knee: correlation to the sizing of current knee arthroplasty systems". In: *JBJS* 85.suppl_4 (2003), pp. 115–122.

[212] Mary I O'Connor. "Osteoarthritis of the hip and knee: sex and gender differences". In: *Orthopedic Clinics* 37.4 (2006), pp. 559–568.

[213] Renee S Richmond, Cathy S Carlson, et al. "Functional estrogen receptors in adult articular cartilage: Estrogen replacement therapy increases chondrocyte synthesis

of proteoglycans and insulin-like growth factor binding protein 2". In: *Arthritis & Rheumatism: Official Journal of the American College of Rheumatology* 43.9 (2000), pp. 2081–2090.

[214] Veronica Mezhov, Flavia M Ciccutini, et al. "Does obesity affect knee cartilage? A systematic review of magnetic resonance imaging data". In: *Obesity reviews* 15.2 (2014), pp. 143–157.

[215] Katerina Blazek, Julien Favre, et al. "Age and obesity alter the relationship between femoral articular cartilage thickness and ambulatory loads in individuals without osteoarthritis". In: *Journal of Orthopaedic Research* 32.3 (2014), pp. 394–402.

[216] MaryFran R Sowers and Carrie A Karvonen-Gutierrez. "The evolving role of obesity in knee osteoarthritis". In: *Current opinion in rheumatology* 22.5 (2010), p. 533.

[217] Leena Sharma, Congrong Lou, et al. "The mechanism of the effect of obesity in knee osteoarthritis: the mediating role of malalignment". In: *Arthritis & Rheumatism: Official Journal of the American College of Rheumatology* 43.3 (2000), pp. 568–575.

[218] Rebecca F Moyer, Trevor B Birmingham, et al. "Alignment, body mass and their interaction on dynamic knee joint load in patients with knee osteoarthritis". In: *Osteoarthritis and cartilage* 18.7 (2010), pp. 888–893.

[219] Ryan Lee and Walter F Kean. "Obesity and knee osteoarthritis". In: *Inflammopharmacology* 20.2 (2012), pp. 53–58.

[220] L Stefan Lohmander, M Gerhardsson De Verdier, et al. "Incidence of severe knee and hip osteoarthritis in relation to different measures of body mass: a population-based

prospective cohort study". In: *Annals of the rheumatic diseases* 68.4 (2009), pp. 490–496.

[221] KL Holliday, DF McWilliams, et al. "Lifetime body mass index, other anthropometric measures of obesity and risk of knee or hip osteoarthritis in the GOAL case-control study". In: *Osteoarthritis and Cartilage* 19.1 (2011), pp. 37–43.

[222] RL Karvonen, WG Negendank, et al. "Factors affecting articular cartilage thickness in osteoarthritis and aging." In: *The Journal of rheumatology* 21.7 (1994), pp. 1310–1318.

[223] Jean-Pierre Pelletier, Jean-Pierre Raynauld, et al. "Risk factors associated with the loss of cartilage volume on weight-bearing areas in knee osteoarthritis patients assessed by quantitative magnetic resonance imaging: a longitudinal study". In: *Arthritis research & therapy* 9.4 (2007), pp. 1–11.

[224] Lori Lyn Price, Matthew S Harkey, et al. "Role of magnetic resonance imaging in classifying individuals who will develop accelerated radiographic knee osteoarthritis". In: *Journal of Orthopaedic Research®* 37.11 (2019), pp. 2420–2428.

[225] Alessandra Griffa, Yasser Aleman-Gomez, et al. *Structural and functional connectome from 70 young healthy adults*. 2019. DOI: 10.5281/zenodo.2872624. URL: https://doi.org/10.5281/zenodo.2872624.

[226] Leila Cammoun, Xavier Gigandet, et al. "Mapping the human connectome at multiple scales with diffusion spectrum MRI". In: *Journal of neuroscience methods* 203.2 (2012), pp. 386–397.

[227] Anders M. Dale, Bruce Fischl, et al. "Cortical Surface-Based Analysis: I. Segmentation and Surface Reconstruction". In: *NeuroImage* 9.2 (1999), pp. 179–194. ISSN: 1053-8119.

DOI: 10.1006/nimg.1998.0395. URL: http://www.sciencedirect.com/science/article/pii/S1053811998903950.

[228] Arno Klein, Satrajit S. Ghosh, et al. "Mindboggling morphometry of human brains". In: *PLOS Computational Biology* 13.2 (2017), e1005350. ISSN: 1553-7358. DOI: 10.1371/journal.pcbi.1005350. URL: http://journals.plos.org/ploscompbiol/article?id=10.1371/journal.pcbi.1005350.

[229] AC Evans, AL Janke, et al. "Brain templates and atlases". In: *NeuroImage* 62.2 (2012), pp. 911–922. DOI: 10.1016/j.neuroimage.2012.01.024.

[230] Sijia Wang, Daniel J. Peterson, et al. "Evaluation of Field Map and Nonlinear Registration Methods for Correction of Susceptibility Artifacts in Diffusion MRI". English. In: *Frontiers in Neuroinformatics* 11 (2017). ISSN: 1662-5196. DOI: 10.3389/fninf.2017.00017. URL: http://journal.frontiersin.org/article/10.3389/fninf.2017.00017/full.

[231] Julia M. Huntenburg. "Evaluating nonlinear coregistration of BOLD EPI and T1w images". eng. Master's Thesis. Berlin: Freie Universitat, 2014. URL: http://hdl.handle.net/11858/00-001M-0000-002B-1CB5-A.

[232] Jeffrey Mark Treiber, Nathan S. White, et al. "Characterization and Correction of Geometric Distortions in 814 Diffusion Weighted Images". In: *PLOS ONE* 11.3 (2016), e0152472. ISSN: 1932-6203. DOI: 10.1371/journal.pone.0152472. URL: http://journals.plos.org/plosone/article?id=10.1371/journal.pone.0152472.

[233] Yashar Behzadi, Khaled Restom, et al. "A component based noise correction method (CompCor) for BOLD and perfusion based fMRI". In: *NeuroImage* 37.1 (2007),

pp. 90–101. ISSN: 1053-8119. DOI: 10.1016/j.neuroimage.2007.04.042. URL: http://www.sciencedirect.com/science/article/pii/S1053811907003837.

[234] Theodore D. Satterthwaite, Mark A. Elliott, et al. "An improved framework for confound regression and filtering for control of motion artifact in the preprocessing of resting-state functional connectivity data". In: *NeuroImage* 64.1 (2013), pp. 240–256. ISSN: 10538119. DOI: 10.1016/j.neuroimage.2012.08.052. URL: http://linkinghub.elsevier.com/retrieve/pii/S1053811912008609.

[235] Matthew C Mauck, Jeffrey Lotz, et al. "The back pain consortium (BACPAC) research program: structure, research priorities, and methods". In: *Pain Medicine* 24.Supplement_1 (2023), S3–S12.

[236] Bruce Fischl. "FreeSurfer". In: *Neuroimage* 62.2 (2012), pp. 774–781.

[237] Madeline Hess, Brett Allaire, et al. "Deep learning for multi-tissue segmentation and fully automatic personalized biomechanical models from BACPAC clinical lumbar spine MRI". In: *Pain Medicine* 24.Supplement_1 (2023), S139–S148.

[238] U. U. Bharadwaj, A. R. Ben-Natan, et al. "Evaluation of 2 Novel Ratio-Based Metrics for Lumbar Spinal Stenosis". In: *American Journal of Neuroradiology* 43.10 (2022), pp. 1530–1538.

[239] U.U. Bharadwaj et al. "Deep learning for automated, interpretable classification of lumbar spinal stenosis and facet arthropathy from axial MRI". In: *European Radiology* (2023). In review.

[240] Oscar Esteban, Christopher J Markiewicz, et al. "fMRIPrep: a robust preprocessing pipeline for functional MRI". In: *Nature methods* 16.1 (2019), pp. 111–116.

[241] Marc Joliot, Gaël Jobard, et al. “AICHA: An atlas of intrinsic connectivity of homotopic areas”. In: *Journal of neuroscience methods* 254 (2015), pp. 46–59.

[242] Kavita Singh, María Guadalupe García-Gomar, et al. “Probabilistic atlas of the mesencephalic reticular formation, isthmic reticular formation, microcellular tegmental nucleus, ventral tegmental area nucleus complex, and caudal–rostral linear raphe nucleus complex in living humans from 7 Tesla magnetic resonance imaging”. In: *Brain Connectivity* 11.8 (2021), pp. 613–623.

Appendix A

Supplementary Information to Chapter 5

A.1 Application to early schizophrenia subjects

We investigated the structure-function model as a potential biomarker for schizophrenia by applying the gamma model to the functional data from schizophrenia subjects. The results we report in Figure A.1 yield from using the "optimal" structural connectome including both A and I with a weighting of 0.3. We found no significant differences between R score or model parameters between the healthy and schizophrenia subject groups. Mean R score for ESZ subjects is 0.41, and mean *gamma* value is 0.16. These results support the notion that the relationship between structural and functional eigenmodes is similar in both disease and healthy populations, as was previously reported in epilepsy subjects [144].

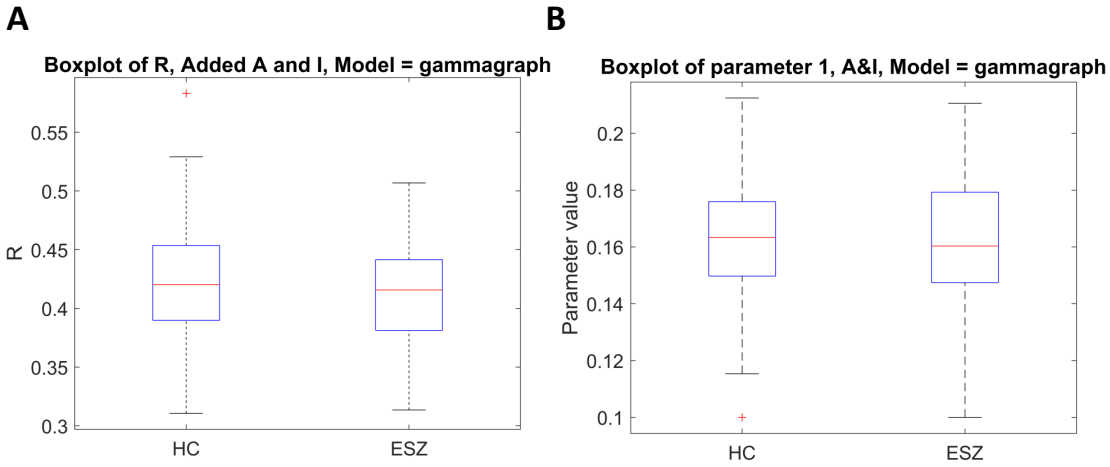

Figure A.1 Comparison of model performance for healthy controls and early schizophrenia subjects. No significant differences in model performance are shown. A) Boxplot of R between true and predicted FC. B) Boxplot of fitted model parameter.

A.2 Results from additional cohort

We repeated the analysis on an openly available data set comprised of structural and functional connectomes from 70 healthy subjects [225]. Two subjects were excluded due to data quality issues. These results can be found in Figures A.2 - A.6. These data only included the 68 cortical regions of the Desikan-Killiany atlas, allowing us to investigate if any of our results were driven by subcortical regions. Additionally, a structural connectome was provided for each subject, allowing us to investigate the differences in model performance when using subject-specific structural data. Both models performed similarly on these data, with a mean R of 0.28 for both across all subjects. The addition of both the adjacency and interhemispheric matrices provided an improvement in model performance, with the interhemispheric matrix addition having a more substantial impact. A notable difference is that, for this data, plots

of R vs weighting factor for the mean connectomes indicate a monotonic increase, with the optimal weights for both adjacency and interhemispheric matrix addition near 1.

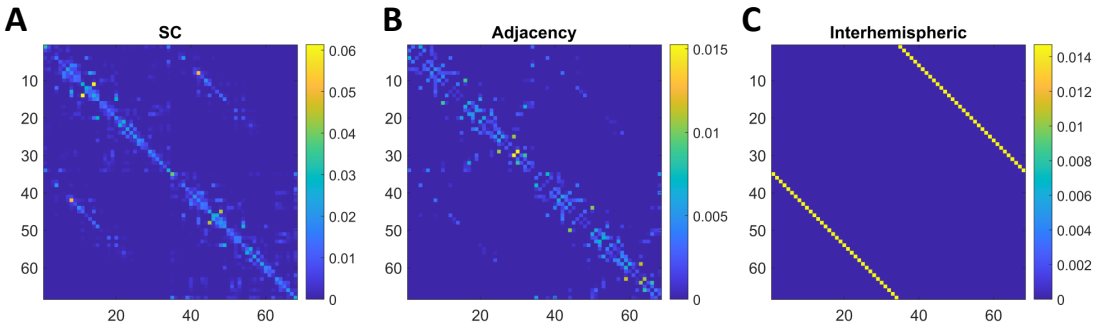

Figure A.2 Structural connectivity matrices for supplementary data using only cortical regions. A) Structural connectome derived from DTI. B) Adjacency matrix derived from the surface area of boundary between regions in brain atlas. C) Interhemispheric matrix representing connections between left and right homologous brain structures.

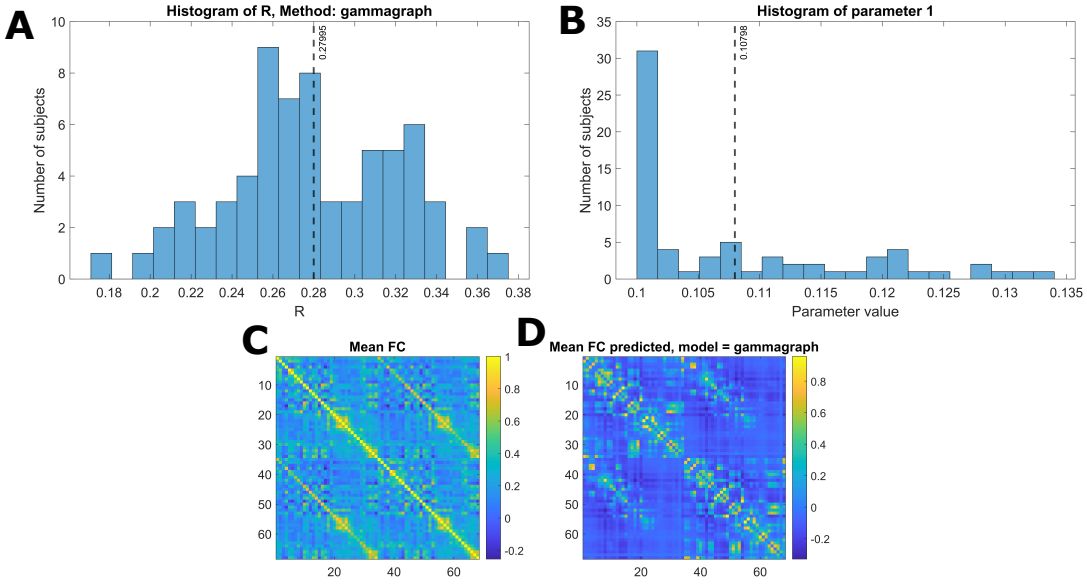

Figure A.3 Gamma model performance on supplementary data. A) Histogram of R score. B) Histogram of fitted parameter. C) Mean functional connectome over all subjects. D) Mean functional connectome predicted by model

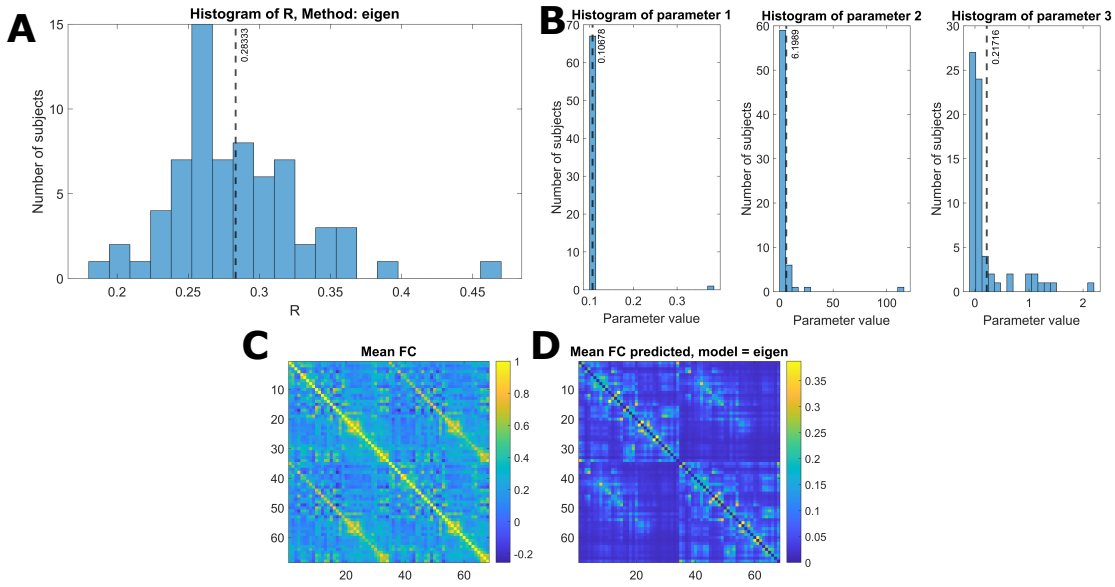

Figure A.4 Eigen model performance on supplementary data. A) Histogram of R score. B) Histogram of fitted parameter. C) Mean functional connectome over all subjects. D) Mean functional connectome predicted by model

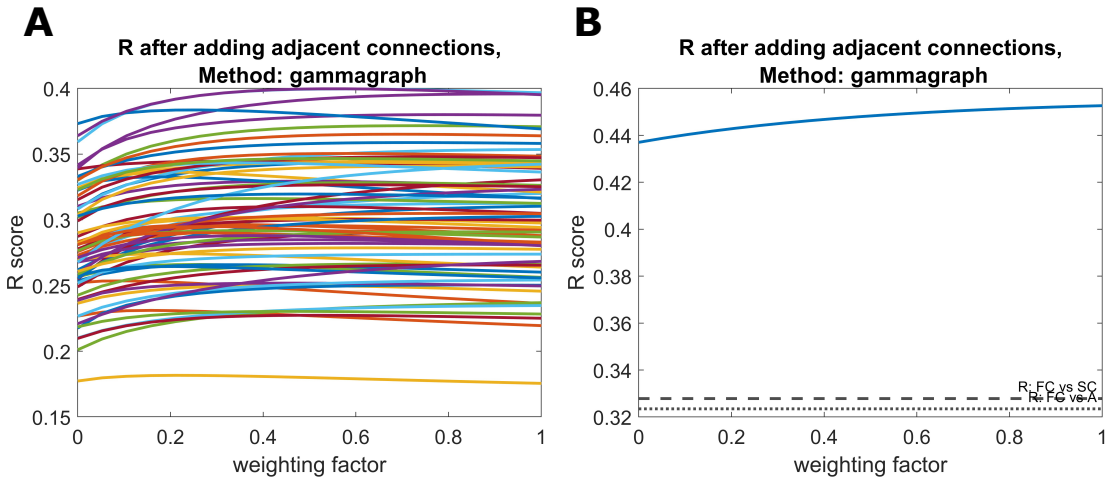

Figure A.5 Results of adding adjacency to supplementary data. A) R vs weighting factor for individual subjects. B) R vs weighting factor for mean structural and functional connectomes.

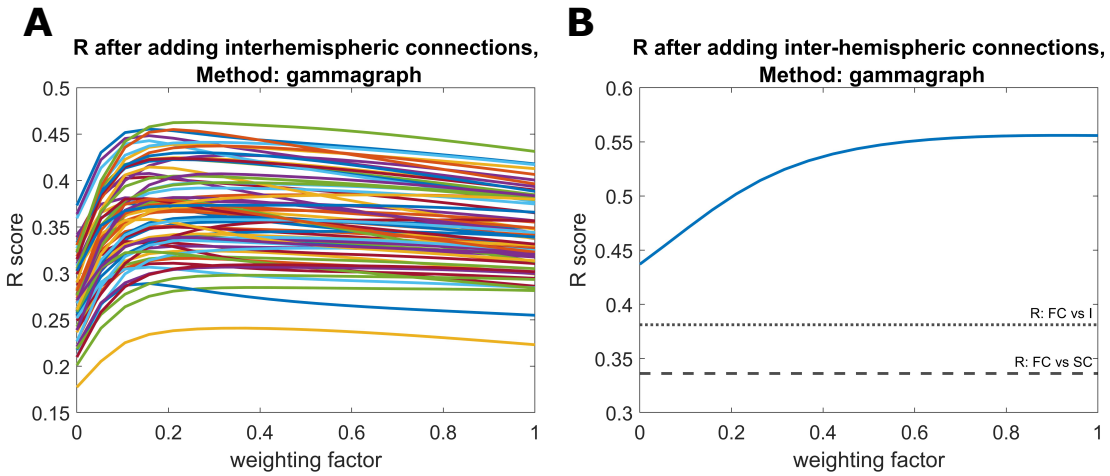

Figure A.6 Results of adding interhemispheric matrix to supplementary data. A) R vs weighting factor for individual subjects. B) R vs weighting factor for mean structural and functional connectomes.

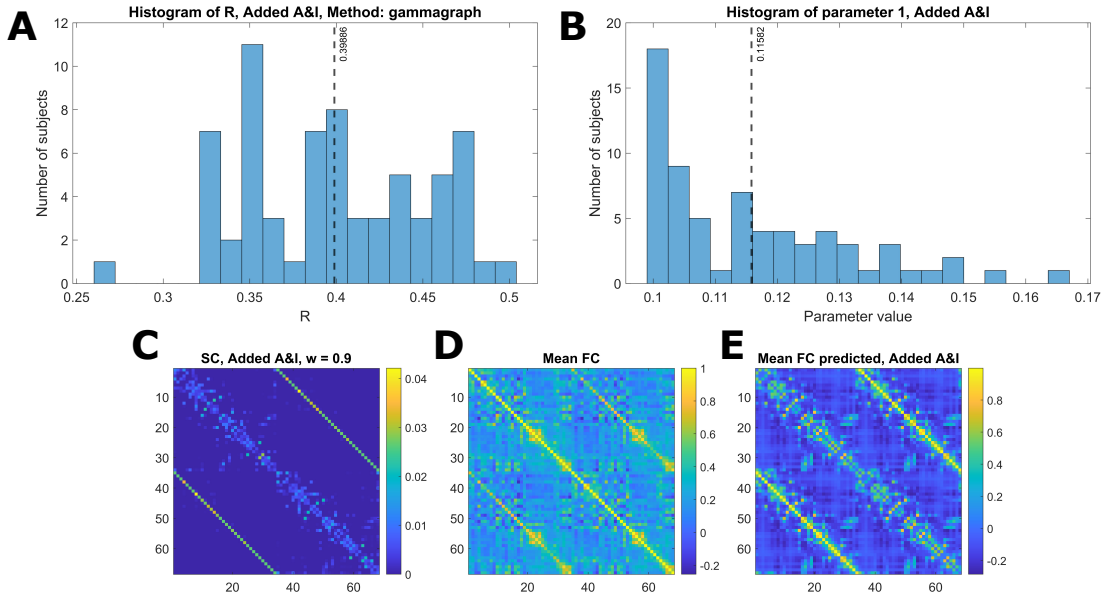

Figure A.7 Optimized model on supplementary data. Performance when using optimal structural connectome comprised of original SC, adjacency matrix, and interhemispheric matrix. A) Histogram of R scores. B) Histogram of fitted parameter. C) Optimal structural connectome. D) Mean functional connectome across healthy subjects.

A.3 Investigation of Gamma Model Parameters

We provide rationale for model parameter choices by repeating our analysis while varying the gamma shape parameter k A.8 and the regularization parameter ϵ A.9. Changing both values has little impact on model performance.

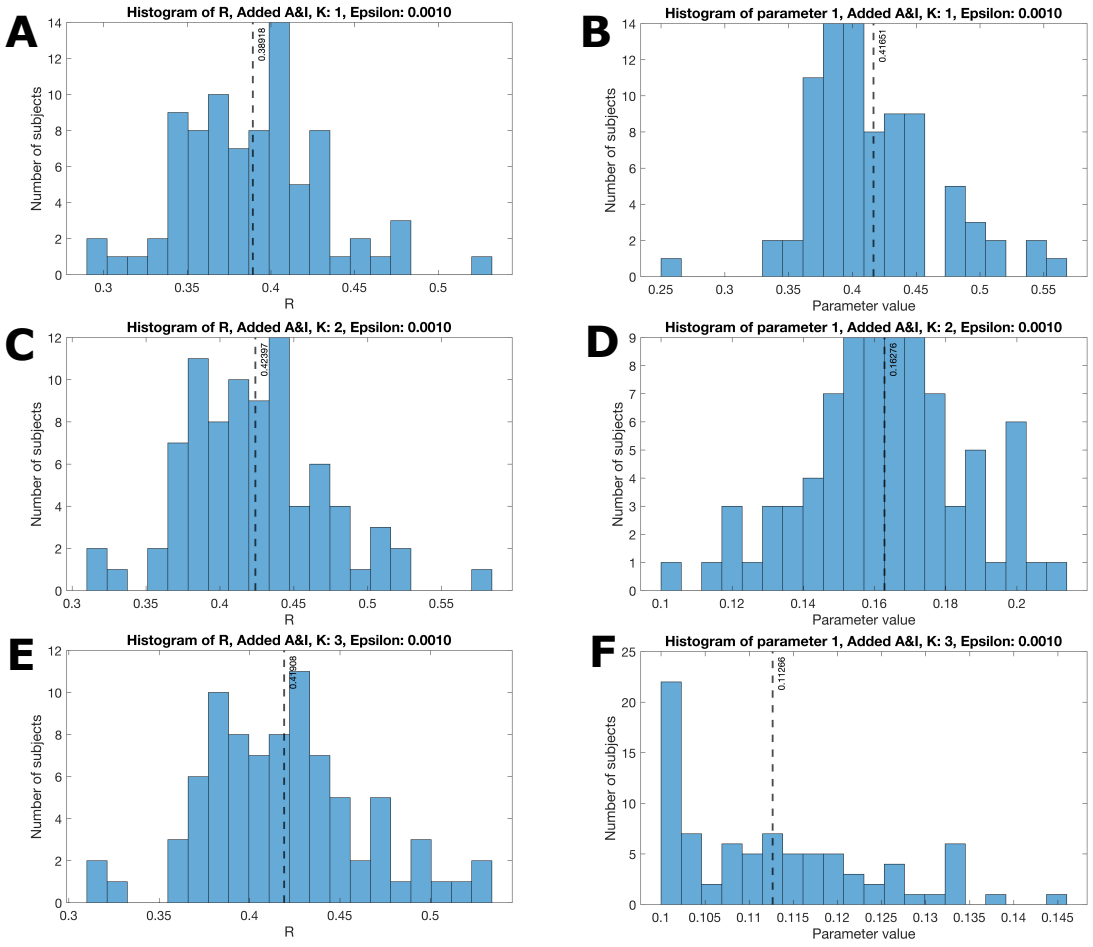

Figure A.8 Histograms of R and fitted parameter for gamma shape parameter. A,B) k=1. C,D) k=2. E,F) k=3

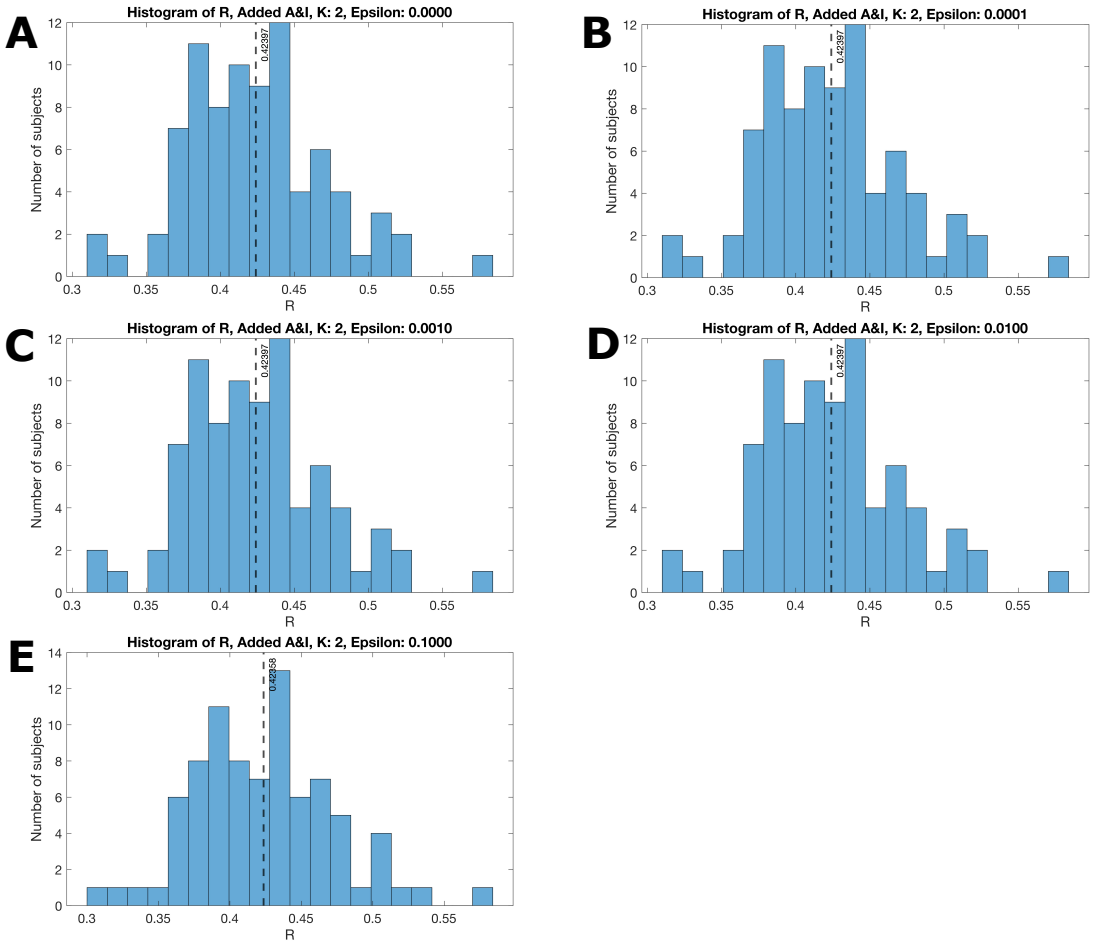

Figure A.9 Histograms of R over range of regularization parameters. A) ϵ=0. B) ϵ=0.0001. C) ϵ=0.001. D) ϵ=0.01. E) ϵ=0.1

A.4 Robustness to Noise

We investigated the impact of noise on model performance by applying the gamma model to mean FC and SC after adding varying levels of random noise to the SC A.10. Noise was added at a range of signal-to-noise ratios (SNR) between 0.01 to 100, and the analysis was repeated 100 times. We show stable model performance at an R of 0.47 above an SNR value of 1. At the lowest SNR of 0.01, we show a mean R value of 0.31 +/- 0.0079.

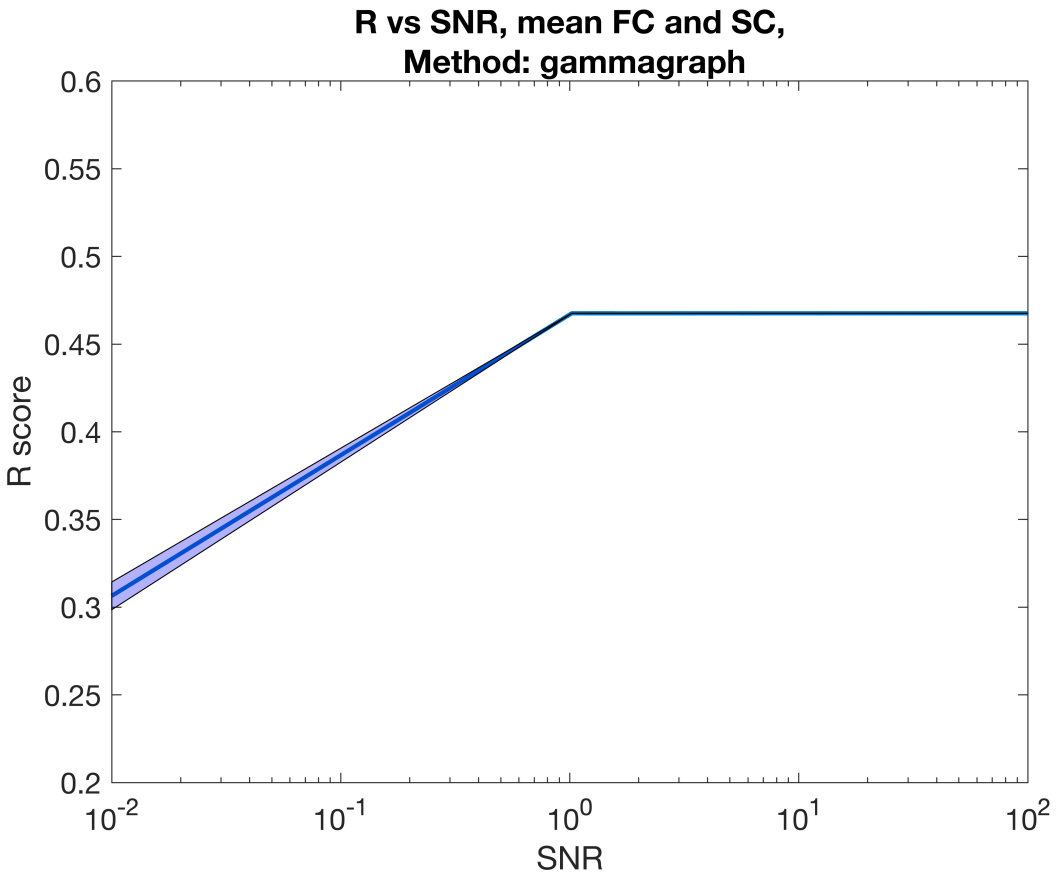

Figure A.10 Robustness to noise. A) R score vs. signal-to-noise ratio when applying gamma model to mean FC and SC while adding various levels of random noise to mean SC. The shaded region represents the 95% confidence interval after 100 repetitions.

A.5 Impact of Connectome Resolution

We investigated the impact of matrix resolution by repeating our analyses on reformatted versions of the supplemental dataset described above. These data are available in five different parcellation scales by subdividing the regions defined by the Desikan atlas into smaller equally-spaced subregions, as described in [226]. We report the results of these studies in Figures A.11 - A.14 for two different matrix sizes, one with 219 regions and one with 1000 regions. We were not able to generate adjacency matrices for these data, but we do

not consider this a large pitfall considering the modest effect of adjacency matrix addition demonstrated in other experiments. Model performance is slightly lower for 219 regions than for the original 68, and lower still for 1000-node connectomes. We hypothesize that smaller parcels introduce noise and other errors in the connectomes, which may explain why poorer fits were observed. The addition of interhemispheric connections improved model fits at both resolutions.

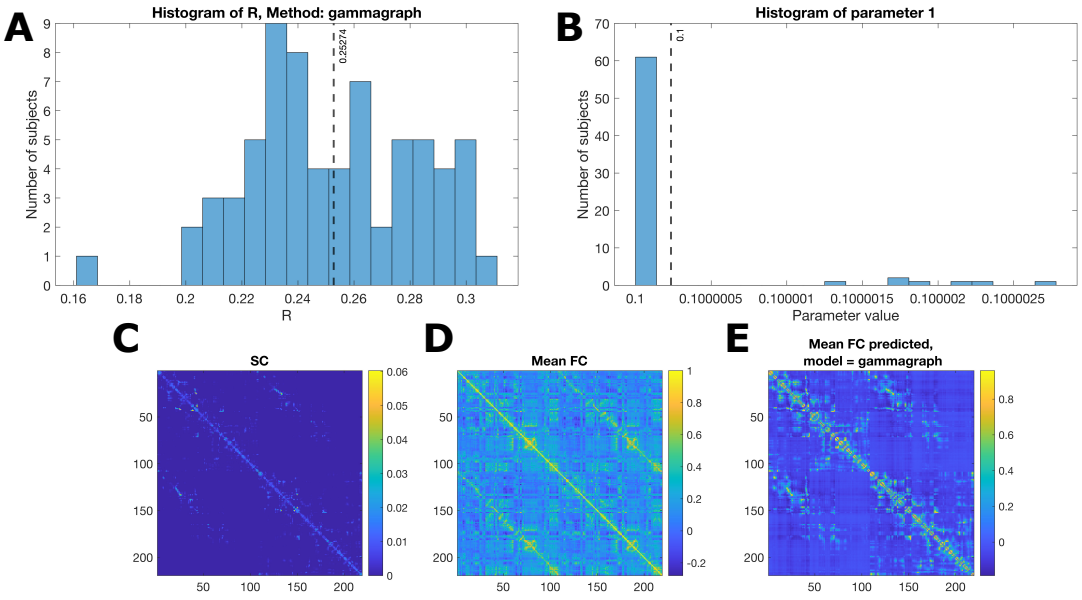

Figure A.11 Gamma model at medium resolution. Performance on supplementary data with 219 brain regions. A) Histogram of R score. B) Histogram of fitted parameters. C) Mean structural connectome. D) Mean functional connectome over all subjects. E) Mean functional connectome predicted by model

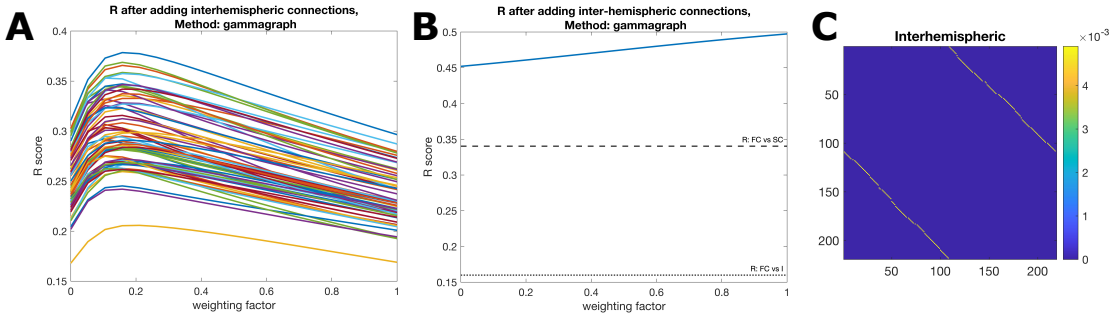

Figure A.12 Impact of interhemispheric connections at medium resolution. A) R vs weighting factor for individual subjects. B) R vs weighting factor for mean structural and functional connectomes. C) Interhemispheric matrix.

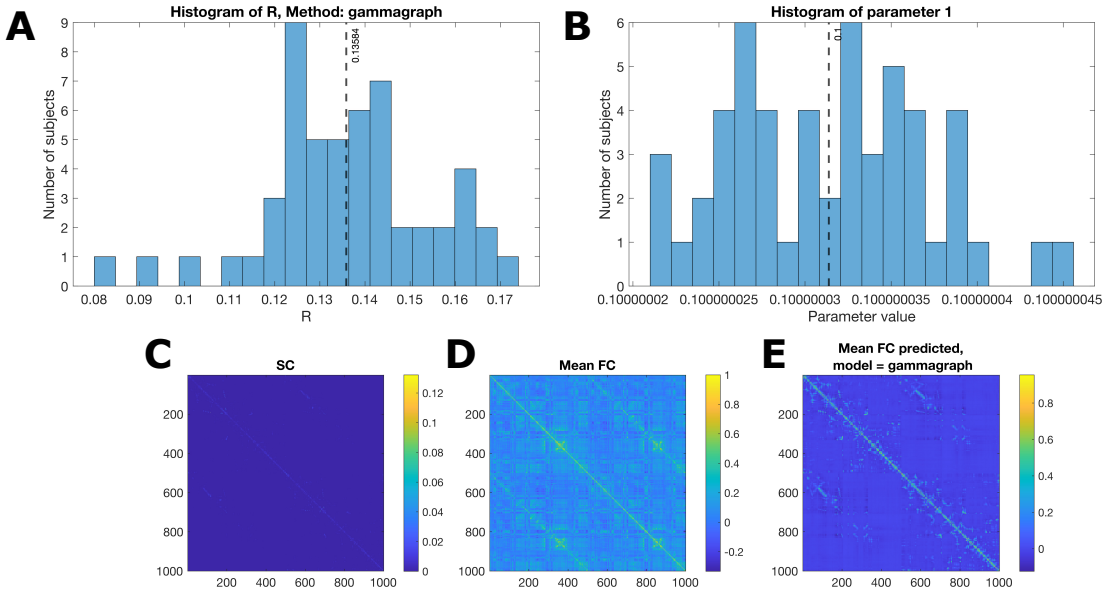

Figure A.13 Gamma model at high resolution. Performance on supplementary data with 1000 brain regions. A) Histogram of R score. B) Histogram of fitted parameters. C) Mean structural connectome. D) Mean functional connectome over all subjects. E) Mean functional connectome predicted by model

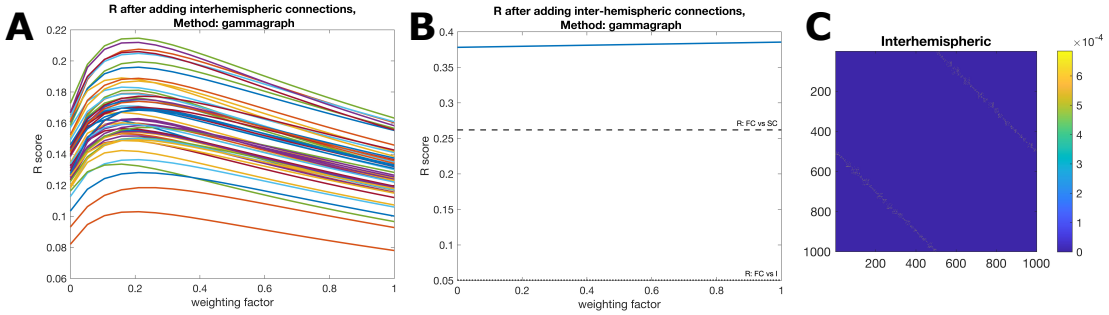

Figure A.14 Impact of interhemispheric connections at high resolution. A) R vs weighting factor for individual subjects. B) R vs weighting factor for mean structural and functional connectomes. C) Interhemispheric matrix.

Appendix B

Supplementary Information to Chapter 6

B.1 Body map dimensionality reduction

Community detection applied to the weighted covariance matrix of gridded pixel count data yielded a solution of 10 communities corresponding to distinct body parts, with an optimized weighting factor $\alpha = 0.90$ and a peak modularity = 0.71. These body parts are illustrated in Figure 6.1. Five of these communities encompassed grid sections from both the front and back body maps (head, left arm, right arm, left leg, and right leg) while five were restricted to either the front body (front chest, front pelvis) or back body (upper back, mid back, low back).

For each sensation, the mean normalized pixel count was calculated across all sections within each body part, yielding a vector of size 30 (number of sensations x number of body parts) for each subject. This matrix was then used as input to the NMF algorithm. The optimal number of factors was empirically selected to be 7 and confirmed with visual inspection of the cross-validation error curve. The resulting patterns are represented in

Figure 6.1 of the main text.

The NMF reconstruction explained 79.60% of the variance of the input data. Pattern 1 explained a majority of the variance (29.25%) and represents low back pain predominantly (88.37% feature weight) with some front pelvis pain (7.53%). All other patterns each contributed an additional 6 to 12% variance. Pattern 2 represents upper body pain, mostly upper back pain (58.22%) as well as some right arm pain (11.48%) and head pain (10.39%). Pattern 3 broadly represents arm symptoms, including left arm pain (22.05%), numbness (14.15%), and pins and needles (5.70%) as well as right arm numbness (11.34%) and pain (8.05%). Pattern 4 encompasses leg symptoms, including right leg pain (34.47%); pins and needles (9.11%) and left leg pain (22.17%); pins and needles (6.69%) as well as some front pelvis pain (8.60%) and right arm pain (5.56%). Pattern 5 is predominantly mid back pain (75.63%). Pattern 6 represents numbness and pins and needles throughout the back, with weights as follows: low back pins and needles (34.75%), low back numbness (21.92%), mid back numbness (6.75%), upper back pins and needles (5.16%), front pelvis pain (5.03%). Finally, Pattern 7 represents more leg symptoms, including left leg numbness (32.15%), pins and needles (10.61%) and pain (5.65%), and right leg numbness (25.13%) and pins and needles (5.26%).

B.2 Permutation test for significance

Following the initial grid search, a 7-component solution was selected for further analysis, with an optimized $N_{CC} = 7$ in 40% of the grid search iterations. All 7 dimensions were significant in held-out test sets compared to shuffled data (Component 1: Mean $r = 0.19$,

p = 3.29e-110; Component 2: Mean $r = 0.41$, $p = 0$; Component 3: Mean $r = 0.28$, p = 2.31e-215; Component 4: Mean $r = 0.12$, p = 4.84e-48; Component 5: Mean $r = 0.13$, p = 2.83e-47; Component 6: Mean $r = 0.24$, p = 4.17e-145; Component 7: Mean $r = 0.19$, p = 4.49e-95). Violin plots showing true and null correlations are presented in Figure B.1.

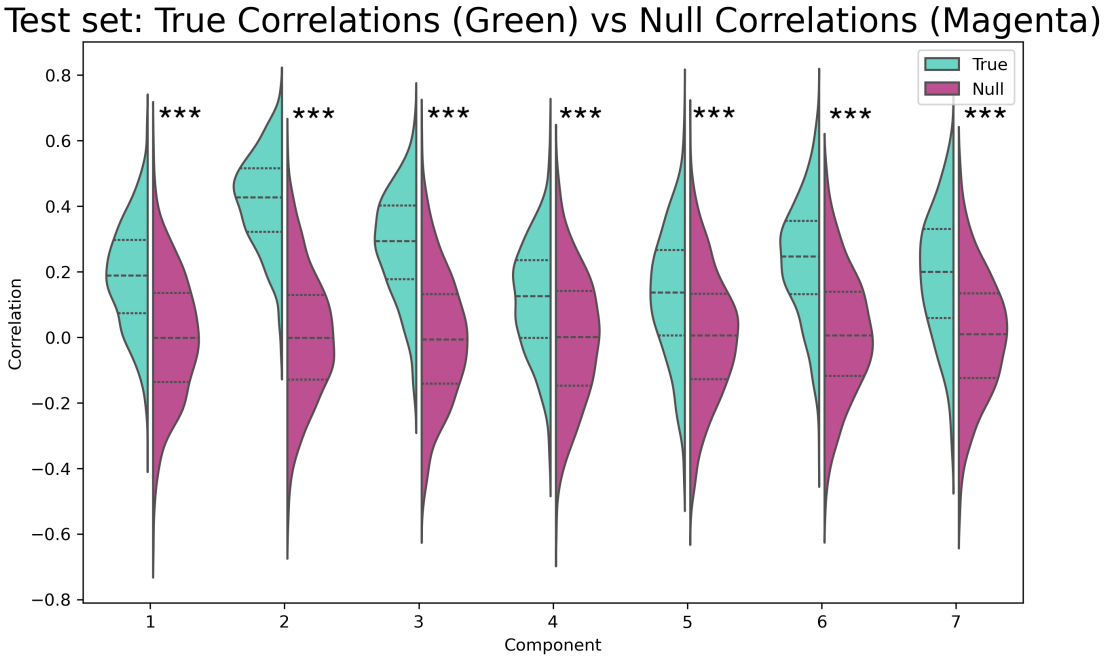

Figure B.1 Correlation of CCA components in true data vs. permuted data.

B.3 Additional Canonical Component Weights

Phenotype 3A (Figure B.2) represents low back symptoms, with low back pain, numbness, and pins and needles all negatively correlated with this component. This phenotype shows stronger connectivity between the amygdala and parahippocampal gyrus, and weaker cortico-cortical connectivity between regions throughout the frontal, parietal, occipital, and cingulate cortices and the insula, as well as between the basal ganglia and the cingulate.

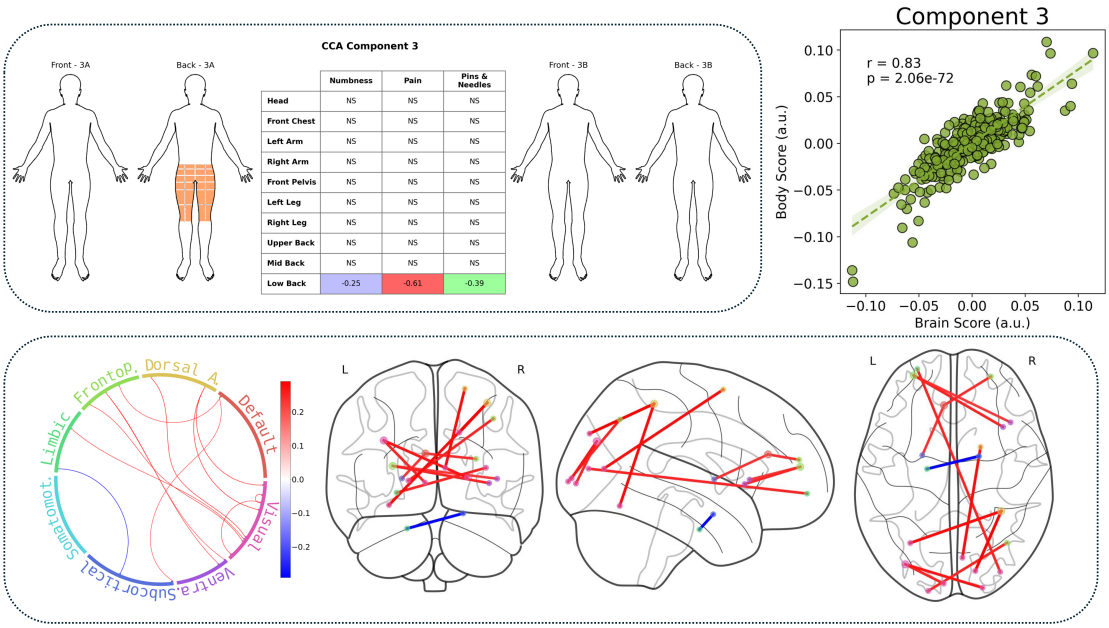

Figure B.2 Component 3.

The fourth dimension (Figure B.3) represents a superior-inferior gradient, with phenotype 4A showing upper body symptoms, including pain and numbness in the arms and upper to mid back, and 4B showing low body symptoms, such as low back pain and leg numbness and pins and needles. Phenotype 4A is associated with stronger connectivity between somatomotor regions, including S1, and DMN, attention, and limbic regions throughout the cortex. Phenotype 4B shows stronger connectivity between the thalamus and superior frontal gyrus.

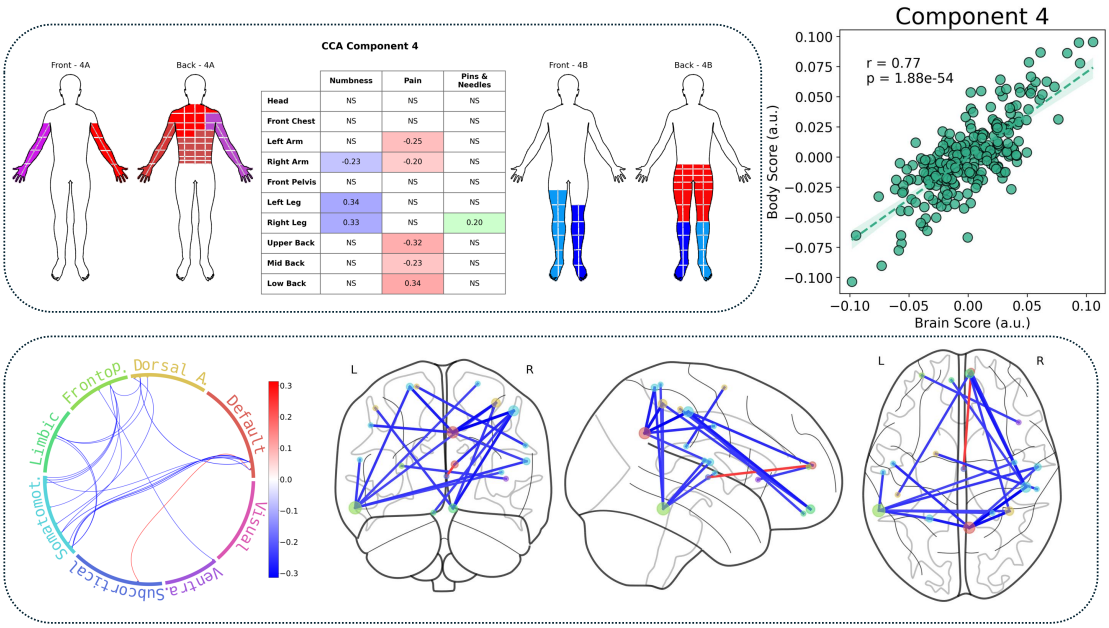

Figure B.3 Component 4.

Phenotype 5A is associated with pain in the legs and pelvis, while 5B involves pain in the upper left back and numbness in the left leg (Figure B.4). Phenotype 5A shows stronger connectivity within and between various somatomotor, attention, and default regions, as well as between the thalamus and parts of the occipital cortex. Phenotype 5B shows stronger interhemispheric connectivity in the superior temporal gyrus.

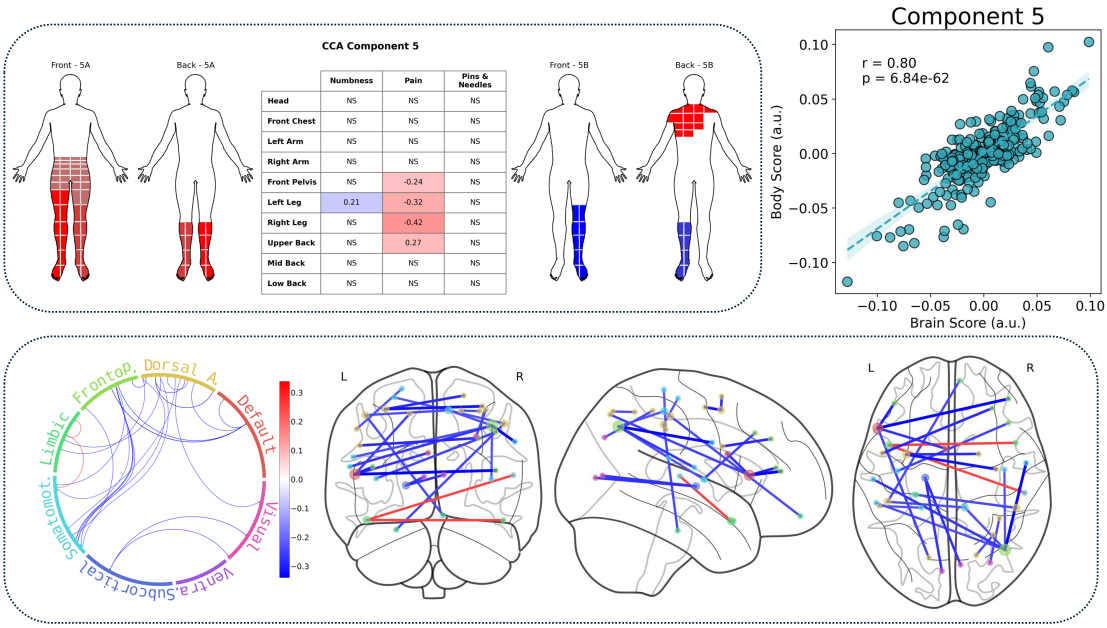

Figure B.4 Component 5.

Phenotype 6A is associated with low back pain, while 6B shows pins and needles in the upper and lower back and pain in the mid back (Figure B.5). Phenotype 6A shows stronger connectivity between visual regions, in particular the left and right lateral occipital cortex, as well as the cingulate and precuneus. Phenotype 6B shows stronger connectivity between the superior parietal lobule and parts of the lateral occipital cortex.

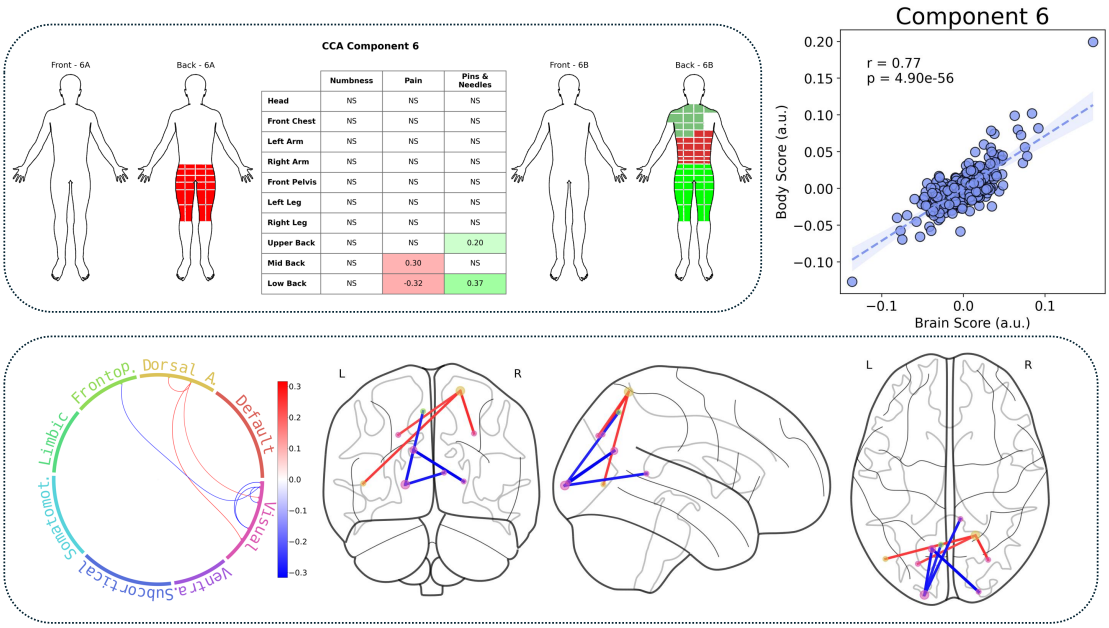

Figure B.5 Component 6.

Component 7 shows upper back pain on one end and mid back pain on the other. Phenotype 7B, the mid back pain phenotype, shows stronger connectivity between the left inferior frontal gyrus and the left insula, cingulate, and parahippocampal gyrus, as well as within the right parahippocampal gyrus.

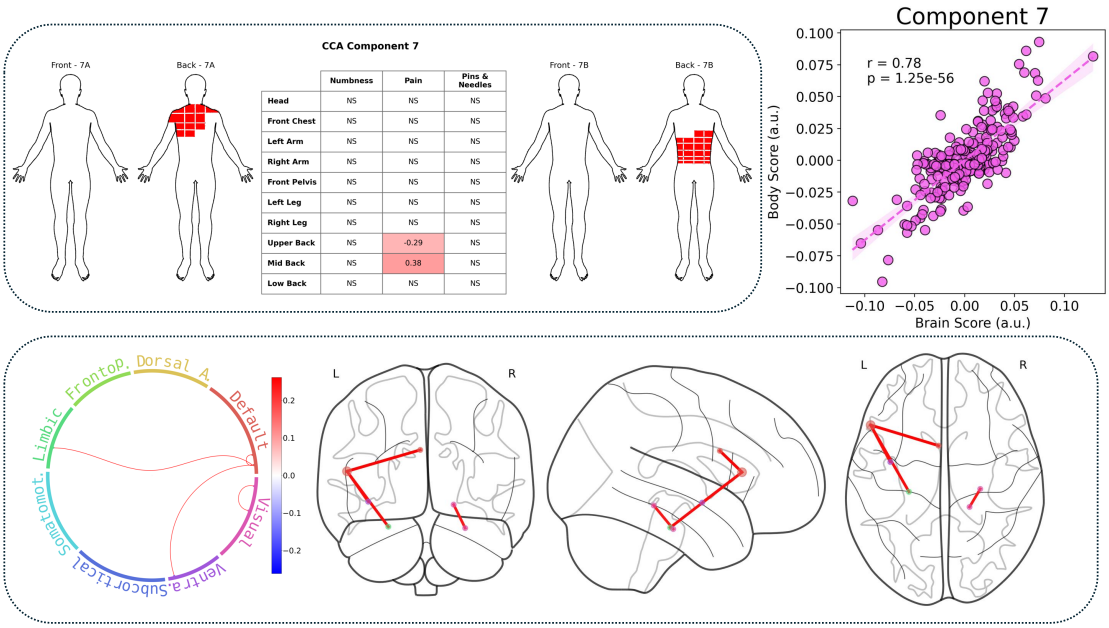

Figure B.6 Component 7.

B.4 Association with biopsychosocial factors

We investigated associations between each component score and a set of biopsychosocial risk and prognostic factors for LBP. Results are shown in Figures B.7 - B.9. Each column represents a component, and each row is a variable. Tests with $p \leq 0.05$ are indicated in the subplot title.

Component 1 is associated with almost all PROMIS variables with the exception of depression, suggesting that a tendency to report more bodily symptoms is also correlated with higher scores on negatively valanced PROMIS indicators (anxiety, fatigue, sleep disturbance) and lower scores on positively valanced PROMIS indicators (social roles and activities, cognitive function, physical function). Phenotype 1A is also associated with a higher PEG score and a higher prevalence of Modic Type 1 imaging findings. Component 2 showed an association with sex, with females tending more toward Phenotype 2B. Phenotype 3A is correlated with lower age and a higher score on the PROMIS fatigue scale. Component 7 is associated with several demographic factors, with Phenotype 7B correlated with female sex, higher BMI, and lower age. It is also associated with higher rates of social activity.

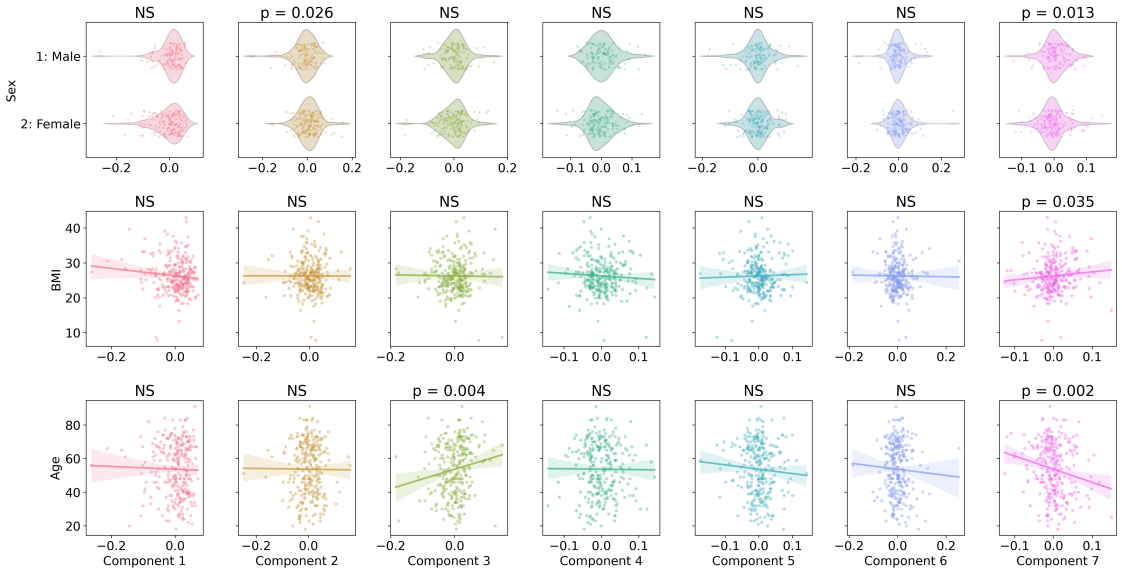

Figure B.7 Demographic Variables.

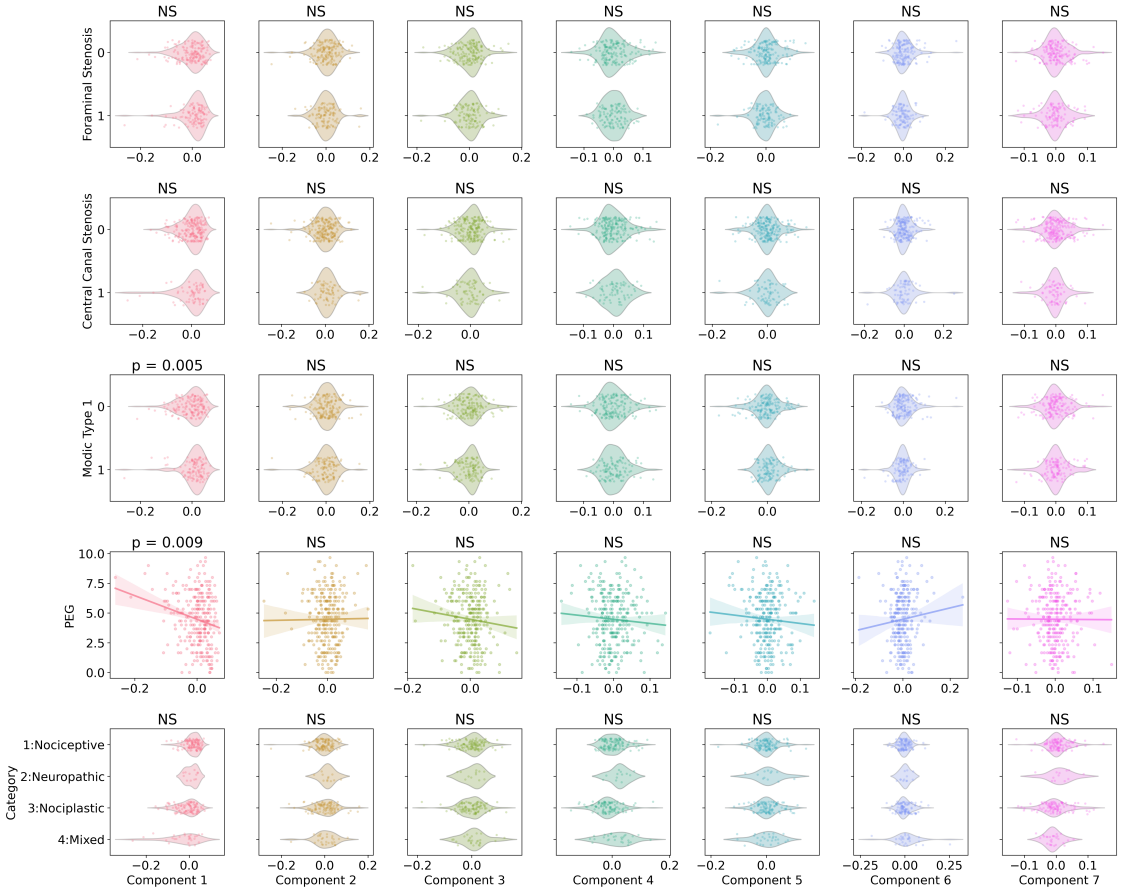

Figure B.8 Clinical Variables.

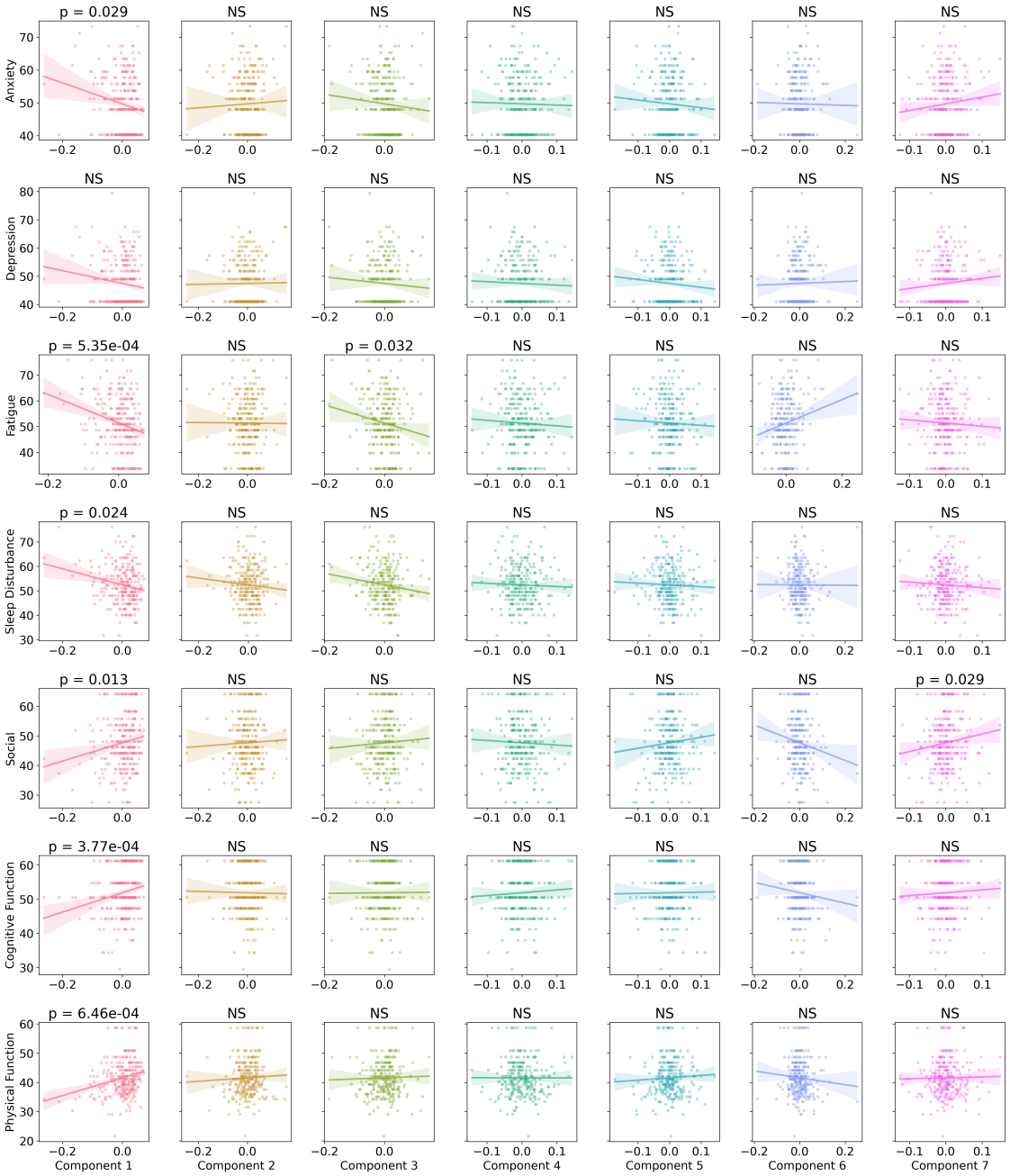

Figure B.9 Psychosocial Variables

Anxiety: PROMIS Anxiety 4a (higher = more anxiety); Depression: PROMIS Depression 4a (higher = more depressed); Fatigue: PROMIS Fatigue 4a (higher = more fatigued); Sleep Disturbance: PROMIS Sleep Disturbance (higher = more disturbance); Social: PROMIS Social Roles and Activities 4a (higher = more social); Cognitive Function: PROMIS Cognitive Function 2a (higher = more cognitive function), Physical Function: PROMIS Physical Function 6b (higher = more function).

B.5 fMRIPrep boilerplate text

Results included in this manuscript come from preprocessing performed using *fMRIPrep* 20.2.7 ([86]; [87]; RRID:SCR_016216), which is based on *Nipype* 1.7.0 ([131]; [132]; RRID:SCR_002502).

B.5.1 Anatomical data preprocessing

A total of 1 T1-weighted (T1w) images were found within the input BIDS dataset. The T1-weighted (T1w) image was corrected for intensity non-uniformity (INU) with `N4BiasFieldCorrection` [127], distributed with ANTs 2.3.3 [128, RRID:SCR_004757], and used as T1w-reference throughout the workflow. The T1w-reference was then skull-stripped with a *Nipype* implementation of the `antsBrainExtraction.sh` workflow (from ANTs), using OASIS30ANTs as target template. Brain tissue segmentation of cerebrospinal fluid (CSF), white-matter (WM) and gray-matter (GM) was performed on the brain-extracted T1w using `fast` [FSL 5.0.9, RRID:SCR_002823, 129]. Brain surfaces were reconstructed using `recon-all` [FreeSurfer 6.0.1, RRID:SCR_001847, 227], and the brain mask estimated previously was refined with a custom variation of the method to reconcile ANTs-derived and FreeSurfer-derived segmentations of the cortical gray-matter of Mindboggle [RRID:SCR_002438, 228]. Volume-based spatial normalization to two standard spaces (MNI152NLin2009cAsym, MNI152NLin6Asym) was performed through nonlinear registration with `antsRegistration` (ANTs 2.3.3), using brain-extracted versions of both T1w reference and the T1w template. The following templates were selected for spatial normalization: *ICBM 152 Nonlinear Asymmetrical template version 2009c* [130], RRID:SCR_008796; TemplateFlow ID: MNI152NLin2009cAsym, *FSL's MNI ICBM 152 non-linear 6th Generation Asymmetric Average Brain Stereotaxic*

Registration Model [229], RRID:SCR_002823; TemplateFlow ID: MNI152NLin6Asym.

B.5.2 Functional data preprocessing

For each of the 1 BOLD runs found per subject (across all tasks and sessions), the following preprocessing was performed. First, a reference volume and its skull-stripped version were generated by aligning and averaging 1 single-band references (SBRefs). A deformation field to correct for susceptibility distortions was estimated based on *fMRIPrep*'s *fieldmap-less* approach. The deformation field is that resulting from co-registering the BOLD reference to the same-subject T1w-reference with its intensity inverted [230, 231]. Registration is performed with `antsRegistration` (ANTs 2.3.3), and the process regularized by constraining deformation to be nonzero only along the phase-encoding direction, and modulated with an average fieldmap template [232]. Based on the estimated susceptibility distortion, a corrected EPI (echo-planar imaging) reference was calculated for a more accurate co-registration with the anatomical reference. The BOLD reference was then co-registered to the T1w reference using `bbregister` (FreeSurfer) which implements boundary-based registration [134]. Co-registration was configured with nine degrees of freedom to account for distortions remaining in the BOLD reference. Head-motion parameters with respect to the BOLD reference (transformation matrices, and six corresponding rotation and translation parameters) are estimated before any spatiotemporal filtering using `mcflirt` [FSL 5.0.9, 135]. BOLD runs were slice-time corrected to 0.351s (0.5 of slice acquisition range 0s-0.703s) using `3dTshift` from AFNI 20160207 [136, RRID:SCR_005927]. First, a reference volume and its skull-stripped version were generated using a custom methodology of *fMRIPrep*. The BOLD time-series

(including slice-timing correction when applied) were resampled onto their original, native space by applying a single, composite transform to correct for head-motion and susceptibility distortions. These resampled BOLD time-series will be referred to as *preprocessed BOLD in original space*, or just *preprocessed BOLD*. The BOLD time-series were resampled into several standard spaces, correspondingly generating the following *spatially-normalized, preprocessed BOLD runs*: MNI152NLin2009cAsym, MNI152NLin6Asym. First, a reference volume and its skull-stripped version were generated using a custom methodology of *fMRIPrep*. Automatic removal of motion artifacts using independent component analysis [ICA-AROMA, 137] was performed on the *preprocessed BOLD on MNI space* time-series after removal of non-steady state volumes and spatial smoothing with an isotropic, Gaussian kernel of 6mm FWHM (full-width half-maximum). Corresponding "non-aggresively" denoised runs were produced after such smoothing. Additionally, the "aggressive" noise-regressors were collected and placed in the corresponding confounds file. Several confounding time-series were calculated based on the *preprocessed BOLD*: framewise displacement (FD), DVARS and three region-wise global signals. FD was computed using two formulations following Power (absolute sum of relative motions, [138]) and Jenkinson (relative root mean square displacement between affines, [135]). FD and DVARS are calculated for each functional run, both using their implementations in *Nipype* [following the definitions by 138]. The three global signals are extracted within the CSF, the WM, and the whole-brain masks. Additionally, a set of physiological regressors were extracted to allow for component-based noise correction [*CompCor*, 233]. Principal components are estimated after high-pass filtering the *preprocessed BOLD* time-series (using a discrete cosine filter with 128s cut-off) for the two *CompCor* variants: temporal (tCompCor) and anatomical (aCompCor). tCompCor components are

then calculated from the top 2% variable voxels within the brain mask. For aCompCor, three probabilistic masks (CSF, WM and combined CSF+WM) are generated in anatomical space. The implementation differs from that of Behzadi et al. in that instead of eroding the masks by 2 pixels on BOLD space, the aCompCor masks are subtracted a mask of pixels that likely contain a volume fraction of GM. This mask is obtained by dilating a GM mask extracted from the FreeSurfer's *aseg* segmentation, and it ensures components are not extracted from voxels containing a minimal fraction of GM. Finally, these masks are resampled into BOLD space and binarized by thresholding at 0.99 (as in the original implementation). Components are also calculated separately within the WM and CSF masks. For each CompCor decomposition, the k components with the largest singular values are retained, such that the retained components' time series are sufficient to explain 50 percent of variance across the nuisance mask (CSF, WM, combined, or temporal). The remaining components are dropped from consideration. The head-motion estimates calculated in the correction step were also placed within the corresponding confounds file. The confound time series derived from head motion estimates and global signals were expanded with the inclusion of temporal derivatives and quadratic terms for each [234]. Frames that exceeded a threshold of 0.5 mm FD or 1.5 standardised DVARS were annotated as motion outliers. All resamplings can be performed with *a single interpolation step* by composing all the pertinent transformations (i.e. head-motion transform matrices, susceptibility distortion correction when available, and co-registrations to anatomical and output spaces). Gridded (volumetric) resamplings were performed using `antsApplyTransforms` (ANTs), configured with Lanczos interpolation to minimize the smoothing effects of other kernels [139]. Non-gridded (surface) resamplings were performed using `mri_vol2surf` (FreeSurfer).

Appendix C

Investigation of Image Quality Variation in Multisite MRI Dataset

The following is adapted from work that was previously shown as a conference presentation, appearing as:

Cummings, J., Jimmy, J., Harris, R., Ichesco, E., Kaplan, C., Torrisi, S., Vu, A., Wey, H.-Y., Yoo, C.-H., & Peltier, S. (2024). Image quality variation and cortical volume estimation in a multisite study of low back pain. In Proceedings of The Organization for Human Brain Mapping (OHBM) Conference, Seoul, Korea, June 2024.

C.1 Introduction

This study examines image quality variation in a multisite study of chronic low back pain (cLBP) collected as part of the Back Pain Consortium (BACPAC) Research Program [235]. We present preliminary results comparing image quality control (QC) metrics and morphometric measurements derived from structural MR images collected on 10 scanners within the

BACPAC network following protocol harmonization. These results show significant site differences, suggesting a need for further harmonization efforts when compiling multisite data for group analysis.

C.2 Methods

C.2.1 Study Design

To collect a large, diverse participant sample, the Brain Imaging Working Group developed a protocol aimed at standardizing neuroimaging acquisition parameters across the different hardware and software configurations at participating institutions. The scan protocol was adapted from the Alzheimer's Disease Neuroimaging Initiative (ADNI) protocol and outlined sequences for three magnetic resonance imaging (MRI) techniques: T1-weighted and T2-weighted structural imaging and functional MRI (fMRI) using single shot echo planar imaging (EPI). Data quality and consistency between scanners was also evaluated using phantom scans and the use of a "traveling participant" - a healthy volunteer scanned at all sites.

Neuroimaging was performed at six sites: University of California, San Francisco (UCSF); University of California, Davis (UCD); University of California, San Diego (UCSD); University of California, Irvine (UCI); University of Michigan (Michigan); Massachusetts General Hospital (MGH). Four sites (UCSF, UCD, UCSD, UM) used two different scanners; data from all scanners are reported here. All sites used 3T MR scanners produced by either Siemens or GE.

C.2.2 Overview of Participants

Participants were recruited as part of each institution's BACPAC study. Common inclusion criteria include the presence of low back pain, and exclusion criteria include contraindications for MR imaging, such as metal implants. Here we report results from the first 8-16 subjects per site. In addition, a traveling subject (healthy volunteer, male, age 28-29, BMI = 27.9) was scanned on at least one scanner at each site between July 2021 and September 2022.

C.2.3 Image Acquisition

Neuroimaging was performed on a total of 10 different scanners across 6 sites. Here we report results using T1-weighted images (MP-RAGE, TR/TE 2500/2.88 (Siemens), 2500/2 (GE); voxel size 1.0 mm isotropic; matrix 256x256; flip angle 8 deg) and T2-weighted images (MP-RAGE, TR/TE 3200/600; voxel size 1.0 mm isotropic; matrix 256x256). All sites used 3T MR Siemens or GE scanners.

C.2.4 Quality Control

Image quality metrics were extracted using MRIQC v23.1.0 [88]. Here we report a selection of summary metrics: the signal-to-noise ratio calculated within the tissue mask (SNR_Total); the signal-to-noise ratio calculated with the air background as reference (SNRD_Total); the contrast-to-noise ratio representing the separation of gray and white matter signals (CNR); the average full width at half maximum, a measure of image smoothness (FWHM_AVG); and a ratio of the SNR to FWHM (SNR/FWHM). All metrics and formulas are described in further detail in MRIQC's documentation.

C.2.5 Brain Volume Analysis

Brain volume measurements were derived from traveling subject data using Freesurfer v 1.201 [236]. Here we report total brain volume and insula volume, an ROI chosen for its importance in pain processing.

C.2.6 Statistical Analysis

One-way ANOVA was performed to test for site differences in each of the four QC metrics studied. Tests with a p-value less than 0.05 are reported.

C.3 Results

C.3.1 Traveling Subject

We first present a comparison of T1w and T2w anatomical images collected for the same traveling subject on 7 scanners, highlighting the evident signal variation (Figure C.1).

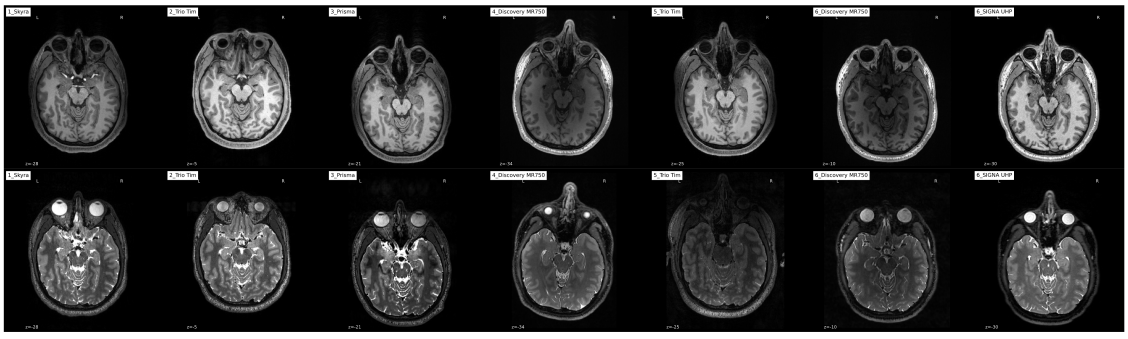

Figure C.1 T1w and T2w brain scans of traveling subject on 7 scanners.

As a means of quantifying this variation, we show brain volume measurements derived from these data in Figure C.2. Whole brain volume estimations for the traveling subject =

1289874.43 ± 13209.57 mm^3; Insula volume estimations = 7094.86 ± 271.21 mm^3.

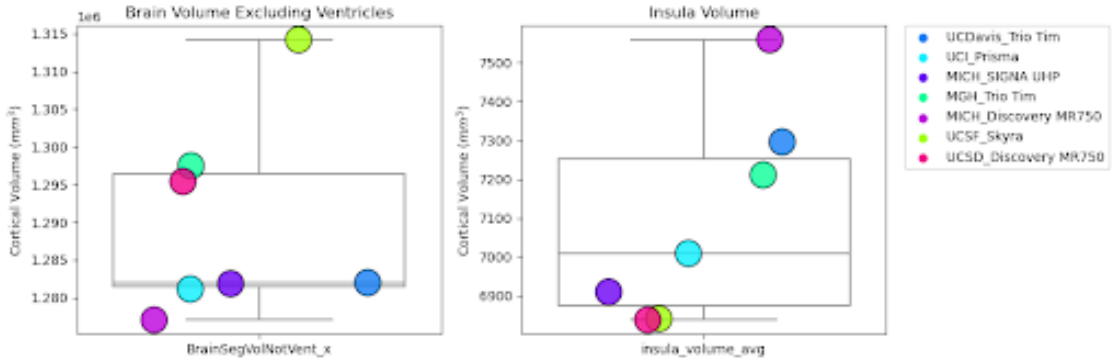

Figure C.2 Brain volume measurements derived from traveling subject data. Each point represents the same subject's acquisition at a different scanner and is colored according to the legend on the right, with Siemens models in shades of blue/green and GE in pink/purple. The first subplot shows the entire brain volume excluding ventricles, while the second shows Insula volume averaged between the left and right hemispheres.

We investigated whether any QC metrics could account for the large degree of variation in these measurements and found that differences in FWHM may play a role, as shown in Figure C.3

C.3.2 All subjects

Image quality metrics for all subject data are shown in Figure C.4. There is a statistically significant difference between the sites for all four QC metrics, as follows:

SNR_Total: F= 13.17, p-value= 6.13e-10, with an overall large effect (ω^2) = 0.36.

CNR: F= 11.22, p-value= 1.15e-8, with an overall large effect (ω^2)= 0.32.

FWHM_AVG: F= 13.00, p-value= 7.92e-10, with an overall large effect (ω^2) = 0.35.

SNR/FWHM: F= 7.05, p-value= 0.000010, with an overall large effect (ω^2) = 0.22.

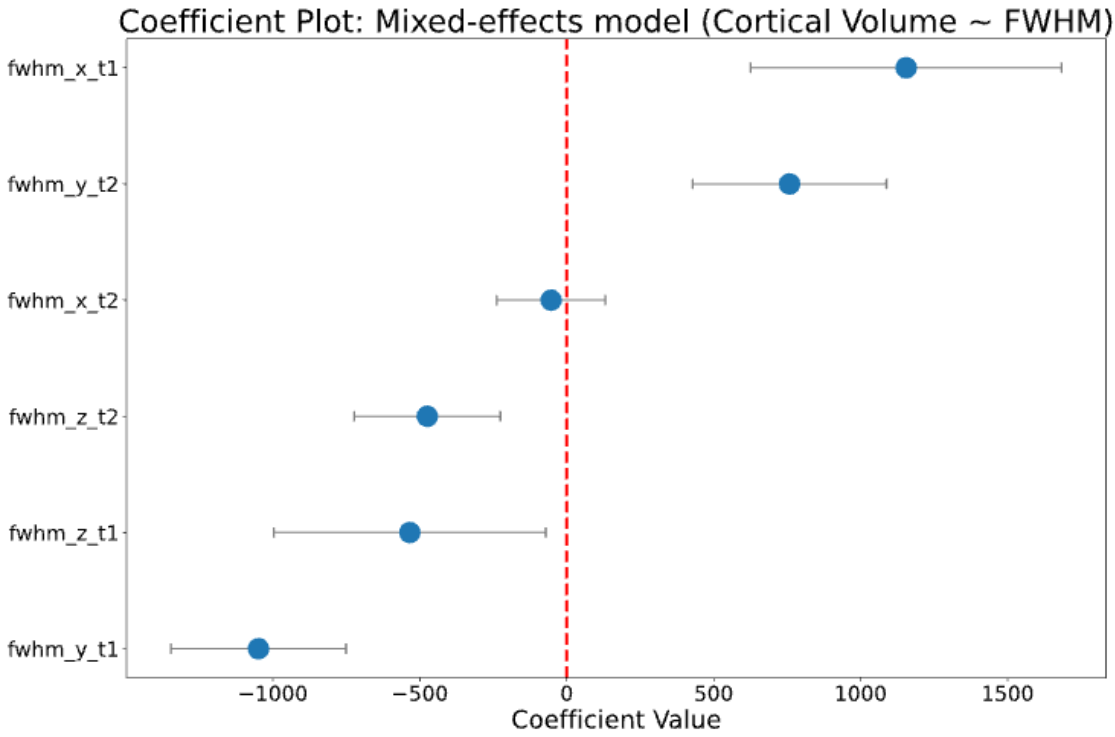

Figure C.3 Coefficient plot showing relationship between FWHM and cortical volume estimate variation.

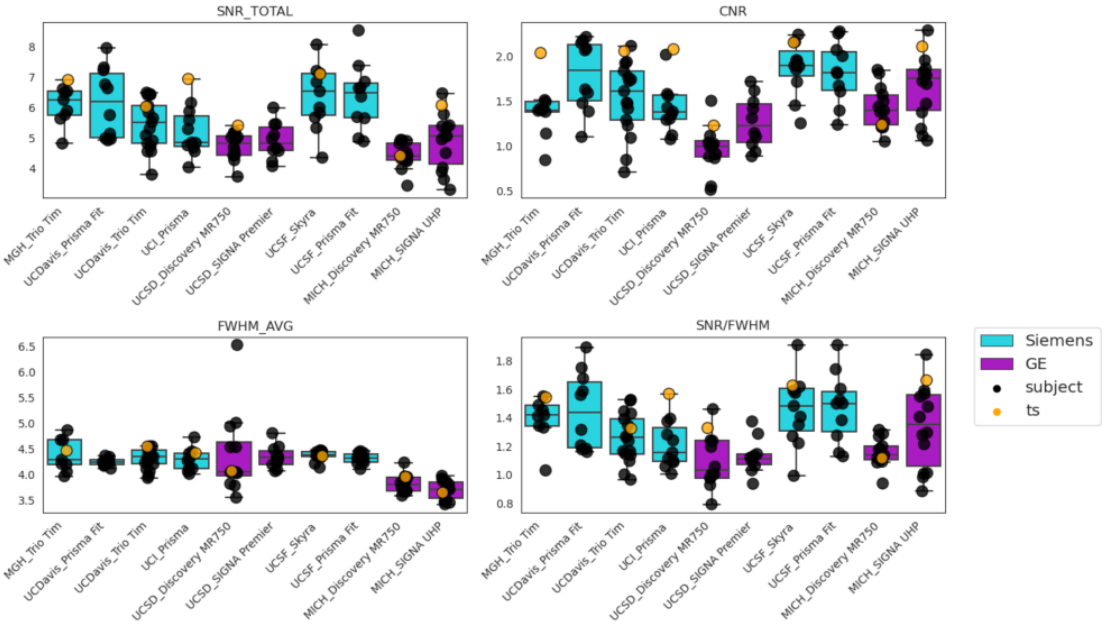

Figure C.4 Image quality metrics derived from participants' structural T1w images. Each subject is represented by a black point and where available, corresponding traveling subject data (ts) is represented in yellow. Boxes are colored according to the scanner manufacturer.

We further investigated the SNR of both anatomical sequences and found significant variation depending on sequence and estimation method, as shown in Figure C.5

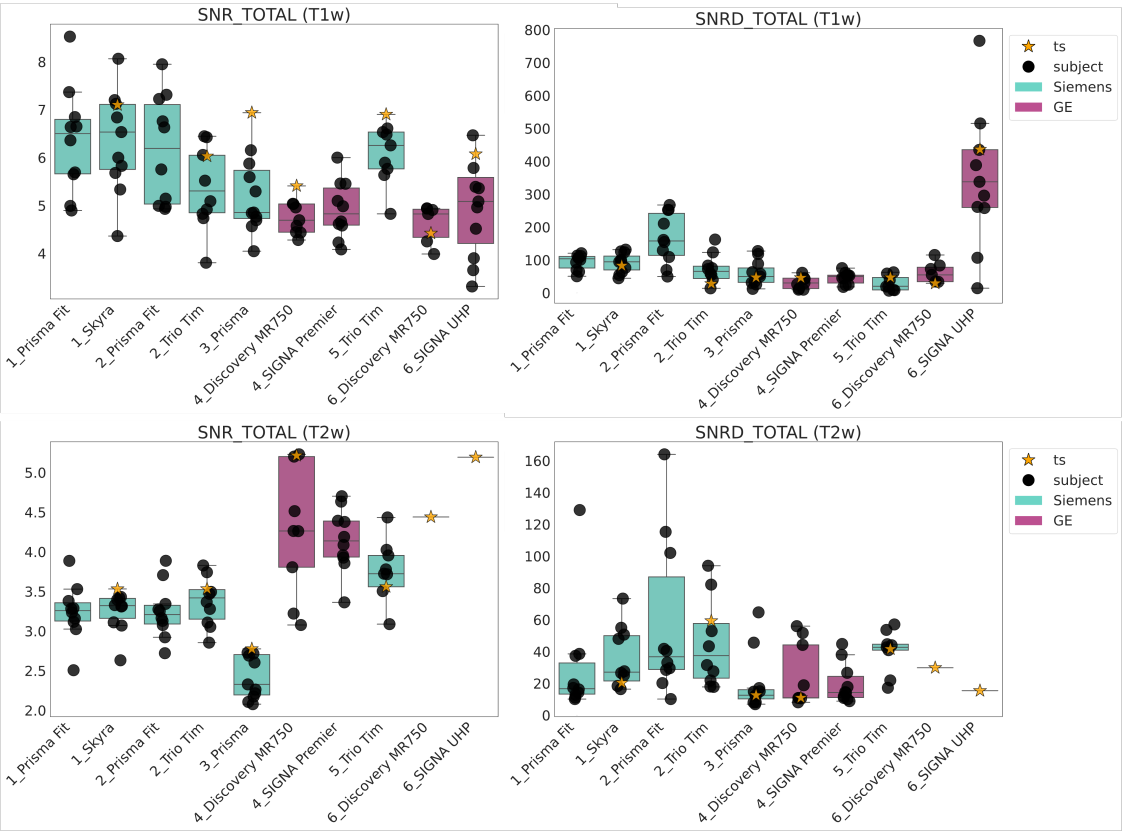

Figure C.5 SNR variation in T1w and T2w images.

C.4 Conclusions

We show that group level image quality measures vary significantly between sites despite harmonization of the imaging protocol. We also show variation of several hundred mm^3 in brain volume estimation on the traveling subject when scanned at different sites. Additionally, our results suggest that image quality, in particular FWHM, may have a sizable impact on derived measurements. This impact could be mediated through several mechanisms, including

blurring effects on tissue boundary detection, partial volume effects, or registration issues. Overall, these results highlight the importance of harmonization efforts at all stages of image acquisition and analysis. Future directions will include a deeper investigation into the causes of these variations, such as image artifacts, coil or software differences, as well as the impacts and considerations when pooling the data for analysis.

Appendix D

Associations Between Central Canal Stenosis, Resting State Functional Connectivity Networks, and Pain Perception in Chronic Lower Back Pain Patients

The following is adapted from work that was previously shown as a conference presentation, appearing as:

Cummings, J., Hess, M., Gao, K., Bharadwaj, U., Han, M., Chin, C., Torrisi, S., Townsend, J., Vu, A., Pedoia, V., & Majumdar, S. (2023). Associations between central canal stenosis, resting state functional connectivity networks, and pain perception in chronic lower back pain patients. In Proceedings of the 31 Annual Meeting of ISMRM, Toronto, Canada, June 2023

D.1 Introduction

Several factors make back pain particularly difficult to characterize, including the diversity of tissues implicated, lack of standardized quantification methods, and the inherent subjectivity of sensation. While brain fMRI holds the possibility of revealing the neural activity underlying pain sensation, a comprehensive understanding of pain must also take peripheral inputs into account. In this study, we present preliminary findings in a dataset combining brain and spine MRI from 30 subjects with chronic low back pain (cLBP). Leveraging recent developments in machine learning, we obtain a measure of central canal stenosis in the spine for each subject as well as functional connectivity in the brain during resting state fMRI. We present relationships between these spine and brain biomarkers with common pain metrics. In doing so, we take the first steps in establishing an imaging-based, multidimensional patient-specific model of pain.

D.2 Methods

D.2.1 Image Acquisition

Brain and spine images were collected for 30 cLBP patients (age = 50.1 $\pm$ 12.5, BMI = 27.1 $\pm$ 7.1, 23 Female (76.7 %)). Spine imaging protocol included sagittal and axial T1 and T2-weighted 2D fast spin-echo sequences. Neuroimaging protocol followed standards set by the Human Connectome Project and included 3D T1-weighted MP-RAGE and resting state fMRI using multiband echo planar imaging. Questionnaires to assess pain and functioning, including the Pain, Enjoyment of Life and General Activity scale (PEG), were also obtained.

D.2.2 Spine Image Processing

Automatic segmentation of the dural sac and intervertebral discs was performed using convolutional neural networks (CNN's) based on 2D V-Nets trained on axial T2-weighted images. Models have been previously published and performances are summarized in Figure D.1 [237]. Segmentation masks were used to calculate dural sac and disc cross-sectional area (CSA) at each axial slice. The ratio of the dural sac and disc CSA's (DDR) was used as input into a decision tree classifier trained to classify each axial slice with a grade of central canal stenosis (Normal, Mild, Moderate, Severe) based on using a method previously described [238, 239] (Figure D.2).

D.2.3 Neuroimaging Processing

Processing was performed using fMRIPrep 21.0.2 [240] and Nilearn [131]. Skull-stripped T1-weighted MP-RAGE images were used for brain tissue segmentation and registration into standard MNI space. Functional data processing included slice-timing correction, alignment to T1w images, removal of motion artifacts and basic CSF/white matter confounds, and band-pass filtering. Time series were extracted from cortical regions defined using the AICHA atlas [241] and a mask of the Periacqueductal gray (PAG) from the Brainstem Navigator toolkit [242]. Pearson's correlation coefficient was applied to the parcellated time series to obtain a seed-based correlation vector between PAG and cortical regions. Fisher's z transform was applied to functional connectivity strengths to produce a normal distribution.

A Stenosis Grading Inter-Reader Agreements

Reader 2	Reader 3	BiT CNN Model	Decision Tree Model
0.86	0.80	0.54	0.80

B Dice Scores

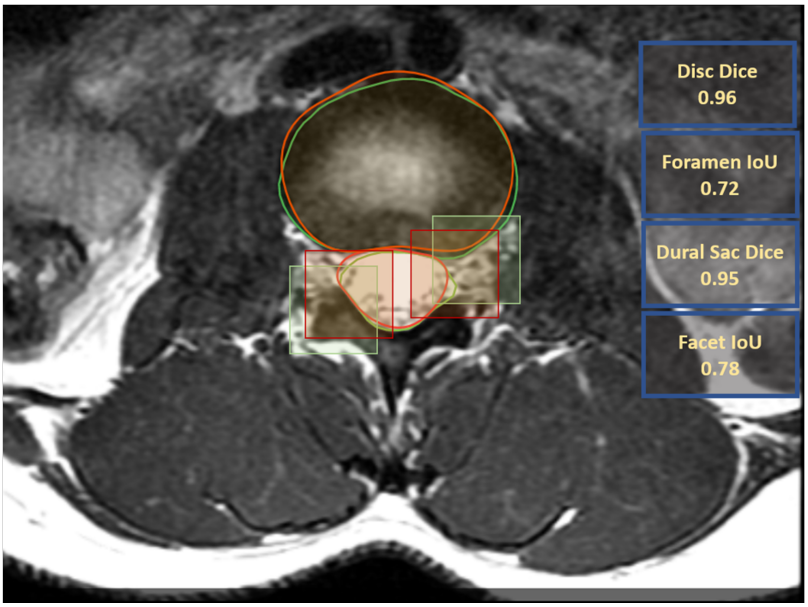

Figure D.1 Central canal stenosis classifier performance. A) Inter-reader agreements between between Reader 1 (neuroradiologist) and Reader 2 (radiology trainee), Reader 3 (musculoskeletal radiologist), big transfer (BiT) convolutional neural network (CNN) model, and decision tree model to classify stenosis. B) Example results of segmentation model, with bounding boxes (red) compared to ground-truth (green) for the right facet and left foramen.

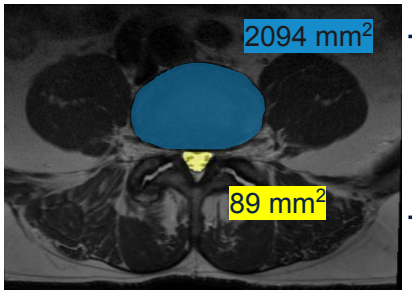

$$DDR = \sqrt{\frac{89}{2094}} = 0.21$$

Grade	Min	Max
Normal	0.33	1
Mild	0.22	0.33
Moderate	0.19	0.22
Severe	0	0.19

Figure D.2 Automatic stenosis grading example. The ratio of the dural sac and disc cross-sectional areas (DDR) is calculated per axial slice. This ratio is used to grade stenosis in each slice using previously validated thresholds.

D.2.4 Statistical Analysis

Linear regression was performed to test for association between central canal stenosis metrics and PEG score, as well as between stenosis metrics and seed-based functional connectivity metrics.

D.3 Results

D.3.1 DDR vs. Pain

The minimum continuous DDR value was obtained for each set of axial slices corresponding to each disc level. We calculated the correlations between this value for each level and subjects' pain measured using the PEG scale, finding that minimum DDR at lower disc levels is negatively correlated with PEG. Additionally, we calculated the extent of stenosis within the spine (i.e. total number of axial slices graded "stenosed"; stenosis grade Mild or above) within the spine and found that a higher number of stenosed levels correlated with higher PEG (Figure D.3).

D.3.2 DDR vs. PAG Functional Connectivity

We evaluated the correlation between extent of stenosis and functional connectivity values between PAG and cortex and found that a larger extent of stenosis is correlated with stronger connectivity between PAG and regions of the parietal and frontal cortices (Figure D.4).

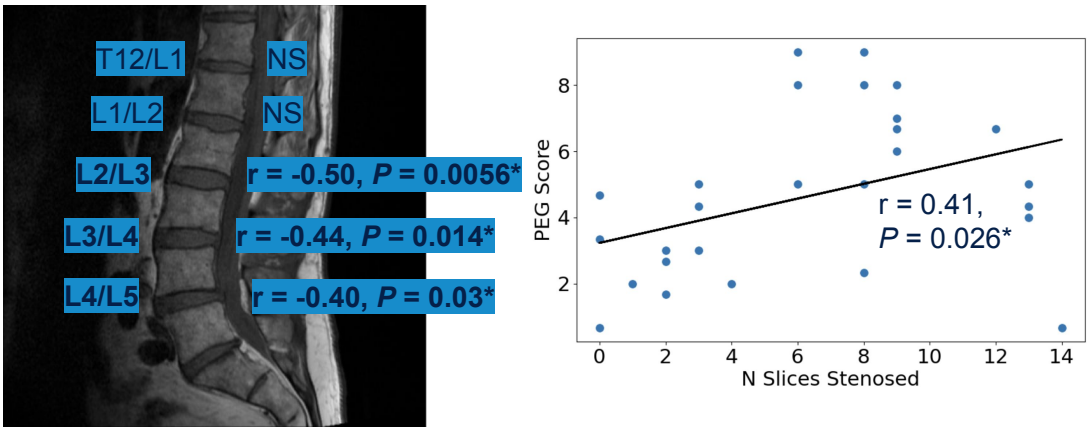

Figure D.3 Central canal stenosis measurements vs. PEG. Example sagittal spine MRI (left) showing group-level correlations between minimum DDR value at individual disc levels and PEG score. NS = Not significant. Scatter plot (right) showing correlation between total number of axial slices graded "stenosed" and PEG score.

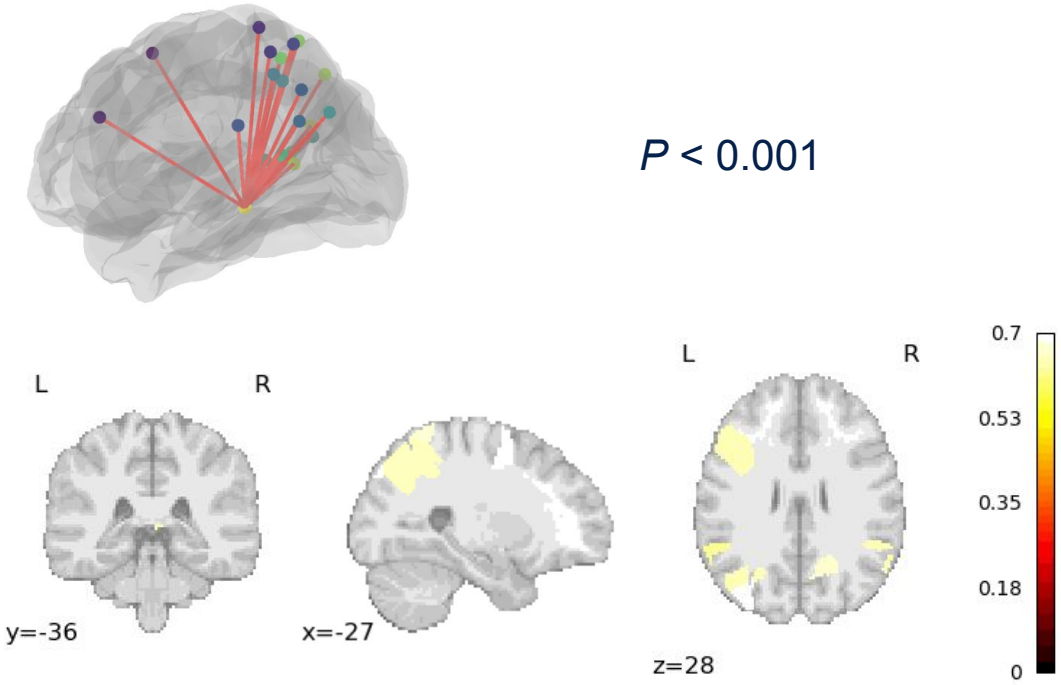

Figure D.4 DDR vs. brain functional connectivity. Figure showing functional connectivity edges correlated ($p < 0.001$) with extent of central canal stenosis. Glass brain (top left) shows each significant edge, while lower row shows the cortical regions associated with each edge, colored by Pearson's R value.

D.4 Conclusions

Our results show that an automatically generated metric of central canal stenosis correlates with reported pain and disability. Additionally, central canal stenosis may be associated with brain functional connectivity changes at rest, specifically with stronger functional connectivity between PAG and regions of the brain associated with sensory processing and higher cognitive functions. Future studies would involve a mediation analysis to investigate whether certain functional connectivity features can predict pain sensation associated with stenosis.

Appendix E

Neural Correlates of Pain Modulation Following Medication Injection

E.1 Introduction

Low back pain (LBP) is one of the leading causes of disability worldwide, yet the underlying neural mechanisms remain incompletely understood. This study investigates the relationship between pain modulation following administration of pain-relieving medication and changes in resting-state functional connectivity in patients with chronic LBP (cLBP). For this preliminary analysis, we investigated the disruption of degree rank order (kD), a unitary measurement of global network reorganization that has been strongly associated with chronic pain. Following Mansour et al., 2016 [73] and others, we hypothesized that a higher level of pain would correlate with more network disruption (a lower kD) and that pain reduction would be associated with network normalization (a kD closer to 0). Additionally, we investigated localized brain network changes pre- and post- treatment.

E.2 Participants

All patients included in this analysis were subjects in a prospective, longitudinal observational study on low back pain, conducted at UCSF as part of the BACPAC initiative [10.1093/pm/pnac202]. Subjects were referred for imaging of the spine as well as fMRI from the UCSF Precision Spine and Peripheral Nerve Center, which provides minimally invasive image-guided injections for patients referred by Orthopedic Surgeons and Neurosurgery with disorders of the spine and peripheral nerves. Referring physicians classified subjects as suffering from predominantly axial (facetogenic) or radicular (neurogenic) LBP, or a combination of both. In this specific analysis, only individuals who received CT-guided pain therapy, indicated and performed by their treating physician, were included. Performed procedures included: facet joint infiltration, nerve root block, combination of nerve root block and facet joint infiltration, sacroiliac joint infiltration, and radiofrequency ablation, and entailed the targeted injection of a corticosteroid (e.g. betamethasone) and local anesthetic (0.75% bupivacaine). During the baseline visit, prior to imaging, demographics (age, sex, body mass index (BMI)) were noted, and all participants completed the Visual Analog Scale (VAS) pain questionnaire. This tool evaluates pain levels on a scale from 0 to 10, where 0 signifies no pain, 5 indicates moderate pain, and 10 represents extreme pain. VAS pain scores were furthermore collected immediately before and after CT-guided therapy. Brain MRI was collected at three time points: baseline, post-injection, and at 12 week follow-up. The study received IRB approval prior to study commencement (IRB 19-29744) and was conducted in full compliance with the principles outlined in the latest version of the Declaration of Helsinki.

Pain trajectories across sessions are shown in Figure E.1 for the full cohort of 41 subjects. For subsequent analyses, we selected those who had quality baseline fMRI data and baseline pain scores available (N = 28, 15 female; age: 63.2 ± 12.8, mean ± SD, age range: 19–86 years old; BMI: 27.8 ± 6.0, BMI range: 20.4-45.8). Additionally, data from three healthy volunteers were used to calculate kD.

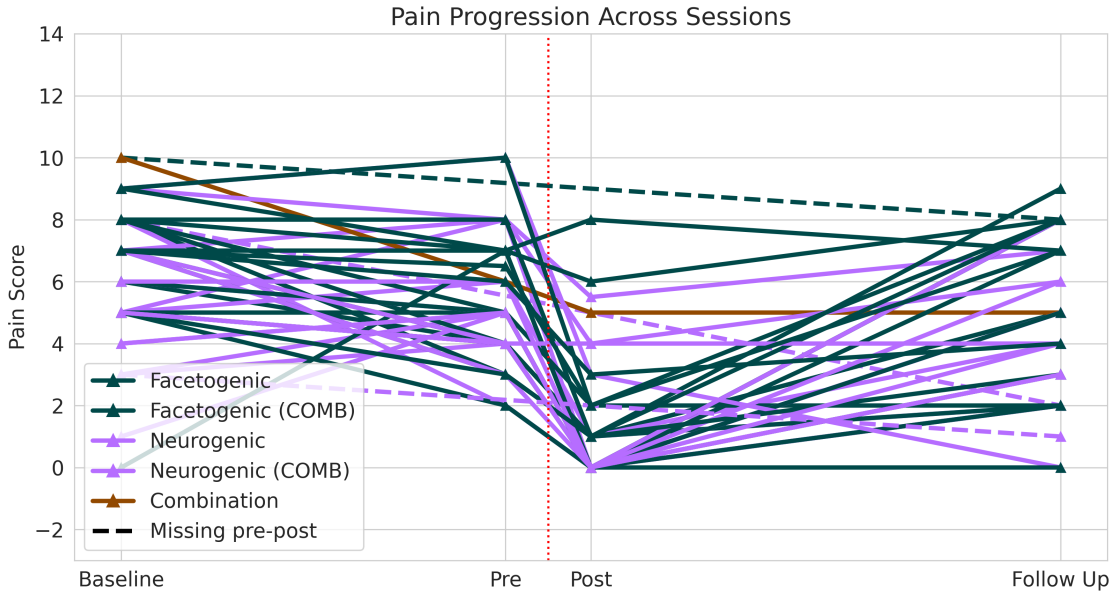

Figure E.1 Pain trajectories pre and post injection.

E.3 Methods

E.3.1 Neuroimaging Processing

Processing was performed using fMRIPrep 20.0.7 [240] and Nilearn [89, 90] following the same protocol described in Chapter 6 (Section 6.2 and Supplementary Materials Appendix B).

E.3.2 Calculation of the degree rank order disruption Index (kD)

kD for each chronic pain patient was estimated following the methods described in [73]. Briefly, each connectome was thresholded at 10% link density, and kD was estimated as the slope of the regression line fitted to the degree difference vector between the subject's connectome and the mean connectome of three healthy controls.

E.3.3 Statistics

Association between kD and pain was tested using Spearman's rank correlation coefficient. Additionally, to identify whether certain brain regions exhibited a large change in node degree pre and post injection, we performed a paired t-test between the degrees of each Brainnetome ROI (246 brain regions) at baseline and immediately following injection for the subset of subjects who had these data available (N=20).

E.4 Results

E.4.1 Association between kD and pain score at baseline

We found no significant correlation between kD and reported pain at baseline, as shown in Figure E.2 (Correlation = -0.11, $p = 0.60$)

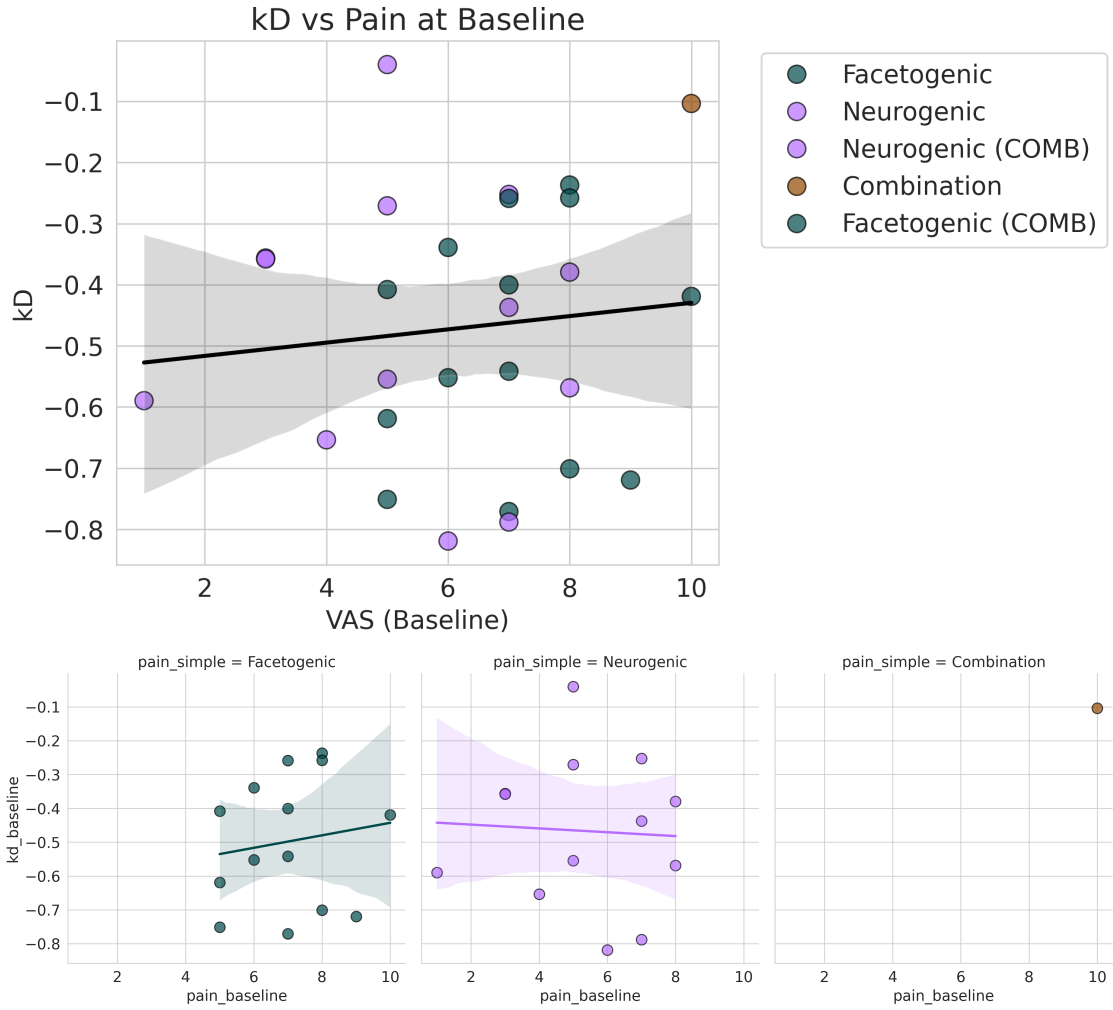

Figure E.2 Association between kD and pain score at baseline.

E.4.2 Association between change in kD and pain reduction following injection

We found no significant correlation between change in kD and change in pain scores from baseline to post-injection, as shown in Figure E.3 (Correlation = -0.17, $p = 0.46$)

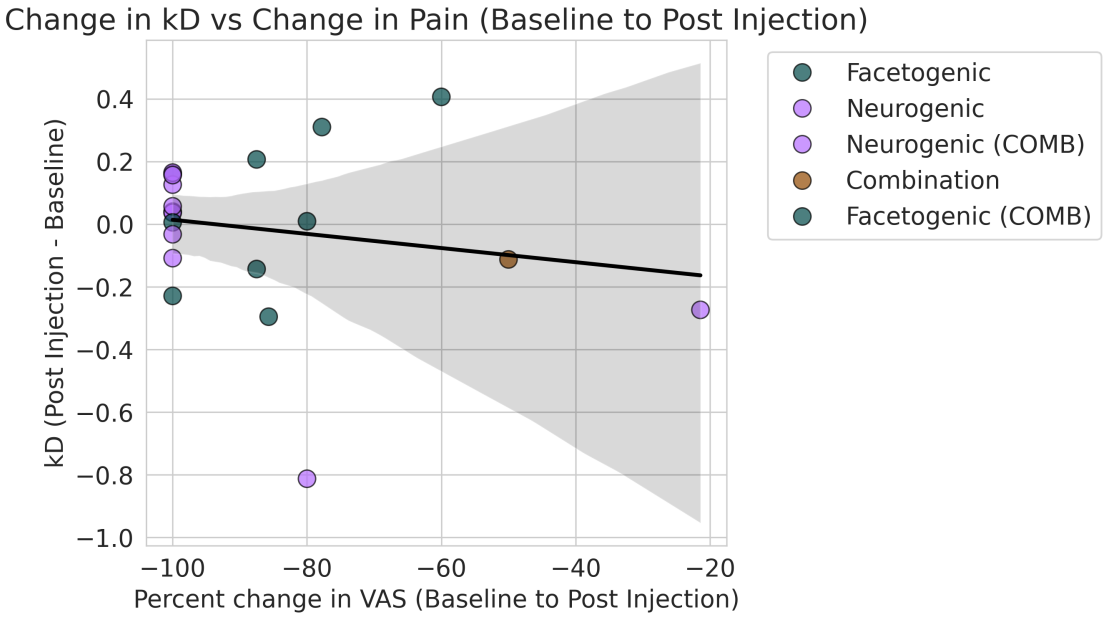

Figure E.3 Association between change in kD and change in pain score from baseline to immediately post-injection.

E.4.3 Association between change in kD and change in pain score at follow-up

We found no significant correlation between change in kD and change in pain scores from baseline to 12 week follow-up, as shown in Figure E.4 (Correlation = 0.27, $p = 0.36$)

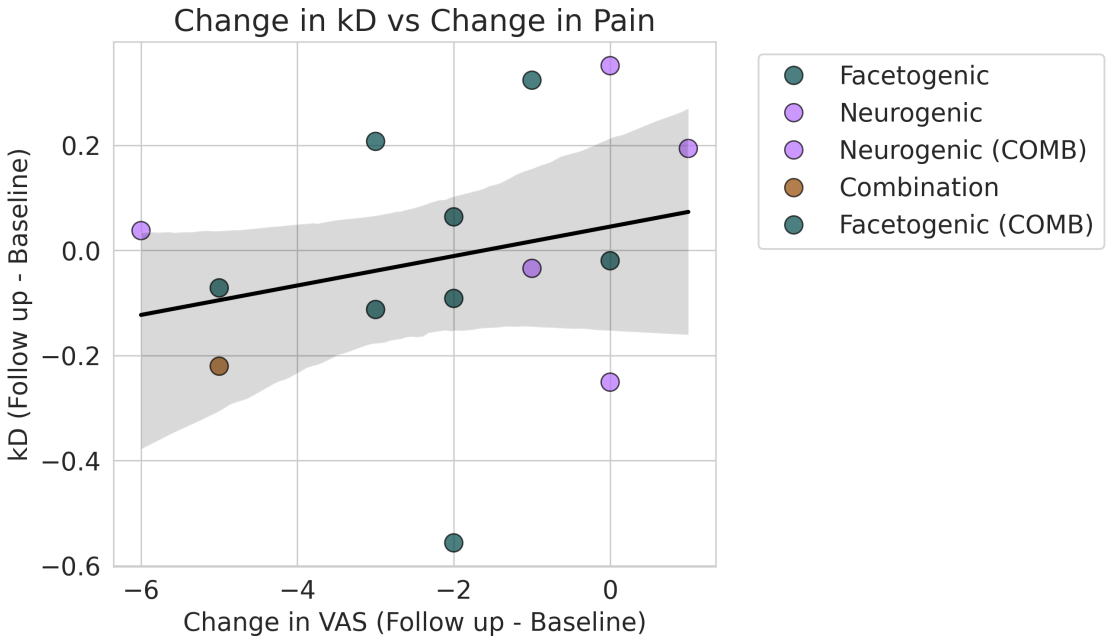

Figure E.4 Association between change in kD and change in pain score from baseline to followup.

E.4.4 Investigation of brain regions associated with pain reduction

We found 10 brain regions that exhibited a significant change in connectivity from baseline to immediately post-injection. Five regions exhibited increased connectivity:

- Left Inferior Parietal Lobule (6_6): T statistic: -3.43, $p = 0.0028$;
- Left Thalamus (8_8): T statistic: -2.26, $p = 0.035$;
- Left Cingulate Gyrus (7_6: T statistic: -2.23, $p = 0.038$;
- Right Superior Frontal Gyrus (7_7): T statistic: -2.15, $p = 0.045$;
- Right Cingulate Gyrus (7_5): T statistic: -2.14, $p = 0.046$)

and five showed decreased connectivity:

- Left Thalamus (8_7): T statistic: 3.33, $p = 0.0035$;
- Right Inferior Parietal Lobule (6_1): T statistic: 2.37, $p = 0.029$;
- Right Inferior Parietal Lobule (6_2): T statistic: 2.35, $p = 0.030$;
- Right Precuneus (4_1): T statistic: 2.33, $p = 0.031$;
- Right Precentral Gyrus (6_2): T statistic: 2.21, $p = 0.040$)

Note: numbers indicate Brainnetome subregion naming convention.

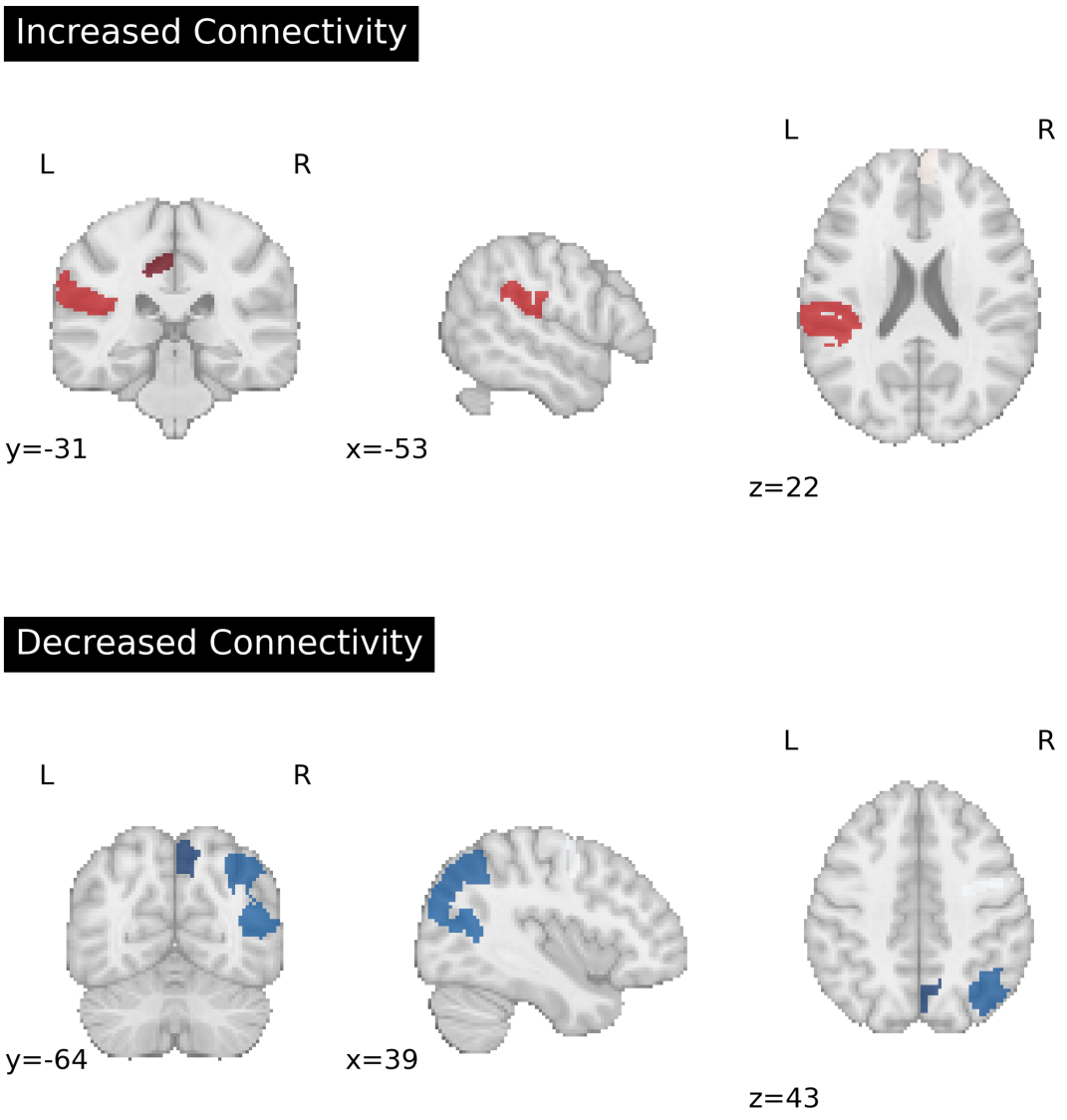

Figure E.5 Regions showing a significant change in degree following injection. Top row shows regions with an increased node degree after injection, while bottom row shows those with decreased degree.

E.5 Discussion

Our results did not support our hypotheses, as we did not show an association between kD and pain measurements. However, this may be due in part to the very low sample size in

this preliminary cohort. A future analysis would involve more subjects and a full age- and sex-matched healthy cohort for kD calculation. We did show changes in connectivity patterns of specific brain regions following injection. These included increased connectivity in the thalamus, cingulate, parietal and frontal lobes, and decreased connectivity in the thalamus, parietal and frontal lobes. We hope to further explore these and other relationships between brain network changes and clinical outcomes in future work.

Appendix F

Code and Data Availability

F.1 Chapter 5

The structural connectivity data analyzed in the main text is openly available from the MGH-USC Human Connectome Project [141] `http://www.humanconnectomeproject.org/`. Structural and functional data analyzed in supplemental figures is available at [225] `https://doi.org/10.5281/zenodo.2872624`. Code is available upon request.

F.2 Chapter 6

The data analyzed in this chapter are currently available on the UCSF rad-cluster, with fMRI data in BIDS format located at `/data/mochila3/ComeBACK/bids` and a table of processed time series located at `/working/mochila2/JC/data/postprocessed/comeback`. These data will be made publicly available on Vivli ahead of final journal publication. The code used in this analysis can be found at `https://git.ucsf.edu/jenncummings/rcca`.

F.3 Chapter 7

The knee connectome generation and analysis code can be found at `/data/VirtualAging/MatalbCode/JC`.

Publishing Agreement

It is the policy of the University to encourage open access and broad distribution of all theses, dissertations, and manuscripts. The Graduate Division will facilitate the distribution of UCSF theses, dissertations, and manuscripts to the UCSF Library for open access and distribution. UCSF will make such theses, dissertations, and manuscripts accessible to the public and will take reasonable steps to preserve these works in perpetuity.

I hereby grant the non-exclusive, perpetual right to The Regents of the University of California to reproduce, publicly display, distribute, preserve, and publish copies of my thesis, dissertation, or manuscript in any form or media, now existing or later derived, including access online for teaching, research, and public service purposes.

DocuSigned by:
Jennifer Cummings
0BB2DF6BB8B1414...
Author Signature

3/21/2025
Date